A Systems Approach to Overcome Tumor-cell Heterogeneity in Drug Response: Metrics and Mechanisms

by

Natacha Comandante-Lou

A dissertation submitted in partial fulfillment
of the requirements for the degree of
Doctor of Philosophy
(Biomedical Engineering)
in the University of Michigan
2022

Doctoral Committee:

Assistant Professor Mohammad Fallahi-Sichani, Chair
Assistant Professor Kelly B. Arnold
Professor Jennifer J. Linderman
Professor Lonnie D. Shea
Associate Professor Greg M. Thurber

Natacha Comandante-Lou

natacom@umich.edu

ORCID iD: 0000-0002-7981-7333

Dedication

To my parents and my brother, who have always supported me and my dreams.

In memory of my aunt, whose battle with cancer inspired me to study this disease.

Acknowledgements

Foremost, I would like to express my deepest gratitude to my advisor, Dr. Mohammad Fallahi-Sichani, for his support, guidance, and inspiration throughout my graduate school journey. Mohammad taught me by example how to become a better scientist, communicator, and mentor. I would like to thank my thesis committee members, Dr. Kelly Arnold, Dr. Jennifer Linderman, Dr. Lonnie Shea, and Dr. Greg Thurber, for their thought-provoking questions and their support through each milestone. I would also like to thank all Fallahi lab members for the inspiring discussions and being unreservedly helpful, especially: Dr. Douglas Baumann and Dr. Mehwish Khaliq, whose experimental expertise and insightful feedback were instrumental to this work; Cara Abecunas, for being there sharing our graduate school life and lab social-chair responsibilities; Dr. Mohan Manikkam, for keeping our lab in order. I acknowledge my funding sources for making this work possible: NIH, Elsa Pardee Foundation and Rackham International Student Fellowship.

I am grateful to Dr. Wendy Thomas for believing in me and her unwavering support as I navigated through this journey. I thank Dr. Gim Toh and Dr. Christine Asidao who were there to listen and support. I thank my friends who keep me sane with board games, distractions, and conversations: from Michigan – Lia Bozarth, Carolina Chung, Sony Choi, Dinank Gupta, Nirmala Maldeniya, Danaja Maldeniya, and Shraddha Surve; from Seattle – Dr. Leonard Wong, Sarah Mac, Tsz Ling Leung, Tin Yan Li, Lael Wentland, Polly Yorioka, and Laura Penner; from Macau – Chris Wong, Lulu Leong, Christy Choi, and Priscila Lau.

I would like to thank my parents Loretta and Patricio, and my brother Marco, for their unconditional love and sacrifices that have brought me to where I am. I would also like to thank Jessi Brown, for keeping me loved and happy through the highs and lows of this process.

Table of Contents

List of Tables

List of Figures

Abstract

Resistance due to tumor cell heterogeneity poses a major challenge to the use of targeted therapies for cancer treatment. Targeted therapies that are designed to block oncogenic signaling in tumor cells often yield substantial short-term responses but fail to fully eradicate tumors. Among the major barriers to full cures is the cell-to-cell heterogeneity in drug response that arises even among genetically identical cells. Recent single-cell studies have revealed that such non-genetic heterogeneity can prime a rare, transient subpopulation of tumor cells to be intrinsically drug-tolerant or render them cellular plasticity to adapt to drug-induced stress dynamically. These therapy escapees constitute a reservoir of reversibly drug-tolerant cells, which can then acquire more stably resistant phenotypes with continuous drug exposure, ultimately driving tumor relapse. Although the emergence and consequences of such intrinsic and adaptive heterogeneities are widely recognized, their molecular basis and their connection to variable states of drug sensitivity remain elusive. Furthermore, the dynamic responses of residual subpopulations of drug-tolerant cells are often obscured by fixed-time population-based measurements in most pre-clinical drug-response assays, posing another challenge to the design of effective therapeutic strategies to overcome drug resistance.

The focus of this dissertation is to address these gaps in our knowledge by quantifying and dissecting the origins of cell-to-cell heterogeneity in cancer drug response using systems biology approaches. First, I developed new experimental and mathematical frameworks to evaluate time-dependent drug responses using probabilistic metrics that quantify drug-induced phenotypic events (i.e., cell death and division) at the single-cell level. By quantifying single-cell phenotypic events over time, these metrics provide a more accurate description of drug response for heterogeneous cell populations. Furthermore, these metrics can reveal which drugs or drug combinations have the ability to block rare subpopulations of drug-tolerant cells. Thus, they have important implications for designing efficacious treatments to avoid therapeutic escape.

Second, this thesis investigates the molecular basis of cellular plasticity and non-genetic heterogeneity in drug response, focusing on the activator protein 1 (AP-1) transcription factor family, for their roles as key effectors of the mitogen-activated protein kinase (MAPK) pathway in BRAF-mutant cancers. Using BRAF-mutant melanoma as a model system with dysregulated MAPK signaling, I employed systems biology approaches that integrated data-driven modeling with multiplexed measurements to capture single-cell heterogeneity before and after MAPK inhibitor treatments in BRAF-mutated melanoma cells. I showed that the state of the AP-1 network plays a unifying role in explaining the intrinsic diversity of phenotypic states and adaptive responses to MAPK inhibitors. Perturbing the state of the AP-1 network through genetic depletion of specific AP-1 proteins, or by MAPK inhibitors, shifts cellular heterogeneity in a predictable fashion. Thus, AP-1 may serve as a critical node for manipulating cellular plasticity with potential therapeutic implications. Together, this thesis may facilitate future efforts for the rational design of therapeutic strategies that aim at overcoming the challenge of drug resistance arising due to tumor cell heterogeneity and plasticity.

Chapter 1 Introduction

The Human Genome Project has opened up the possibility of understanding the genetic basis of human diseases [1]. This new understanding fuels the movement towards precision medicine [2], which together with the rapid pace of drug development, has provided new treatment options for many cancers through molecularly targeted therapies. Targeted therapies are designed to selectively inhibit oncoproteins or components of their effector signaling cascades that drive tumor growth. They block tumor cells by exploiting their elevated dependency on the hyperactivated oncogenic pathways for survival and cell growth, a phenomenon also known as *oncogene addiction* [3,4]. As a result, targeted therapies have drastically improved the safety and efficacies of cancer therapies over conventional cytotoxic agents that block the general cell proliferative processes [5]. Prominent examples of targeted therapies include the use of imatinib to inhibit the deregulated fusion protein BCR-ABL that drives chronic myeloid leukemia [6], the epidermal growth factor receptor (EGFR) inhibitor gefitinib for EGFR-mutated non-small-cell lung cancer [7], and serine-threonine protein kinase B-RAF (BRAF) inhibitor vemurafenib for BRAF-mutant melanoma, the deadliest form of skin cancer [8]. These pioneering examples mark a paradigm shift in anticancer drug development from the broad, fortuitous search for exceptional responders within patient populations, to the focused investigation of new mutation-tailored therapeutics in a subset of patients with defined genomic signatures [9].

Therapeutic resistance due to tumor heterogeneity, however, still represents a major hurdle for achieving full cure with targeted therapies. Even in patients who have substantial initial responses, treatments eventually fail to fully eradicate tumors, and subsequently lead to progression of drug-resistant disease. A paradigmatic example of therapy resistance is observed in response to BRAF/MEK-targeted therapies in melanoma. Small-molecule BRAF inhibitors and their combinations with MEK kinase inhibitors have greatly improved the prognosis in BRAF-mutant melanoma patients [8,10]. Nevertheless, they are commonly not curative for most patients. Many patients experience tumor relapse due to acquired resistance, which evidently arises from the regrowth of a small fraction of residual cells that escape the initial phase of treatment [11,12]. The challenge of incomplete response to targeted therapies is prevalent across different cancers, shedding light on a common phenomenon in cancer biology [5]; yet the root mechanisms of resistance remain elusive.

Mounting evidence has revealed a wide spectrum of phenotypic outcomes among and within tumors upon inhibition of the mutated oncogenic pathways. Across tumors, responses to targeted therapies varies vastly in the extent and in the duration of response [8,12] (Figure 1.1). Within the same tumor population, the suppression of oncogenic signaling leads to considerable variability in cell fates and cell states, including apoptosis, proliferative arrest, or changes in differentiation state and metabolic state [13–18]. The variety of phenotypic responses to targeted therapies demonstrates the remarkable diversity across tumor cells in their state of oncogenic pathway dependency that cannot be fully explained by their genetic background alone. Understanding the molecular origins of such heterogeneity and precisely how drug-resistant tumor cells arise from seemingly homogeneous populations of cells are essential for improving the outcome of targeted therapies in patients.

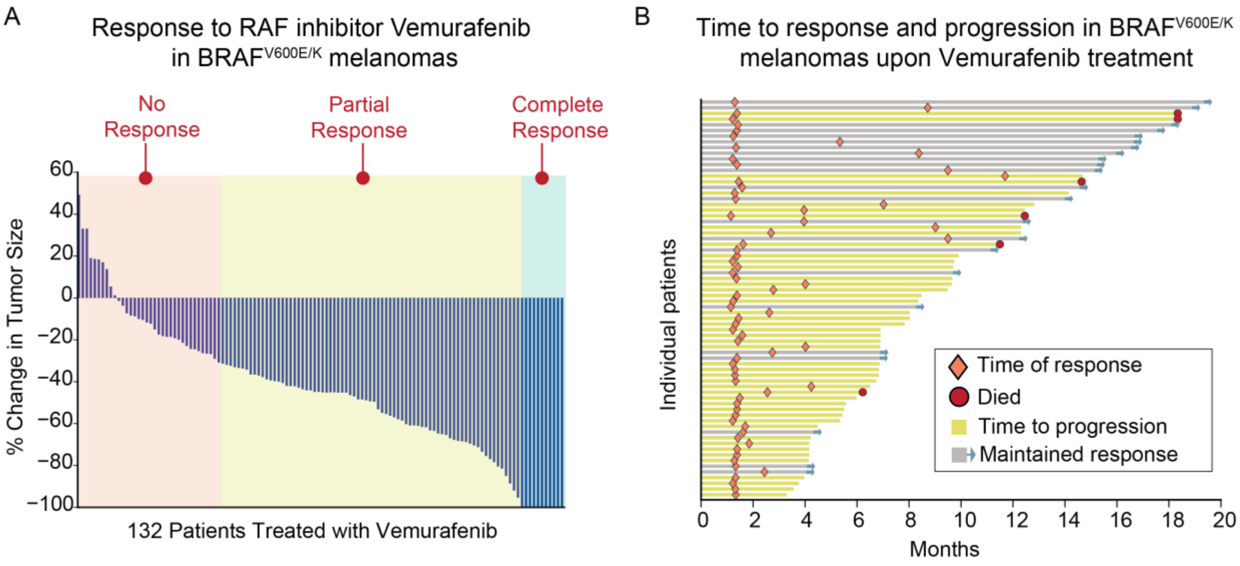

Figure 1.1 Variability in response to RAF inhibitor in BRAF-mutant melanoma patients.

(A) Objective response across 132 BRAF-mutant melanoma patients treated with BRAF inhibitor Vemurafenib. **(B)** Time to response and response duration among 69 patients who had a response. (Adapted from Sosman *et al* [8])

1.1 Heterogeneity in the state of pathway dependency

Cell-to-cell variability in drug response can arise from heterogeneity in the extracellular environment, such as variability in the spatial distribution of drug or paracrine signaling from the microenvironment [19–21]. Cell-autonomous heterogeneity, however, is also a major driver of therapeutic resistance. Heterogeneity can arise because of genetic variability among tumor cells. For example, mutations in the gatekeeper residue of the targeted molecules may enable some tumor cells to escape the effect of therapy by sterically impairing the binding of the drug [22,23]. Alternatively, genetic alterations can alleviate the dependency of tumor cells on a single oncoprotein by activating upstream or downstream effectors of the targeted pathway, or by engaging parallel pro-growth pathways [24–27] (Figure 1.2).

Cell-to-cell variability in drug response may have non-genetic origins, as seen among genetically identical cells that are exposed to uniform concentrations of drugs [28–30]. Such phenotypic diversity in the absence of genetic variation has been the topic of extensive research in the past decade, and may be attributed to a combination of factors that influence the state of oncogenic pathway dependency across individual cells (Figure 1.2), including:

I) the epigenetic regulation of transcriptional states (e.g. differentiation states) [11,13–16,28,31,32];

II) stochastic fluctuations in the abundance, localization and activity of key molecules (e.g. mRNA or protein of an effector gene that bypasses the targeted oncogene) [29,33–36];

III) multi-stability and oscillation generated by certain biological circuit topologies (e.g. a bistable switch formed by feedback motifs) [37–40].

Altogether, the non-genetic sources of cell-to-cell variability diversify the phenotypic responses of tumor cells to cancer drugs. Such deviation from the simple one-to-one genotype-phenotype mapping poses a significant challenge to the use of targeted therapies for cancer treatment [41].

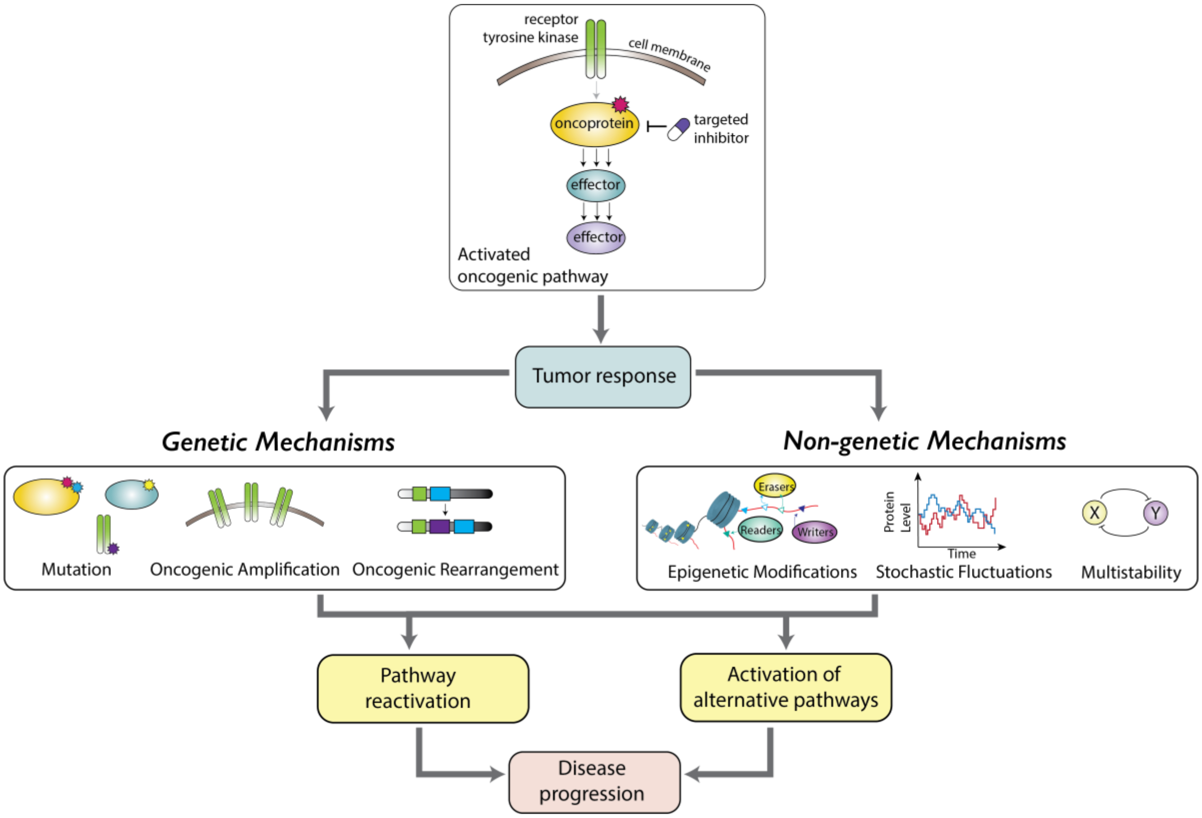

Figure 1.2 Different sources of heterogeneity give rise to resistance to targeted therapies.

Resistance is conferred by genetic and non-genetic sources of heterogeneity, which changes the state of oncogenic pathway dependency of tumor cells.

1.2 Survival of the outliers: selection and adaptation

One possible way for the emergence of drug resistance is through Darwinian selection against intrinsic heterogeneity that exists within the cell population independent of drug treatment. As demonstrated by Luria and Delbrück in an elegantly simple experiment in 1943 [42], molecular variations among cells, which exist prior to drug treatment, may provide small subpopulations of cells with survival advantage when they are exposed to cytotoxic drugs [43–46] (Figure 1.3). Such intrinsic cell-to-cell variability that renders drug resistance has been conventionally attributed to genetic heterogeneity among cells [12,42,45–48]. However, recent studies have revealed that such heterogeneity may also exist among genetically homogeneous populations of cells, leading to fractional killing of tumor cells and the enrichment of drug-tolerant persister cells following drug treatment [14,28,30,43,44,49]. These persister cells may constitute subpopulations with a size as small as < 1% of the total cancer cell population, and may dynamically fluctuate between drug-sensitive and slow-growing drug-tolerant states in the absence of drug [14,28]. Upon selection and growth following drug treatment, they undergo further changes and ultimately evolve toward acquired genetic resistance in response to a continuous drug-induced selective pressure [43,44].

In addition to the pre-existing intrinsic heterogeneity that facilitates the Darwinian selection of drug-tolerant cells, drug-induced adaptive changes in cells may lead to drug resistance. The emergence of such reversibly drug-adapted phenotypes has been described using a Lamarckian induction framework, in which tumor cells respond to drug treatment by activating a variety of homeostatic adaptive mechanisms that allow them to escape the cytotoxic effects of therapy [50,51] (Figure 1.3). Such adaptive responses have been shown to be remarkably diverse both across genetically distinct tumors and among genetically identical cells. The most commonly reported adaptive responses to targeted therapies are those that involve either reactivation of the targeted pathway [52] or up-regulation of an alternative pro-growth pathway or stress/cytokine response [53–60], reflecting the feedback regulation in cell signaling homeostasis. The diversity and complexity of these adaptive cascades, however, suggests the possibility of a more global epigenetic reprogramming of phenotypic states that enable tumor cells to adapt to environmental stress. In the case of BRAF-mutant melanomas, time-lapse live-cell experiments followed by single-cell analysis have revealed the emergence of slow-cycling, drug-tolerant cells that exhibit a de-differentiated phenotype within 1 to 2 days of BRAF/MEK inhibitor treatment [15,61]. Upon growing in the absence of drugs, or with the inhibition of appropriate epigenetic modifiers, these drug-tolerant cells can be reverted to a differentiated, drug-sensitive state [15]. Such developmental plasticity associated with drug resistance has recently been observed in numerous studies for various cancers in cell cultures [15,60,62,63], mouse models [11,63,64] and patients [17], suggesting that lineage switching could be a universal mechanism for adaptive resistance. Notably, across different cancers, these drug-adaptive phenotypes commonly maintain effective pathway suppression in the presence of drug. This suggests that lineage switching is often accompanied with a transient transformation into a less oncogene-dependent state. [15,50,63–65].

Cellular mechanisms that lead to drug resistance through selection or adaptation are not mutually exclusive. For example, drug-tolerant persister cells transiently primed via natural fluctuations in the expression of drug resistance genes can be selected by drug treatment. The continuous presence of the drug can further push these surviving outliers into a more stable or irreversible oncogene-independent state through dynamic, stepwise epigenetic reprogramming [28,31]. Collectively, these various mechanisms of drug resistance demonstrate a rich intraclonal dynamics of tumor cell heterogeneity that necessitates novel therapeutic approaches. While often the acquired genetic mutations conferring resistance seem to be a moving target that escape constant development of newer generations of targeted inhibitors, the transient maintenance of slow-cycling, drug-tolerant states appears to be a common phenomenon across different cancer types and drug-treatments. Furthermore, these drug-tolerant states are typically observed much earlier (in hours or days) than the emergence of genetic resistance (in months or years). Thus, these transient drug-tolerant states could provide new therapeutic targets and an opportunity of early intervention.

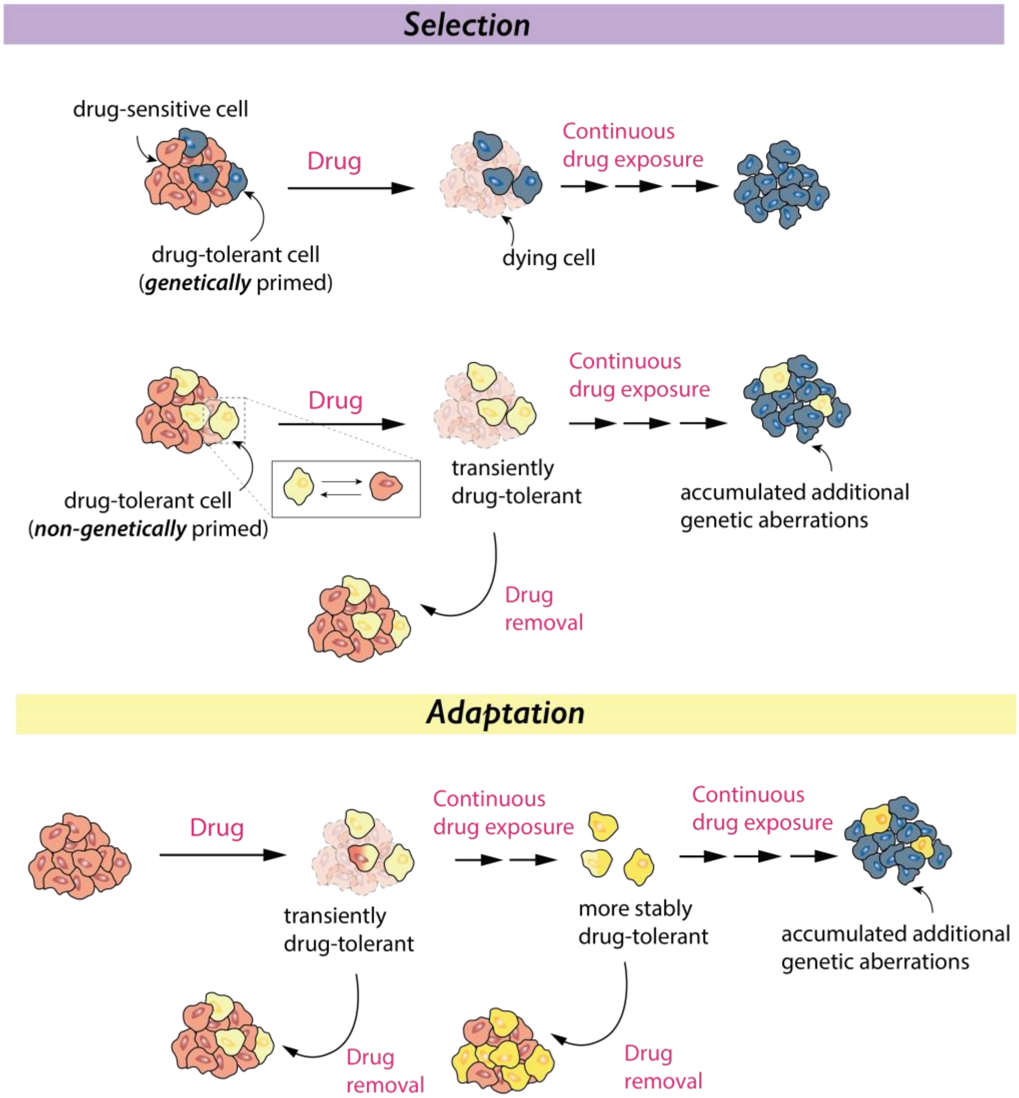

Figure 1.3 Fractional tumor-cell killing can arise from selection of intrinsic heterogeneity or drug-induced adaptation.

Resistance to targeted therapy emerges from a small fraction of drug-tolerant cells, which can be selected by therapeutic pressure, or generated by drug-induced adaptive mechanisms. These residual drug-tolerant cells constitute a reservoir for establishing more stable resistant phenotypes through acquiring additional genetic alterations or epigenetic reprogramming.

1.3 Overcoming drug resistance and cellular plasticity

Leveraging our new understanding of tumor cell heterogeneity and plasticity, the following two main categories of strategies that focus on minimizing these slow-cycling, drug-tolerant cells could be envisaged to overcome the challenge of fractional tumor cell killing. The first approach is to selectively target the drug-tolerant states, including those that pre-exist as persister cells or those that emerge though phenotype switching. Such an approach leverages a concept parallel to synthetic lethality, where a tumor-specific alteration in one gene may increase the essentiality of another, creating a new vulnerability to be exploited therapeutically [66,67]. Often, the shift in the dependence of these drug-tolerant states on the targeted pathway is also accompanied with increased dependence on alternative transcriptional or metabolic activities [14,18,68], thus exposing drug-tolerant cells to new vulnerabilities that are specific to them. For example, loss of differentiation in melanoma cells that are tolerant to BRAF inhibitors renders them more vulnerable to ferroptosis-inducing drugs due to their increased susceptibility to oxidative stress [13].

An alternative class of strategies to maximize tumor cell killing is to modulate the variability of a tumor cell population by targeting the regulators of such variability. For pre-existing heterogeneity, targeting the regulatory pathways that drive the primed drug-tolerant persister states could minimize the frequency of their existence in the first place [31]. For the heterogeneity that emerges dynamically from adaptive responses, targeting key phenotype-switching regulators to either block or revert such transition [11,69–72], could overcome the challenge of cellular plasticity. The establishment of new transient drug-adaptive phenotypes predominantly requires global remodeling and licensing of the epigenetic landscape. Such epigenetic landscape then permits execution of various transcriptional programs for drug-adaptation or lineage conversion. Focusing on the epigenetic process of phenotype switching, several levels of molecular mechanisms could be potential targets: I) epigenetic regulators that modulate chromatin accessibility [15,16,73,74], II) pioneer factors that select enhancer landscapes and recruit additional transcription factors for lineage-specific programs [75,76], III) lineage-specific transcription factors that directly control cellular reprogramming [72,77,78], and IV) signaling pathways that are crucial to the establishment of drug-tolerant phenotypes [52,54].

The heterogeneous and dynamic nature of tumor cell phenotypic responses to anticancer drugs suggests that full eradication of tumor cells would most likely require a combination of targeted therapies. Indeed, co-targeting oncogenic dependency and cellular plasticity of a tumor population has yielded the most substantial response compared to either approach alone in certain cancers [15,72,79]. Therefore, identifying the optimal combinatorial therapy approaches will be key to achieving full cure.

1.4 Quantification of drug response and drug combination interactions for heterogeneous populations of tumor cells

Quantification of drug response is essential for the discovery of novel cancer drugs, the prioritization of promising compounds for clinical investigations, and the elucidation of their mechanisms of action [80–83]. The current standard to quantify anticancer drug response is based on dose-response curves, which are generated by measuring cell count at a fixed time-point (typically 72 h or 96 h) following the exposure of cells to varying concentrations of a drug. A dose-response curve captures at least two distinct pharmacological properties of a drug: potency and efficacy (Figure 1.4 A). Potency is the drug concentration required to achieve a given level of drug response (e.g., 50% inhibition in growth rate). Efficacy, in contrast, is the maximum response attainable by a drug at its highest tolerated dose. Conventionally, relative viability (number of cells in the drug-treated culture relative to the untreated control) across dose is fitted to a sigmodal function given by the Hill Equation [84], from which quantitative metrics such as half-maximum inhibitory concentration (IC_{50}), drug maximal effect (E_{max}), area under the dose-response curve (AUC) and hill slope (HS) are extracted (Figure 1.4 B). These dose-response curve metrics are routinely used to compare various aspects of drug sensitivity across cell lines and drug types. These dose-response metrics have also been used in large-scale pharmacogenomic studies to systematically identify genomic predictors of drug sensitivity and resistance in tumor cells through statistical analysis [80–82]. Despite their wide-spread usage, these conventional dose-response metrics fall short in capturing the following two emerging areas of cancer pharmacology: variability and dynamics. Addressing these challenges are critical for the discovery of effective therapies to overcome cell-to-cell heterogeneity in drug response and ultimately drug resistance.

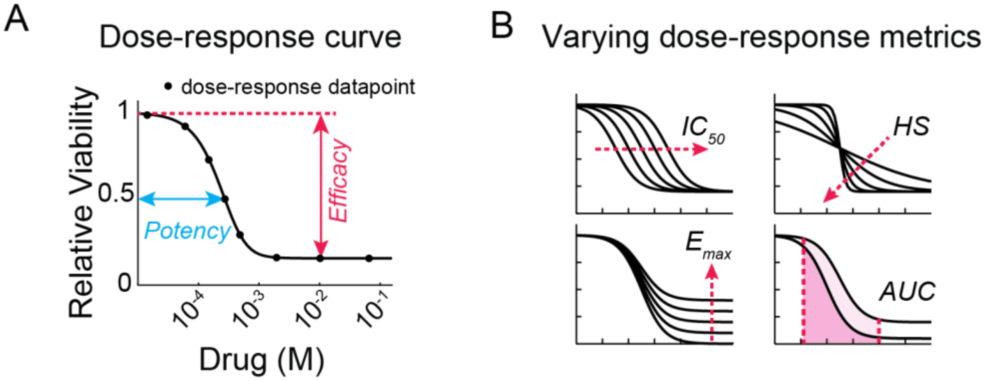

Figure 1.4 Conventional dose-response curve and metrics.

(A) Conventional dose-response curve. Potency is the dose required to achieve a given level of response. Efficacy is the response attainable at the maximum tolerated dose. **(B)** Dose-response metrics vary with the shape of the dose-response curves (adapted from Fallahi-Sichani *et al* [85])

1.4.1 Variability in drug sensitivity

Conventional dose-response curves use cell population survival as the main readout for drug response. Such population-level measurements are the result of a sequence of events that in combination determine the drug effect, including drug uptake, target engagement, alteration of downstream pathways, and the resulting phenotypes [86]. Variations in each of these events and pathways may contribute to variations in the overall shape of the dose-response curve. When comparing dose-response curves across cell populations, one may ask which aspects of dose-response most represent drug sensitivity. Without delineating the origins of variations in dose-response parameters, the answer to this question may not be obvious. In fact, multiparametric studies have demonstrated that different dose-response metrics encode complementary yet distinct information about how populations of cells respond to a drug [85,87].

Conventionally, comparative analyses of anticancer drug responses have mainly focused on variations in drug potency (e.g., IC_{50}), assuming that it most importantly represents drug sensitivity. Variations in potency can be explained by differences in drug-target interactions (e.g., binding affinities), drug and target concentrations, (e.g., drug influx/efflux, number of target receptors), polypharmacology (e.g., secondary targets) and existence of pathway redundancy (e.g., presence of a secondary oncogenic driver), among others [86]. More potent drugs engage more targets more effectively, therefore, require a lower drug concentration to achieve the same amount of response.

On the other hand, variations in metrics other than potency (e.g., E_{max} and HS) are rarely examined in traditional pharmacology. Variations in efficacy, for example, arise from differences in the amount of heterogeneity in drug response within the cell population. Such cell-to-cell variability is less commonly considered in classical pharmacology because measurements are typically made on bulk populations of cells. However, recent single-cell studies have revealed a remarkable level of cell-to-cell variability even within genetically-homogeneous populations of tumor cells [15,28–30]. Cell-to-cell fluctuations in protein abundance or activity involving the drug-response pathway may cause the dose-response relationship to vary from one cell to the next. At the population level, averaging these varying dose-response relationships across cells can give rise to dose-response curves that vary in metrics other than potency. In fact, shallow dose response curves (i.e. low efficacies) often correlate with the emergence of drug-tolerant or drug-adapted subpopulations [85], which have important implications in driving therapy resistance. Overcoming such cell-to-cell variability motivates efforts towards identifying efficacious combination therapies that minimize cross-resistance by blocking subpopulations of drug-tolerant cells. However, the reliance on population-averaged measurements in conventional dose-response analyses limits our ability to delineate how heterogeneity is influenced by combined drug interactions. Quantifying such heterogeneity within a population, therefore, requires single-cell measurements and metrics that consider the probabilistic nature of drug response and its variation from one cell to another.

1.4.2 Dynamics of drug response

The relative-viability approach in assessing drug response suffers from a fundamental flaw, which is being confounded by variations in cell proliferation rate and assay duration. The reason is that cell count, which is used as a normalization factor in the calculation of relative viability, is nonlinearly time-dependent. Consequently, the use of relative viability in pharmacogenomic studies may lead to false-positive and false-negative associations between genomic variables and drug sensitivity [87]. To correct for such bias, new generation of drug response metrics, such as drug-induced proliferation (DIP) rate [88] and growth rate (GR) inhibition [89], have recently been proposed and applied [16]. These metrics measure drug-induced changes as a function of drug dose in terms of the net growth rate of the tumor cell population instead of their relative viability. By normalizing the net growth rate in drug-treated cell population to the untreated control, these metrics correct for the variability in growth rate that is irrelevant to drug treatment, such as basal variability in proliferation rate across tumor populations and arbitrary differences in experiment conditions and durations.

While these new generation metrics correct for an important bias in the conventional dose-response metrics, their assumption of time-invariant growth rate is not always valid. Moreover, their reliance on fixed-time measurements does not sufficiently capture the complexity and heterogeneity of drug response among individual cancer cells that may adapt to treatment or become selected because of varied levels of intrinsic sensitivity to drug. For instance, the emergence of a drug-adaptive state due to phenotype-switching may occur 48 hour after MAPK inhibitor treatment in one BRAF-mutated melanoma cell line, while in a different cell line, such adaptive state may not be observed even after 96 h [15]. Furthermore, residual drug-tolerant cells are likely undetectable at early timepoints with population measurements, but with time, drug-sensitivity of the population decreases as the drug-tolerant subpopulation is enriched. Measurements of drug response at arbitrarily fixed time-points, therefore, will likely miss important information of the population response in the long-term.

1.5 Structure of thesis

As described above, resistance to therapy due to tumor cell heterogeneity remains to be a major challenge in the use of targeted therapies. Molecular differences generate cell-to-cell variability in phenotypes that profoundly impact the efficacy and duration of response to targeted therapies. Recent system-wide single-cell studies have revealed that resistance is driven by rare subpopulations of drug-tolerant tumor cells that transiently escape the early phase of treatment and regrow with prolonged drug-exposure. These rare subpopulations can arise from the intrinsic heterogeneity within a tumor population prior to treatment or emerge from adaptive phenotypic switching. Despite our increasing knowledge of phenotypic diversity in tumor cell drug response, the molecular basis of such cellular plasticity and its connection to the diverse state of oncogene dependency remains poorly understood. Furthermore, responses from these residual rare subpopulations are not captured in most pre-clinical drug response assays, posing another challenge to discover therapy agents that block such heterogeneity. Here, I present a dissertation that applies systems pharmacology and single-cell biology approaches to address these challenges from two angles:

I) developing new drug-response metrics to score such rare-cell variability**;**

II) elucidating the mechanisms underlying cellular plasticity, using BRAF-mutated melanoma as a model system.

The approaches to these goals can be organized into the following two aims:

Aim 1: Developing new mathematical and experimental frameworks to model cell-to-cell variability in drug response and combination efficacy (Chapter 2)

Cell-to-cell variability generates subpopulations of drug-tolerant cells that diminish therapeutic efficacy, even in populations of cells that are scored as highly sensitive based on drug potency. Overcoming such heterogeneity and blocking subpopulations of drug-tolerant cells motivate efforts toward identifying efficacious combination therapies. The success of these efforts depends on our ability to distinguish how heterogeneous populations of cells respond to individual drugs, and how these responses are influenced by combined drug interactions. In this aim, I propose mathematical and experimental frameworks to evaluate time-dependent drug interactions based on probabilistic metrics that quantify drug-induced tumor cell killing or inhibition of division at a single-cell level. These metrics can reveal heterogeneous drug responses and their changes with time and drug combinations. Thus, they have important implications for designing efficacious combination therapies, especially those designed to block or overcome drug-tolerant subpopulations of cancer cells.

Aim 2: Elucidating the role of AP-1 transcription factor family in melanoma differentiation state heterogeneity and plasticity underlying MAPK inhibitor response (Chapter 3)

Cellular plasticity underlies the observed cell-to-cell variability in MAPK inhibitor response in melanomas. Understanding the molecular basis for cellular plasticity is therefore key to overcome fractional tumor-cell killing. Such plasticity has been associated with fluctuations in transcriptional programs that are linked to melanoma differentiation state heterogeneity, or with diverse adaptive responses that reflect signaling homeostasis upon inhibition of MAPK signaling. It remains unclear whether these seemingly distinct forms of heterogeneity are driven by independent mechanisms, or by an overarching process governed by a common set of molecular players. In this aim, I test the hypothesis that the Activator Protein 1 (AP-1) transcription factor network serves as a critical node that unifies diverse patterns of cellular plasticity in melanoma cells. Using systems approaches and single-cell analyses, I show that the state of the AP-1 network explains both the intrinsic heterogeneity of differentiation states and adaptive responses to MAPK inhibition in individual melanoma cells. Perturbing the AP-1 state can shift such cellular heterogeneity in a predictable fashion. Therefore, AP-1 may be leveraged therapeutically for manipulating cellular plasticity in melanoma to minimize therapy escape.

References

1. Collins FS, Patrinos A, Jordan E, Chakravarti A, Gesteland R, Walters L. New goals for the U.S. Human Genome Project: 1998-2003. Science. 1998;282: 682–689. doi:10.1126/science.282.5389.682

2. Collins FS, Varmus H. A New Initiative on Precision Medicine. New England Journal of Medicine. 2015;372: 793–795. doi:10.1056/NEJMp1500523

3. Weinstein IB, Joe A. Oncogene Addiction. Cancer Res. 2008;68: 3077–3080. doi:10.1158/0008-5472.CAN-07-3293

4. Garraway LA, Jänne PA. Circumventing Cancer Drug Resistance in the Era of Personalized Medicine. Cancer Discov. 2012;2: 214–226. doi:10.1158/2159-8290.CD-12-0012

5. Bivona TG, Doebele RC. A framework for understanding and targeting residual disease in oncogene-driven solid cancers. Nature Medicine. 2016;22: 472–478. doi:10.1038/nm.4091

6. Druker BJ, Tamura S, Buchdunger E, Ohno S, Segal GM, Fanning S, et al. Effects of a selective inhibitor of the Abl tyrosine kinase on the growth of Bcr–Abl positive cells. Nature Medicine. 1996;2: 561–566. doi:10.1038/nm0596-561

7. Lynch TJ, Bell DW, Sordella R, Gurubhagavatula S, Okimoto RA, Brannigan BW, et al. Activating mutations in the epidermal growth factor receptor underlying responsiveness of non-small-cell lung cancer to gefitinib. N Engl J Med. 2004;350: 2129–2139. doi:10.1056/NEJMoa040938

8. Sosman JA, Kim KB, Schuchter L, Gonzalez R, Pavlick AC, Weber JS, et al. Survival in BRAF V600–Mutant Advanced Melanoma Treated with Vemurafenib. New England Journal of Medicine. 2012;366: 707–714. doi:10.1056/NEJMoa1112302

9. Cohen P, Cross D, Jänne PA. Kinase drug discovery 20 years after imatinib: progress and future directions. Nat Rev Drug Discov. 2021;20: 551–569. doi:10.1038/s41573-021-00195-4

10. Long GV, Stroyakovskiy D, Gogas H, Levchenko E, de Braud F, Larkin J, et al. Combined BRAF and MEK Inhibition versus BRAF Inhibition Alone in Melanoma. New England Journal of Medicine. 2014;371: 1877–1888. doi:10.1056/NEJMoa1406037

11. Rambow F, Rogiers A, Marin-Bejar O, Aibar S, Femel J, Dewaele M, et al. Toward Minimal Residual Disease-Directed Therapy in Melanoma. Cell. 2018;174: 843-855.e19. doi:10.1016/j.cell.2018.06.025

12. Wagle N, Emery C, Berger MF, Davis MJ, Sawyer A, Pochanard P, et al. Dissecting Therapeutic Resistance to RAF Inhibition in Melanoma by Tumor Genomic Profiling. J Clin Oncol. 2011;29: 3085–3096. doi:10.1200/JCO.2010.33.2312

13. Tsoi J, Robert L, Paraiso K, Galvan C, Sheu KM, Lay J, et al. Multi-stage Differentiation Defines Melanoma Subtypes with Differential Vulnerability to Drug-Induced Iron-Dependent Oxidative Stress. Cancer Cell. 2018;33: 890-904.e5. doi:10.1016/j.ccell.2018.03.017

14. Sharma SV, Lee DY, Li B, Quinlan MP, Takahashi F, Maheswaran S, et al. A Chromatin-Mediated Reversible Drug-Tolerant State in Cancer Cell Subpopulations. Cell. 2010;141: 69–80. doi:10.1016/j.cell.2010.02.027

15. Fallahi-Sichani M, Becker V, Izar B, Baker GJ, Lin J, Boswell SA, et al. Adaptive resistance of melanoma cells to RAF inhibition via reversible induction of a slowly dividing de-differentiated state. Molecular Systems Biology. 2017;13: 905. doi:10.15252/msb.20166796

16. Khaliq M, Manikkam M, Martinez ED, Fallahi-Sichani M. Epigenetic modulation reveals differentiation state specificity of oncogene addiction. Nat Commun. 2021;12: 1536. doi:10.1038/s41467-021-21784-2

17. Sequist LV, Waltman BA, Dias-Santagata D, Digumarthy S, Turke AB, Fidias P, et al. Genotypic and Histological Evolution of Lung Cancers Acquiring Resistance to EGFR Inhibitors. Sci Transl Med. 2011;3. doi:10.1126/scitranslmed.3002003

18. Haq R, Shoag J, Andreu-Perez P, Yokoyama S, Edelman H, Rowe GC, et al. Oncogenic BRAF regulates oxidative metabolism via PGC1α and MITF. Cancer Cell. 2013;23: 302–315. doi:10.1016/j.ccr.2013.02.003

19. Obenauf AC, Zou Y, Ji AL, Vanharanta S, Shu W, Shi H, et al. Therapy-induced tumour secretomes promote resistance and tumour progression. Nature; London. 2015;520: 368-372P.

20. Hirata E, Girotti MR, Viros A, Hooper S, Spencer-Dene B, Matsuda M, et al. Intravital imaging reveals how BRAF inhibition generates drug-tolerant microenvironments with high integrin β1/FAK signaling. Cancer Cell. 2015;27: 574–588. doi:10.1016/j.ccell.2015.03.008

21. Fu F, Nowak MA, Bonhoeffer S. Spatial Heterogeneity in Drug Concentrations Can Facilitate the Emergence of Resistance to Cancer Therapy. PLOS Computational Biology. 2015;11: e1004142. doi:10.1371/journal.pcbi.1004142

22. Gorre ME, Mohammed M, Ellwood K, Hsu N, Paquette R, Rao PN, et al. Clinical Resistance to STI-571 Cancer Therapy Caused by BCR-ABL Gene Mutation or Amplification. Science. 2001;293: 876–880. doi:10.1126/science.1062538

23. Solomon BJ, Tan L, Lin JJ, Wong SQ, Hollizeck S, Ebata K, et al. RET Solvent Front Mutations Mediate Acquired Resistance to Selective RET Inhibition in RET-Driven Malignancies. Journal of Thoracic Oncology. 2020;15: 541–549. doi:10.1016/j.jtho.2020.01.006

24. Engelman JA, Zejnullahu K, Mitsudomi T, Song Y, Hyland C, Park JO, et al. MET amplification leads to gefitinib resistance in lung cancer by activating ERBB3 signaling. Science. 2007;316: 1039–1043. doi:10.1126/science.1141478

25. Nazarian R, Shi H, Wang Q, Kong X, Koya RC, Lee H, et al. Melanomas acquire resistance to B-RAF(V600E) inhibition by RTK or N-RAS upregulation. Nature. 2010;468: 973–977. doi:10.1038/nature09626

26. Johannessen CM, Boehm JS, Kim SY, Thomas SR, Wardwell L, Johnson LA, et al. COT drives resistance to RAF inhibition through MAP kinase pathway reactivation. Nature. 2010;468: 968–972. doi:10.1038/nature09627

27. Choi PS, Li Y, Felsher DW. Addiction to multiple oncogenes can be exploited to prevent the emergence of therapeutic resistance. Proceedings of the National Academy of Sciences. 2014;111: E3316–E3324. doi:10.1073/pnas.1406123111

28. Shaffer SM, Dunagin MC, Torborg SR, Torre EA, Emert B, Krepler C, et al. Rare cell variability and drug-induced reprogramming as a mode of cancer drug resistance. Nature. 2017;546: 431–435. doi:10.1038/nature22794

29. Spencer SL, Gaudet S, Albeck JG, Burke JM, Sorger PK. Non-genetic origins of cell-to-cell variability in TRAIL-induced apoptosis. Nature. 2009;459: 428–432. doi:10.1038/nature08012

30. Reyes J, Lahav G. Leveraging and coping with uncertainty in the response of individual cells to therapy. Current Opinion in Biotechnology. 2018;51: 109–115. doi:10.1016/j.copbio.2017.12.007

31. Torre EA, Arai E, Bayatpour S, Jiang CL, Beck LE, Emert BL, et al. Genetic screening for single-cell variability modulators driving therapy resistance. Nat Genet. 2021;53: 76–85. doi:10.1038/s41588-020-00749-z

32. Wouters J, Kalender-Atak Z, Minnoye L, Spanier KI, De Waegeneer M, Bravo González-Blas C, et al. Robust gene expression programs underlie recurrent cell states and phenotype switching in melanoma. Nat Cell Biol. 2020;22: 986–998. doi:10.1038/s41556-020-0547-3

33. Cohen AA, Geva-Zatorsky N, Eden E, Frenkel-Morgenstern M, Issaeva I, Sigal A, et al. Dynamic Proteomics of Individual Cancer Cells in Response to a Drug. Science. 2008;322: 1511–1516.

34. Gaudet S, Spencer SL, Chen WW, Sorger PK. Exploring the Contextual Sensitivity of Factors that Determine Cell-to-Cell Variability in Receptor-Mediated Apoptosis. PLOS Computational Biology. 2012;8: e1002482. doi:10.1371/journal.pcbi.1002482

35. Raj A, Oudenaarden A van. Nature, Nurture, or Chance: Stochastic Gene Expression and Its Consequences. Cell. 2008;135: 216–226. doi:10.1016/j.cell.2008.09.050

36. Sigal A, Milo R, Cohen A, Geva-Zatorsky N, Klein Y, Liron Y, et al. Variability and memory of protein levels in human cells. Nature. 2006;444: 643–646. doi:10.1038/nature05316

37. Zhu R, Rio-Salgado JM del, Garcia-Ojalvo J, Elowitz MB. Synthetic multistability in mammalian cells. 2021 Feb p. 2021.02.10.430659. doi:10.1101/2021.02.10.430659

38. Huang S. On the intrinsic inevitability of cancer: From foetal to fatal attraction. Seminars in Cancer Biology. 2011;21: 183–199. doi:10.1016/j.semcancer.2011.05.003

39. Chang HH, Hemberg M, Barahona M, Ingber DE, Huang S. Transcriptome-wide noise controls lineage choice in mammalian progenitor cells. Nature. 2008;453: 544–547. doi:10.1038/nature06965

40. Santos SDM, Verveer PJ, Bastiaens PIH. Growth factor-induced MAPK network topology shapes Erk response determining PC-12 cell fate. Nat Cell Biol. 2007;9: 324–330. doi:10.1038/ncb1543

41. Symmons O, Raj A. What's Luck Got to Do with It: Single Cells, Multiple Fates, and Biological Nondeterminism. Molecular Cell. 2016;62: 788–802. doi:10.1016/J.MOLCEL.2016.05.023

42. Luria SE, Delbrück M. Mutations of Bacteria From Virus Sensitivity To Virus Resistance. Genetics. 1943;28: 491–511. doi:10.1093/genetics/28.6.491

43. Hata AN, Niederst MJ, Archibald HL, Gomez-Caraballo M, Siddiqui FM, Mulvey HE, et al. Tumor cells can follow distinct evolutionary paths to become resistant to epidermal growth factor receptor inhibition. Nat Med. 2016;22: 262–269. doi:10.1038/nm.4040

44. Roesch A, Vultur A, Bogeski I, Wang H, Zimmermann KM, Speicher D, et al. Overcoming Intrinsic Multidrug Resistance in Melanoma by Blocking the Mitochondrial Respiratory

Chain of Slow-Cycling JARID1Bhigh Cells. Cancer Cell. 2013;23: 811–825. doi:10.1016/j.ccr.2013.05.003

45. Diaz LA, Williams RT, Wu J, Kinde I, Hecht JR, Berlin J, et al. The molecular evolution of acquired resistance to targeted EGFR blockade in colorectal cancers. Nature. 2012;486: 537–540. doi:10.1038/nature11219

46. Turke AB, Zejnullahu K, Wu Y-L, Song Y, Dias-Santagata D, Lifshits E, et al. Preexistence and Clonal Selection of MET Amplification in EGFR Mutant NSCLC. Cancer Cell. 2010;17: 77–88. doi:10.1016/j.ccr.2009.11.022

47. Attolini CS-O, Michor F. Evolutionary Theory of Cancer. Annals of the New York Academy of Sciences. 1168: 23–51. doi:10.1111/j.1749-6632.2009.04880.x

48. Poulikakos PI, Persaud Y, Janakiraman M, Kong X, Ng C, Moriceau G, et al. RAF inhibitor resistance is mediated by dimerization of aberrantly spliced BRAF(V600E). Nature. 2011;480: 387–390. doi:10.1038/nature10662

49. Ramirez M, Rajaram S, Steininger RJ, Osipchuk D, Roth MA, Morinishi LS, et al. Diverse drug-resistance mechanisms can emerge from drug-tolerant cancer persister cells. Nat Commun. 2016;7: 10690. doi:10.1038/ncomms10690

50. Boumahdi S, de Sauvage FJ. The great escape: tumour cell plasticity in resistance to targeted therapy. Nat Rev Drug Discov. 2020;19: 39–56. doi:10.1038/s41573-019-0044-1

51. Pisco AO, Brock A, Zhou J, Moor A, Mojtahedi M, Jackson D, et al. Non-Darwinian dynamics in therapy-induced cancer drug resistance. Nature Communications. 2013;4. doi:10.1038/ncomms3467

52. Lito P, Pratilas CA, Joseph EW, Tadi M, Halilovic E, Zubrowski M, et al. Relief of profound feedback inhibition of mitogenic signaling by RAF inhibitors attenuates their activity in BRAFV600E melanomas. Cancer Cell. 2012;22: 668–682. doi:10.1016/j.ccr.2012.10.009

53. Sun C, Wang L, Huang S, Heynen GJJE, Prahallad A, Robert C, et al. Reversible and adaptive resistance to BRAF(V600E) inhibition in melanoma. Nature. 2014;508: 118–122. doi:10.1038/nature13121

54. Fallahi-Sichani M, Moerke NJ, Niepel M, Zhang T, Gray NS, Sorger PK. Systematic analysis of BRAFV600E melanomas reveals a role for JNK/c-Jun pathway in adaptive resistance to drug-induced apoptosis. Molecular Systems Biology. 2015;11: 797–797. doi:10.15252/msb.20145877

55. Shi H, Hong A, Kong X, Koya RC, Song C, Moriceau G, et al. A novel AKT1 mutant amplifies an adaptive melanoma response to BRAF inhibition. Cancer Discov. 2014;4: 69–79. doi:10.1158/2159-8290.CD-13-0279

56. Britschgi A, Andraos R, Brinkhaus H, Klebba I, Romanet V, Müller U, et al. JAK2/STAT5 Inhibition Circumvents Resistance to PI3K/mTOR Blockade: A Rationale for Cotargeting These Pathways in Metastatic Breast Cancer. Cancer Cell. 2012;22: 796–811. doi:10.1016/j.ccr.2012.10.023

57. Prahallad A, Sun C, Huang S, Di Nicolantonio F, Salazar R, Zecchin D, et al. Unresponsiveness of colon cancer to BRAF(V600E) inhibition through feedback activation of EGFR. Nature. 2012;483: 100–103. doi:10.1038/nature10868

58. Mirzoeva OK, Das D, Heiser LM, Bhattacharya S, Siwak D, Gendelman R, et al. Basal Subtype and MAPK/ERK Kinase (MEK)-Phosphoinositide 3-Kinase Feedback Signaling Determine Susceptibility of Breast Cancer Cells to MEK Inhibition. Cancer Res. 2009;69: 565–572. doi:10.1158/0008-5472.CAN-08-3389

59. Chandarlapaty S, Sawai A, Scaltriti M, Rodrik-Outmezguine V, Grbovic-Huezo O, Serra V, et al. AKT Inhibition Relieves Feedback Suppression of Receptor Tyrosine Kinase Expression and Activity. Cancer Cell. 2011;19: 58–71. doi:10.1016/j.ccr.2010.10.031

60. Rothenberg SM, Concannon K, Cullen S, Boulay G, Turke AB, Faber AC, et al. Inhibition of mutant EGFR in lung cancer cells triggers SOX2-FOXO6-dependent survival pathways. Davis R, editor. eLife. 2015;4: e06132. doi:10.7554/eLife.06132

61. Yang C, Tian C, Hoffman TE, Jacobsen NK, Spencer SL. Melanoma subpopulations that rapidly escape MAPK pathway inhibition incur DNA damage and rely on stress signalling. Nat Commun. 2021;12: 1747. doi:10.1038/s41467-021-21549-x

62. Su Y, Wei W, Robert L, Xue M, Tsoi J, Garcia-Diaz A, et al. Single-cell analysis resolves the cell state transition and signaling dynamics associated with melanoma drug-induced resistance. Proceedings of the National Academy of Sciences. 2017;114: 13679–13684. doi:10.1073/pnas.1712064115

63. Mu P, Zhang Z, Benelli M, Karthaus WR, Hoover E, Chen C-C, et al. SOX2 promotes lineage plasticity and antiandrogen resistance in TP53- and RB1-deficient prostate cancer. Science. 2017;355: 84–88. doi:10.1126/science.aah4307

64. Biehs B, Dijkgraaf GJP, Piskol R, Alicke B, Boumahdi S, Peale F, et al. A cell identity switch allows residual BCC to survive Hedgehog pathway inhibition. Nature. 2018;562: 429–433. doi:10.1038/s41586-018-0596-y

65. Davies AH, Beltran H, Zoubeidi A. Cellular plasticity and the neuroendocrine phenotype in prostate cancer. Nat Rev Urol. 2018;15: 271–286. doi:10.1038/nrurol.2018.22

66. O’Neil NJ, Bailey ML, Hieter P. Synthetic lethality and cancer. Nat Rev Genet. 2017;18: 613–623. doi:10.1038/nrg.2017.47

67. Wang T, Yu H, Hughes NW, Liu B, Kendirli A, Klein K, et al. Gene Essentiality Profiling Reveals Gene Networks and Synthetic Lethal Interactions with Oncogenic Ras. Cell. 2017;168: 890-903.e15. doi:10.1016/j.cell.2017.01.013

68. Bradner JE, Hnisz D, Young RA. Transcriptional Addiction in Cancer. Cell. 2017;168: 629–643. doi:10.1016/j.cell.2016.12.013

69. Wallner L, Dai J, Escara-Wilke J, Zhang J, Yao Z, Lu Y, et al. Inhibition of interleukin-6 with CNTO328, an anti-interleukin-6 monoclonal antibody, inhibits conversion of androgen-dependent prostate cancer to an androgen-independent phenotype in orchiectomized mice. Cancer Res. 2006;66: 3087–3095. doi:10.1158/0008-5472.CAN-05-3447

70. Liau BB, Sievers C, Donohue LK, Gillespie SM, Flavahan WA, Miller TE, et al. Adaptive Chromatin Remodeling Drives Glioblastoma Stem Cell Plasticity and Drug Tolerance. Cell Stem Cell. 2017;20: 233-246.e7. doi:10.1016/j.stem.2016.11.003

71. Ku SY, Rosario S, Wang Y, Mu P, Seshadri M, Goodrich ZW, et al. Rb1 and Trp53 cooperate to suppress prostate cancer lineage plasticity, metastasis, and antiandrogen resistance. Science. 2017;355: 78–83. doi:10.1126/science.aah4199

72. Smith MP, Brunton H, Rowling EJ, Ferguson J, Arozarena I, Miskolczi Z, et al. Inhibiting Drivers of Non-mutational Drug Tolerance Is a Salvage Strategy for Targeted Melanoma Therapy. Cancer Cell. 2016;29: 270–284. doi:10.1016/j.ccell.2016.02.003

73. Zawistowski JS, Bevill SM, Goulet DR, Stuhlmiller TJ, Beltran AS, Olivares-Quintero JF, et al. Enhancer Remodeling during Adaptive Bypass to MEK Inhibition Is Attenuated by Pharmacologic Targeting of the P-TEFb Complex. Cancer Discov. 2017;7: 302–321. doi:10.1158/2159-8290.CD-16-0653

74. Bell CC, Fennell KA, Chan Y-C, Rambow F, Yeung MM, Vassiliadis D, et al. Targeting enhancer switching overcomes non-genetic drug resistance in acute myeloid leukaemia. Nat Commun. 2019;10: 2723. doi:10.1038/s41467-019-10652-9

75. Comandante-Lou N, Baumann DG. AP-1 transcription factor network explains diverse patterns of cellular plasticity in melanoma. Systems Biology; 2021 Dec. doi:10.1101/2021.12.06.471514

76. Angus SP, Stuhlmiller TJ, Mehta G, Bevill SM, Goulet DR, Olivares-Quintero JF, et al. FOXA1 and adaptive response determinants to HER2 targeted therapy in TBCRC 036. npj Breast Cancer. 2021;7: 1–15. doi:10.1038/s41523-021-00258-0

77. Bishop JL, Thaper D, Vahid S, Davies A, Ketola K, Kuruma H, et al. The Master Neural Transcription Factor BRN2 Is an Androgen Receptor–Suppressed Driver of

Neuroendocrine Differentiation in Prostate Cancer. Cancer Discov. 2017;7: 54–71. doi:10.1158/2159-8290.CD-15-1263

78. Verfaillie A, Imrichova H, Atak ZK, Dewaele M, Rambow F, Hulselmans G, et al. Decoding the regulatory landscape of melanoma reveals TEADS as regulators of the invasive cell state. Nat Commun. 2015;6: 6683. doi:10.1038/ncomms7683

79. Echevarría-Vargas IM, Reyes-Uribe PI, Guterres AN, Yin X, Kossenkov AV, Liu Q, et al. Co-targeting BET and MEK as salvage therapy for MAPK and checkpoint inhibitor-resistant melanoma. EMBO Mol Med. 2018;10. doi:10.15252/emmm.201708446

80. Barretina J, Caponigro G, Stransky N, Venkatesan K, Margolin AA, Kim S, et al. The Cancer Cell Line Encyclopedia enables predictive modelling of anticancer drug sensitivity. Nature. 2012;483: 603–607. doi:10.1038/nature11003

81. Garnett MJ, Edelman EJ, Heidorn SJ, Greenman CD, Dastur A, Lau KW, et al. Systematic identification of genomic markers of drug sensitivity in cancer cells. Nature. 2012;483: 570–575. doi:10.1038/nature11005

82. Iorio F, Knijnenburg TA, Vis DJ, Bignell GR, Menden MP, Schubert M, et al. A Landscape of Pharmacogenomic Interactions in Cancer. Cell. 2016;166: 740–754. doi:10.1016/j.cell.2016.06.017

83. Gonçalves E, Segura-Cabrera A, Pacini C, Picco G, Behan FM, Jaaks P, et al. Drug mechanism-of-action discovery through the integration of pharmacological and CRISPR screens. Molecular Systems Biology. 2020;16. doi:10.15252/msb.20199405

84. Goutelle S, Maurin M, Rougier F, Barbaut X, Bourguignon L, Ducher M, et al. The Hill equation: a review of its capabilities in pharmacological modelling. Fundamental & Clinical Pharmacology. 2008;22: 633–648. doi:10.1111/j.1472-8206.2008.00633.x

85. Fallahi-Sichani M, Honarnejad S, Heiser LM, Gray JW, Sorger PK. Metrics other than potency reveal systematic variation in responses to cancer drugs. Nature Chemical Biology. 2013;9: 708–714. doi:10.1038/nchembio.1337

86. Yang R, Niepel M, Mitchison TK, Sorger PK. Dissecting Variability in Responses to Cancer Chemotherapy Through Systems Pharmacology. Clinical Pharmacology & Therapeutics. 2010;88: 34–38. doi:10.1038/clpt.2010.96

87. Hafner M, Niepel M, Sorger PK. Alternative drug sensitivity metrics improve preclinical cancer pharmacogenomics. Nat Biotechnol. 2017;35: 500–502. doi:10.1038/nbt.3882

88. Harris LA, Frick PL, Garbett SP, Hardeman KN, Paudel BB, Lopez CF, et al. An unbiased metric of antiproliferative drug effect in vitro. Nature Methods. 2016;13: 497–500. doi:10.1038/nmeth.3852

89. Hafner M, Niepel M, Chung M, Sorger PK. Growth rate inhibition metrics correct for confounders in measuring sensitivity to cancer drugs. Nature Methods. 2016;13: 521–527. doi:10.1038/nmeth.3853

Chapter 2 Phenotype-Based Probabilistic Analysis of Heterogeneous Responses to Cancer Drugs and Their Combination Efficacy

2.1 Introduction

In pre-clinical studies, potentially effective drug combinations are usually identified based on evidence of synergy [1–4]. In the case of cancer drugs, synergistic interactions are typically assessed on the basis of bulk cell population measurements, such as relative viability (normalized cell count) and net growth rate inhibition, and their variations with drug dose and combination [5–9]. The benefit of drug combination is then evaluated based on whether using two drugs together improves the potency (via minimizing the dose) or efficacy of treatment (via enhancing the effect) as compared with using either of the drugs alone [10–16]. Such benefit with respect to efficacy and potency, however, may be decoupled [10], as each metric encodes distinct information about cellular response to a drug [17]. Variations in potency are often explained by differences in target engagement (e.g. physicochemistry of drug-target interaction), concentration of drug available to cells (e.g. drug uptake and efflux), or existence of pathway redundancy (e.g. presence of a secondary oncogenic driver), among others [18]. Thus, a more potent drug combination enables engaging the target and achieving the desired effect in a cell population by using lower doses of treatment [19,20]. Efficacy, on the other hand, refers to the maximum response achievable using tolerable doses of a drug. A more efficacious drug or drug combination engages a larger proportion of cells [21,22]. Previous systematic studies have revealed that variation in cancer drug efficacy is associated with the extent of cell-to-cell variability in drug response [17,23], although such heterogeneity is not directly scored in most pre-clinical drug response assays.

Cell-to-cell variability may generate subpopulations of drug-tolerant cells that diminish cancer drug efficacy [24–30]. An example of such heterogeneity is observed following the emergence of adaptive resistance or selection of resistant sub-clones even in populations of cells that are scored as highly responsive based on drug potency (e.g. EC_{50} measurements) in routine 3 to 5-day assays. In such cases, while more than half (often as many as 90-99%) of cells may respond to treatment (depending on time and dose), the remaining cells give rise to a drug-insensitive subpopulation of survivors that may stay quiescent or divide slowly in the presence of drug [31]. Although not obvious from the most commonly used potency measurements, the emergence of such survivors limits therapeutic efficacy, leading to residual cells from which drug-resistant clones may eventually arise and drive disease progression [32–35]. Overcoming such heterogeneity in drug response and eradicating subpopulations of drug-tolerant cells provide a strong motivation for identifying more efficacious combination therapies [36]. A key step toward this goal is the ability to distinguish how heterogeneous populations of cells respond to individual drugs in short-term assays, and how these responses are influenced by combined drug interactions. However, the standard way in which drugs or their combinations are screened using normalized population assays obscures single-cell and subpopulation effects that likely play a major role in diminishing the therapeutic efficacy [21,37].

Focusing on efficacy, the benefit of drug combination in a heterogeneous population of cells may arise either from its cooperative inhibitory effect on target cells [22], or simply from the increased probability of cells being sensitive to any of the constituent drugs [38]. In both cases, the overall phenotypic consequences of drug interactions may be assessed in cell culture experiments based on null models of non-interaction [3]; synergistic efficacy is typically concluded when the observed combinatorial effect exceeds the expected effect from a given null model. The most commonly used model, Bliss independence, evaluates interactions based on the probability theory for statistically independent drug actions [16]. In cancer treatment, two basic phenotypic events affected by drug action are cell death and division. The effect of a drug on an individual cell changes the probability of its survival or division within a given time interval. However, current application of the Bliss independence typically uses fraction of cells affected (f_a), a number between zero and one defined based on relative viability or net growth rate inhibition normalized to an untreated control at a fixed timepoint, as drug effect [3,7]. We argue that this commonly used approach leads to a bias in the estimation of both drug efficacy and combination effectiveness in heterogeneous cell populations, especially when the ultimate goal is to block or eradicate small subpopulations of drug-tolerant cells. This is because f_a quantities are not equal to the time-dependent probabilities at which cell death or inhibition of cell division are induced by a drug.

In this paper, we discuss evaluating time-dependent drug responses based on probabilistic metrics that quantify drug-induced tumor cell killing and inhibition of division at a single-cell level. Using these phenotype metrics, we re-evaluate criteria for statistical independence of drug interactions based on probability theory. Experimentally, phenotype metrics are measured using time-lapse live cell microscopy via monitoring cells engineered to express fluorescent reporters for nucleus identification (to distinguish live versus dead cells) and cell cycle progression (to score division events). As a proof of concept, we evaluate the performance of the metrics in two BRAF-mutant melanoma cell lines exposed to a range of targeted drugs which have been tested or proposed to be studied in combination with standard of care BRAF and MEK kinase inhibitors. Dynamic measurements of the phenotype metrics reveal distinctive responses of melanoma cells to drug combinations that may not be distinguishable when assessed based on conventional assays. This is because these metrics deconvolve differential degrees of drug effect on tumor cell killing versus inhibition of division, which are not necessarily correlated across various drug treatments and their combinations. Furthermore, these metrics increase the sensitivity of short-term drug response assays to cell-to-cell heterogeneities and thus the presence or emergence of drug-tolerant subpopulations, which are typically overlooked in conventional drug response assays.

2.2 Results

2.2.1 Probabilistic description of drug-induced phenotypic events

We model the arrival of phenotypic events, including cell division and death, in a given cell population as independent non-stationary *Poisson* processes with time-varying rate constants (k_{event}). These rate constants are linked to the actual probabilities (P_{event}) with which such events occur in individual cells within a series of short time intervals (dt):

$$P_{event} = 1 - e^{-k_{event}dt} \approx k_{event}dt \qquad \text{(Equation 2.1)}$$

At a population level, the occurrence of these phenotypic events can be described by *Poisson* processes of which the time-dependent rates of occurrence are directly related to the probabilities of events at a single-cell level (Figure 2.1). Therefore, the distribution of death and division events observed for a population of N cells during a time period of Δt may be approximated using the following equation:

$$P\{N_{event}(t \rightarrow t + \Delta t) = x\} = \frac{(k_{event}(t)N\Delta t)^{x}}{x!} e^{-(k_{event}(t)N)\Delta t} \qquad \text{(Equation 2.2)}$$

where N_{event} $(t \rightarrow t + \Delta t)$ is the number of phenotypic events (death or division) occurring during the time interval between t and $t + \Delta t$.

Assuming negligible cell death in the absence of any treatment, the model describes the cytotoxic effect of a drug on a given cell by the probability with which it induces cell death per unit of time ($P_{death} = k_{death}dt$). The cytostatic effect of drug on a given cell is defined by a conditional probability (P_{stasis}) with which it prevents the cell from dividing given that the same cell would have divided in the absence of drug with a probability of $P_{division\ (no\ drug)} = k_{division\ (no\ drug)}dt$. The relationships between the conditional probability P_{stasis} and the probability of cell division in the presence of drug ($P_{division\ (with\ drug)} = k_{division\ (with\ drug)}dt$) and their associated rate constants are as follows (see Materials and Methods for the derivation details):

$$P_{stasis} = 1 - \frac{P_{division\ (with\ drug)}}{P_{division\ (no\ drug)}} = 1 - \frac{k_{division\ (with\ drug)}}{k_{division\ (no\ drug)}} \qquad \text{(Equation 2.3)}$$

$$k_{stasis} = P_{stasis} k_{division\ (no\ drug)} \qquad \text{(Equation 2.4)}$$

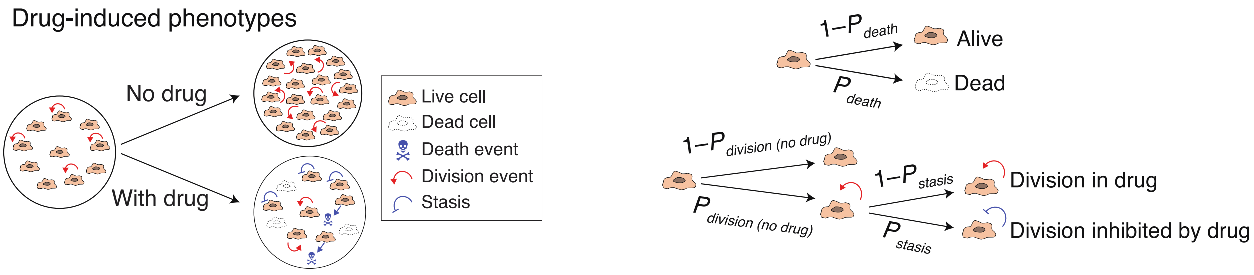

Figure 2.1 Schematic representation of phenotypic effects of drug action in a cell population.

Drug effect is described as probabilistic events, involving induction of cell death and inhibition of cell division, at a single-cell level. Cytotoxic effect of a drug on a given cell is described by the probability with which it induces cell death per unit of time (P_{death}). The cytostatic effect of drug on a given cell is described by a conditional probability (P_{stasis}) with which it prevents the cell from dividing given that the same cell would have divided in the absence of drug with a probability of $P_{division\ (no\ drug)}$.

The model provides a framework to simulate how dose-dependent responses in populations of cells vary with P_{death} per unit of time (h) and P_{stasis} by using input parameters

(k_{death} and k_{stasis}) that represent drugs with a wide range of cytotoxic and cytostatic effects. For each condition, the fraction of cells affected (f_a), defined based on changes in relative viability or net growth rate inhibition (using recently developed drug-induced proliferation (DIP) and growth rate (GR) inhibition metrics [5,6]) normalized to an untreated control, are also derived as model outputs (Figure 2.2).

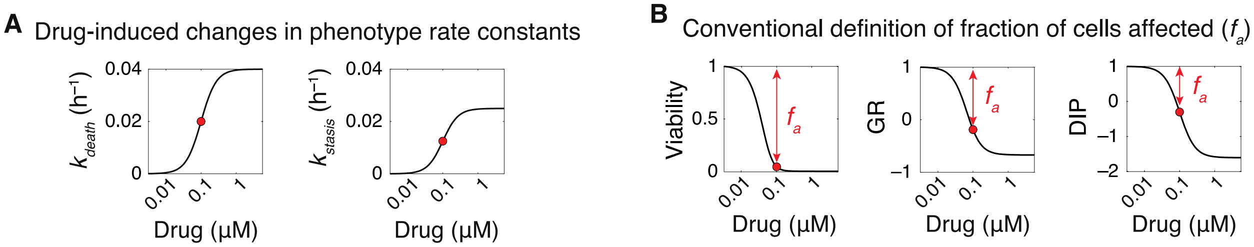

Figure 2.2 Input and output of the model simulating dose-dependent responses in a cell population.

(A) Dose-dependent changes in phenotype rate constants (k_{death} and k_{stasis}) in simulation of drug effect in a population of cells. **(B)** Model outputs showing variations in the fraction of cells affected (f_a) at t = 96 h corresponding to phenotype rate constant values shown in (A). f_a may be calculated in three different ways based on bulk response metrics such as relative viability and net growth rate inhibition (GR and DIP) following normalization to an untreated control.

We compared f_a quantities with probabilistic measures of drug action (P_{death} and P_{stasis}) across a number of drug response simulations. Except for extreme cases such as when $P_{death} = P_{stasis} = 0$ (i.e. there is no drug) or when $P_{death} = 1$ (i.e. all cells dying within the first time interval), f_a quantities differed substantially from the probability with which drugs induced cell death or from the probability with which they inhibited cell division (Figure 2.3). f_a gives a closer estimate of the overall probability with which a drug induces either cell death or inhibition of cell division ($P_{death \cup stasis}$), i.e. the probability of a cell being affected (Figure 2.3). However, it still fails to accurately represent the probabilistic nature of drug action in cells. Together, simulation results suggest that using f_a as a metric for probabilistic analysis of drug response or drug combination efficacy (such as in Bliss independence) might lead to unreliable conclusions.

Instead, we propose to use direct measures of probabilistic phenotype metrics (P_{death} and P_{stasis} or k_{death} and k_{stasis}) for such analyses.

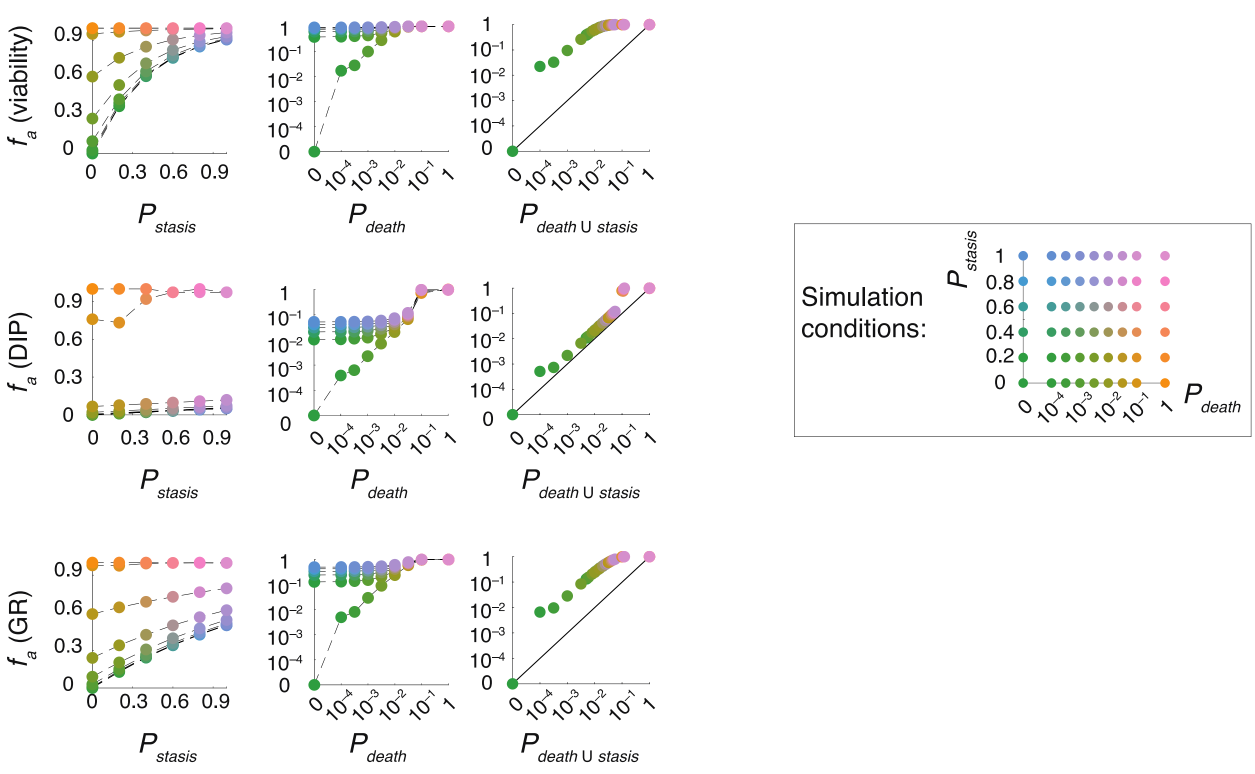
Probability of drug effect versus fraction of cells affected (f_a)

Figure 2.3 f_a quantities do not capture probabilities of drug action.

Simulation results comparing f_a quantities at t = 96 h with probabilistic measures of drug action, P_{death} quantified per unit of time (h) and conditional probability P_{stasis}, and the overall probability with which a drug induces cell death or inhibits cell division ($P_{death \cup stasis}$) across a variety of conditions, representing drugs with different levels of cytotoxic and cytostatic effect. Each data-point represents the mean of 30 stochastic simulations. Cells grow from an initial number of N_{live} (t = 0) = 1000 and at a rate of $k_{division\ (no\ drug)}$ = 0.025 h^{-1}.

2.2.2 Probabilistic rate constants capture time-dependent heterogeneities in phenotypic responses

Probabilistic rate constants are estimated based on the frequencies of occurrence of individual phenotypic events. These metrics are expected to exhibit high sensitivity to the presence of cell-to-cell heterogeneities that cause the selection of small subpopulations of drug-tolerant cells. To test this hypothesis, we simulated drug treatment scenarios where the initial cell population consisted of heterogeneous subpopulations, in which a small fraction ($\omega \leq 5\%$) of cells were substantially less sensitive (by up to r = 16-fold) to treatment relative to the majority of the cell population (Figure 2.4). We then defined and calculated "resistance enrichment ratio" for each of the f_a metrics (described based on viability, GR and DIP) or for phenotype rate constants (k_{death} and k_{stasis}) by normalizing each metric measured for the heterogeneous population to that in a homogeneous population (i.e. $\omega = 0$ or $r = 1$) at different times of treatment. Smaller resistance enrichment ratios represent greater sensitivity to the presence of heterogeneous drug-tolerant cells.

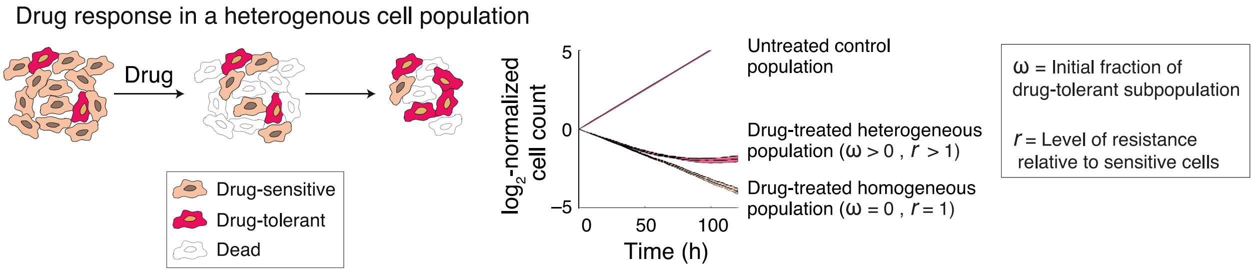

Figure 2.4 Schematic representation of drug response in a heterogeneous cell population and the key model parameters used to model such population.

Prior to drug-treatment, cells consist of a dominantly drug-sensitive population plus a small fraction ($\omega \leq 5\%$) of drug-tolerant subpopulation which is r times more drug-resistant than the majority of cells. Upon drug treatment, the drug-tolerant subpopulation is gradually enriched over time. Resistance enrichment ratio for each of the f_a metrics (described based on viability, GR and DIP) or for phenotype rate constants (k_{death} and k_{stasis}) is calculated by normalizing each metric measured for a heterogeneous population to that in a homogeneous population (i.e. $\omega = 0$ or $r = 1$) at different times of treatment. Smaller resistance enrichment ratios represent greater sensitivity to the presence of heterogeneous drug-tolerant cells.

We first compared the ability of each metric to capture the presence of small subpopulations of drug-tolerant cells by analyzing how resistance enrichment ratio varies with ω and time (Figure 2.5 A-C). Simulation results show that f_a metrics, defined based on either normalized cell viability or growth rate inhibition (GR and DIP), are significantly less sensitive than k_{death} and k_{stasis} to the presence of drug-tolerant cells. Furthermore, for any given initial fraction of drug-tolerant cells (ω), phenotype rate constants captured the emergence of drug resistance at earlier timepoints. Using similar simulations, we also tested how the relative level of drug resistance (r) in a fixed initial fraction of drug-tolerant cells would influence each of the drug response metrics. Simulation results show that for a given ω, phenotype rate constants detect subpopulations with weaker levels of resistance (i.e. smaller r values) and at earlier timepoints (Figure 2.5 D-F).

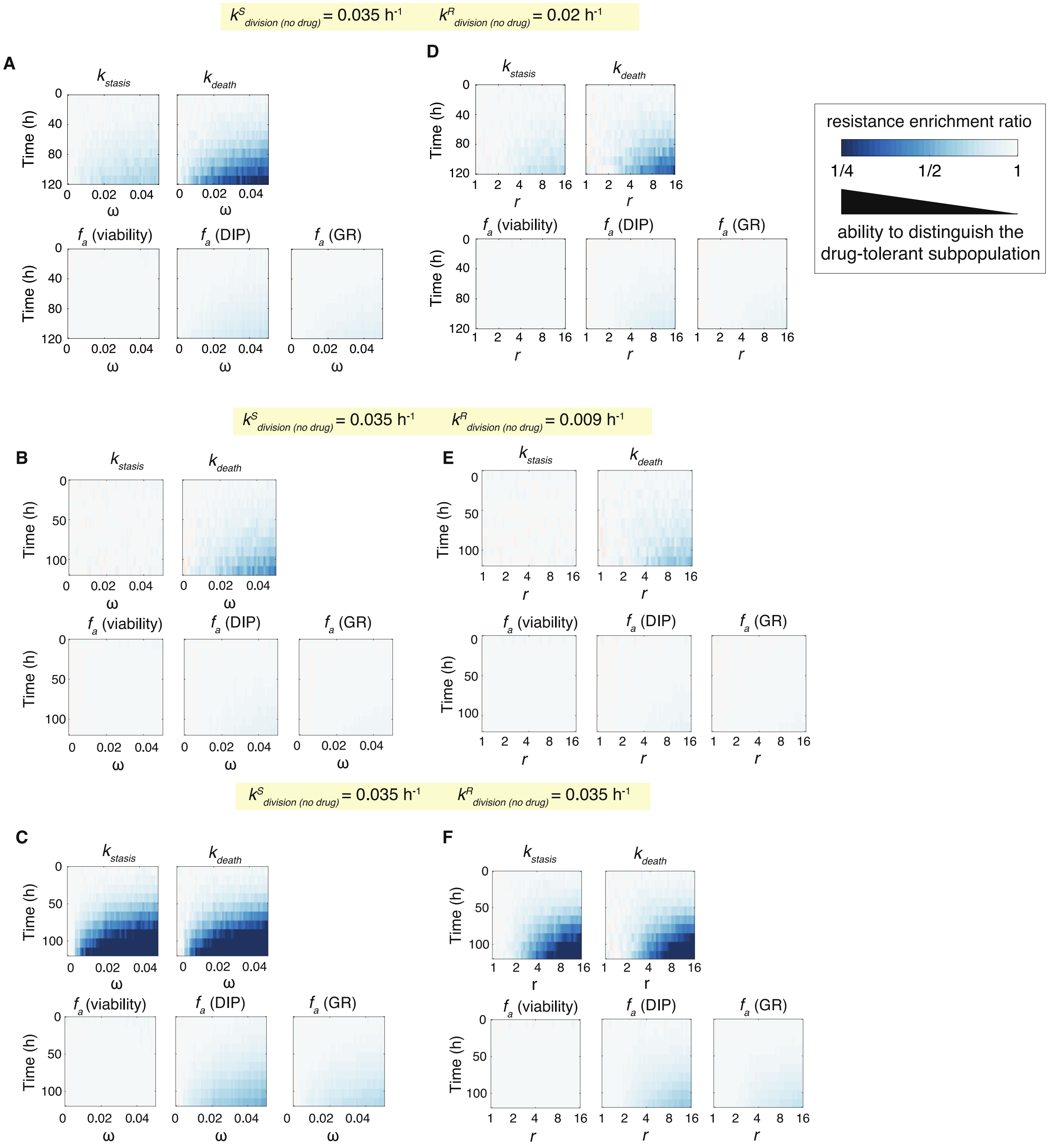

Figure 2.5 Probabilistic rate constants capture time-dependent heterogeneities in phenotypic responses

(A-C) Simulation results showing changes in resistant enrichment ratio calculated for each of the f_a metrics and for phenotype rate constants (k_{death} and k_{stasis}) as a function of ω (at a fixed value of r = 16) across different times of treatment. Data are shown for fixed inherent growth rates for the sensitive population, $k^S_{division\ (no\ drug)}$ = 0.035 h^{-1} and three different rates of inherent growth rate for the resistant subpopulation: $k^R_{division\ (no\ drug)}$ = 0.02 h^{-1} (A), $k^R_{division\ (no\ drug)}$ = 0.009 h^{-1} (B) and $k^R_{division\ (no\ drug)}$ = 0.035 h^{-1} (C). **(D-F)** Simulation results showing changes in resistant enrichment ratio calculated for each of the f_a metrics and for phenotype rate constants (k_{death} and k_{stasis}) as a function of r (at a fixed value of ω = 0.03) across different times of treatment. Data are shown for fixed inherent growth rates for the sensitive population, $k^S_{division\ (no\ drug)}$ = 0.035 h^{-1} and three different rates of inherent growth rate for the resistant subpopulation: $k^{R}_{division\ (no\ drug)} = 0.02\ h^{-1}$ (D), $k^{R}_{division\ (no\ drug)} = 0.009\ h^{-1}$ (E) and $k^{R}_{division\ (no\ drug)} = 0.035\ h^{-1}$ (F). All data represent mean values from 50 simulations.

Most conventional drug screening assays are performed following exposure of cells to drug for 3 to 5 days. While variations in drug potency are distinguishable in such assays, it is often suggested that longer periods of treatment are essential to detect the phenotypic consequences of drug-tolerant persisters that diminish the efficacy. However, our results show that phenotype rate constants can capture heterogeneities that would otherwise require significantly longer experiments when using population-level f_a metrics that mask such heterogeneities. The benefit of using phenotype rate constants would be especially significant in the case of potent drugs that induce substantial cell death, while sparing a small fraction of drug-tolerant cells (Figure 2.6 A,B). In particular, as the efficiency of drug-induced cell killing increases, the sensitivity of f_a metrics to detect drug tolerance in the surviving fraction of cells decreases (Figure 2.6C).

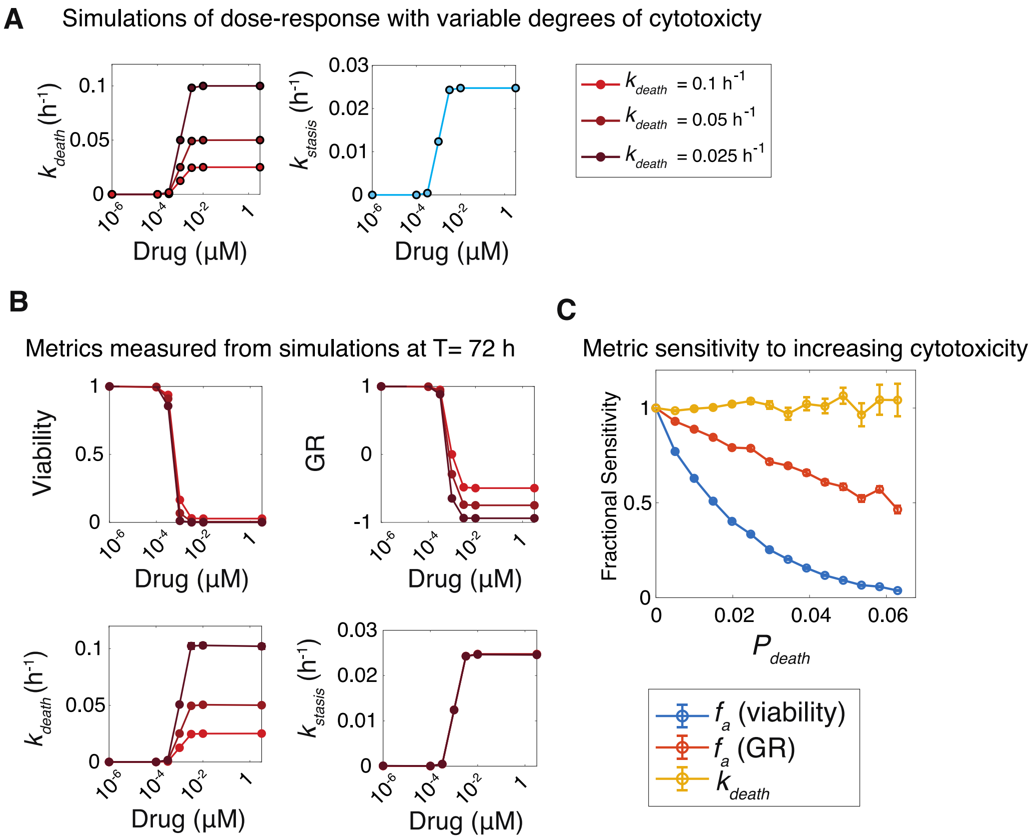

Figure 2.6 Sensitivity of f_a metrics decreases as drug cytotoxicity increases.

(A) Input dose response profiles used in simulations. The maximum cytotoxic efficacy was varied at three different levels, whereas the cytostatic dose response profiles for all three conditions were held constant. **(B)** Model output measured from the simulated conditions in (A) at t = 72 h showing variations in viability, GR and the probabilistic phenotype rate constants. **(C)** Analysis of metric sensitivity with varying drug cytotoxicity parameter P_{death}, quantified per unit of time (h). Sensitivity analysis was performed on simulations with P_{stasis} = 0 and $k_{division\ (no\ drug)}$ = 0.035 h^{-1}. Initial cell number was $N_{live}(t = 0) = 5000$. Data shown are mean ± SEM across 50 simulations. Probabilistic phenotype rate constants were estimated from a 24 h time-interval centered at 72 h.

2.2.3 Estimating probabilistic rate constants using time-lapse live cell microscopy

To experimentally capture stochastic processes of induction of cell death and inhibition of division in drug-treated tumor cell populations, we used time-lapse live cell microscopy and cells engineered to express two fluorescent reporters. The reporters included: (i) an H2B-Venus reporter which labels chromatin, allowing identification of nuclei and scoring cell death based on changes in nucleus morphology, and (ii) an mCherry-Geminin reporter for cell cycle progression

[39] which allows tracking of cell division events. Using a high-throughput, automated image analysis workflow (see Materials and Methods), the occurrence of individual phenotypic events (death and division) in single cells was tracked in time across a variety of drug treatment conditions (Figure 2.7). To estimate time-dependent changes in probabilistic phenotype rate constants, the number of cell death and division events (N_{event}) were quantified over a series of uniform time intervals of length Δt. Phenotype rate constants were then estimated via normalizing N_{event} in each time interval to the length (Δt) and the average number of live cells over that time interval $[N_{live}(t \rightarrow t + \Delta t)]_{avg}$ as detailed below:

$$k_{death}(t) = \frac{N_{death}(t \rightarrow t + \Delta t)}{[N_{live}(t \rightarrow t + \Delta t)]_{avg} \Delta t} \quad \text{(Equation 2.5)}$$

$$k_{division}(t) = \frac{N_{division}(t \rightarrow t + \Delta t)}{[N_{live}(t \rightarrow t + \Delta t)]_{avg} \Delta t} \quad \text{(Equation 2.6)}$$

$$k_{stasis}(t) = k_{division\ (no\ drug)} - k_{division\ (with\ drug)}(t) \quad \text{(Equation 2.7)}$$

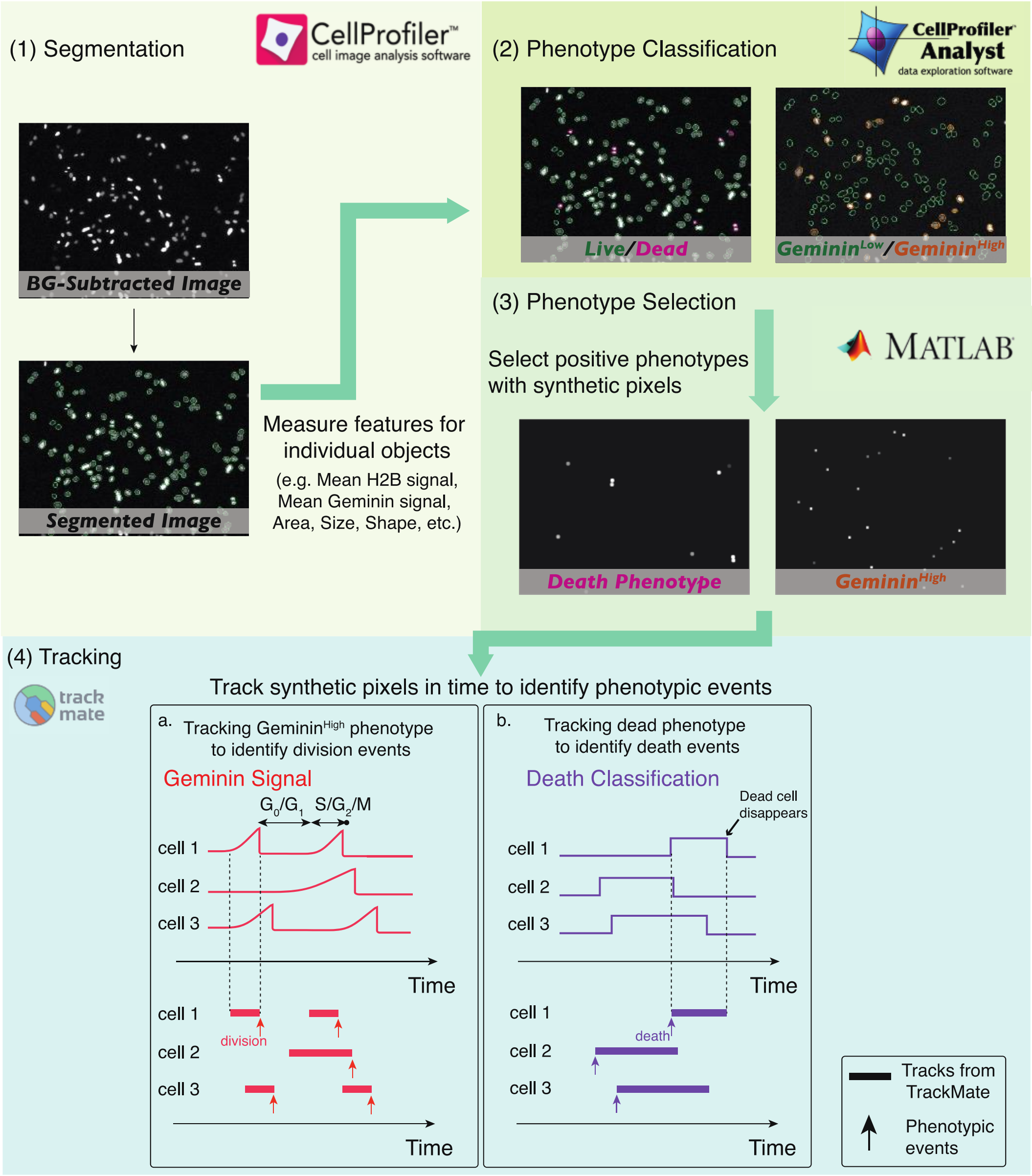

Figure 2.7 Overview of the time-lapse image analysis pipeline to quantify occurrence of single-cell phenotypic events from time-lapse live cell microscopy data.

The automated image analysis pipeline involves four steps: (1) Each background (BG) subtracted H2B image was segmented in CellProfiler for nucleus identification. For each nucleus object, a variety of features (e.g. mean signal intensities across multiple channels, area and shape) were measured. (2) To classify the phenotypes of interest (i.e. live or dead cells, Gemininhigh or Gemininlow cells) in each image, classification models were trained in CellProfiler Analyst based on feature measurements of the user-annotated training sets. (3) Based on phenotype classifications of individual cells for each image output from CellProfiler, corresponding synthetic images were generated in MATLAB for each phenotype of interest. Synthetic images contained synthetic pixels at locations of Gemininhigh or dead cells. To facilitate tracking of individual cells, relative intensities of the synthetic pixels for each phenotype were scaled with the mean intensity of the signal associated with that phenotype. For example, intensities of death synthetic pixels were scaled with the mean H2B signal intensities of individual cells, whereas intensities of the Gemininhigh synthetic pixels were scaled with the mean Geminin signal intensities. (4) Synthetic pixels for each phenotype were tracked separately in TrackMate. Since Geminin reporter level drops at the M phase, a division event is marked when the Geminin track ends. The beginning of a death track is also marked as a death event.

As a proof of concept, we monitored responses of two BRAF-mutated melanoma cell lines (COLO858 and MMACSF) following exposure to a BRAF inhibitor Vemurafenib at 6 doses for a period of ~120 h. Heterogeneity in drug response was then visualized through the estimation and analysis of phenotype rate constants, k_{death} and k_{stasis}, as a function of drug dose and time in each cell line (Figure 2.8A, B). In COLO858 cells, which have been shown to be initially sensitive but rapidly develop adaptive resistance to Vemurafenib [21,22], increasing drug concentration enhanced both the amplitude and the rate of increase in k_{death} and k_{stasis} within the first 36 h. After that, these responses were attenuated concurrent with the activation of drug-induced adaptive responses (Figure 2.8A). Responses of MMACSF cells involved a relatively monotonic and dose-dependent decrease in the number of live cells. At the highest drug concentration (3.2 μM), however, we observed two peaks of apoptotic response, one similar to COLO858 cells at $t \approx 36$ h and a higher peak later at $t \approx 108$ h (Figure 2.8B). These data are consistent with previous data reporting high sensitivity of MMACSF cells to 5 days of exposure to Vemurafenib [21,22], but also highlight the impact of cell-to-cell heterogeneity and the presence of subpopulations of cells with different levels of drug tolerance.

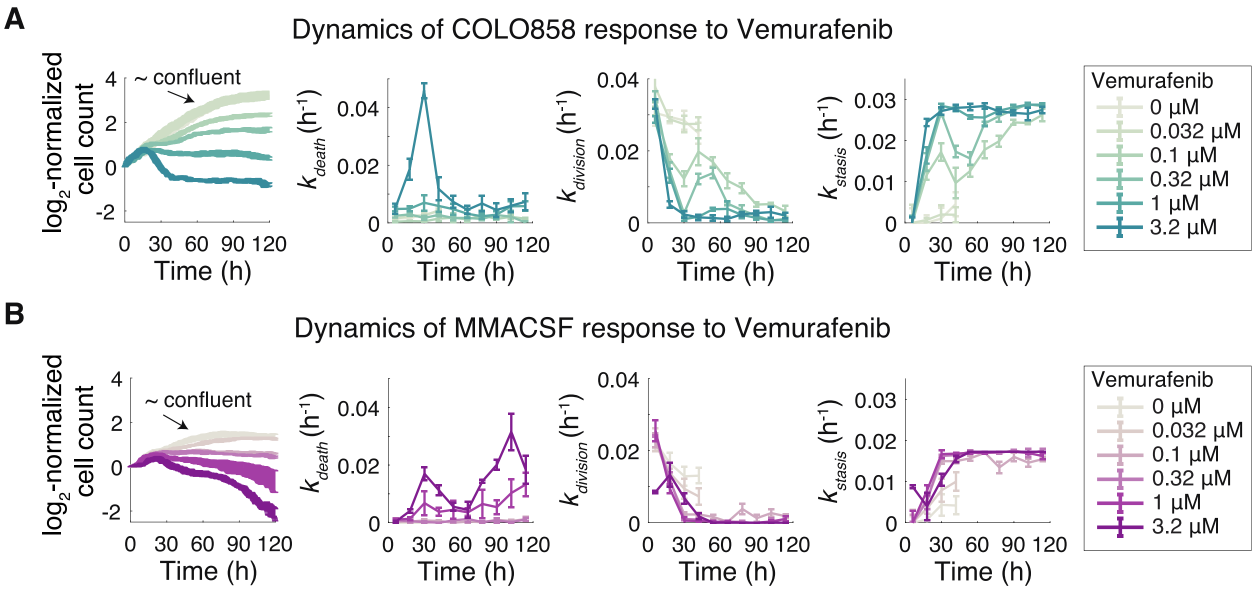

Figure 2.8 Dynamic analysis of heterogeneous drug response using estimates of probabilistic phenotype rate constants from time-lapse live cell microscopy.

(A-B) Dynamics of (A) COLO858 and (B) MMACSF cell responses to BRAF inhibitor Vemurafenib across 6 doses (0-3.2 µM). Time- and dose-dependent changes in live cell count and estimates of k_{death}, $k_{division}$ and k_{stasis} for time intervals of Δt = 12 h are shown. Experimental data for Vemurafenib concentrations of 0 and 0.032 µM are shown until 48 h, that is when cells reached confluency under these conditions. Data are shown as mean ± SEM across four replicates.

In addition to interrogating dynamic aspects of heterogeneous drug response, we also tested the performance of our automated image analysis workflow by comparing the estimated phenotype rate constants with those measured from data generated by manual single-cell tracking using a MATLAB-based software [40]. The software allowed accurate tracking and cell fate annotation of individual cells across time-lapse images taken over a period of multiple days. Single-cell profiles from manual tracking confirmed heterogeneity in the number and timing of death and division events in cells exposed to drug. In COLO858, for example, cell-to-cell variability ranged from cells that died rapidly (as early as ~24 h) in response to high concentrations of Vemurafenib, to cells that survived but did not divide, to cells that slowly divided following a temporary delay in their cell cycle, the proportion and dynamics of which changed with drug dose (Figure 2.9A). By comparing rate constants between two image analysis methods across a variety of conditions in two cell lines, we identified quantitatively similar patterns (Figure 2.10). This consistency confirms that the automated workflow would be suitable for high-throughput analysis of drug response.

We also used single-cell phenotype data to empirically evaluate the assumption of non-stationary *Poisson* process to model drug-induced death and division events. We compared the distribution of phenotypic events measured from time-lapse microscopy experiments with those simulated based on *Poisson* processes using estimates of phenotype rate constants. We observed similarity across patterns of response at the single-cell level and between distributions of events at the population level (Figure 2.9), suggesting that a simplified model of non-stationary *Poisson* process for drug-induced death and division events is a reasonable one.

Taken together, high-throughput estimation and analysis of phenotype rate constants and their changes with time and dose provide an efficient tool to capture critical dynamic aspects of probabilistic and heterogeneous drug response that would be overlooked in bulk population assays.

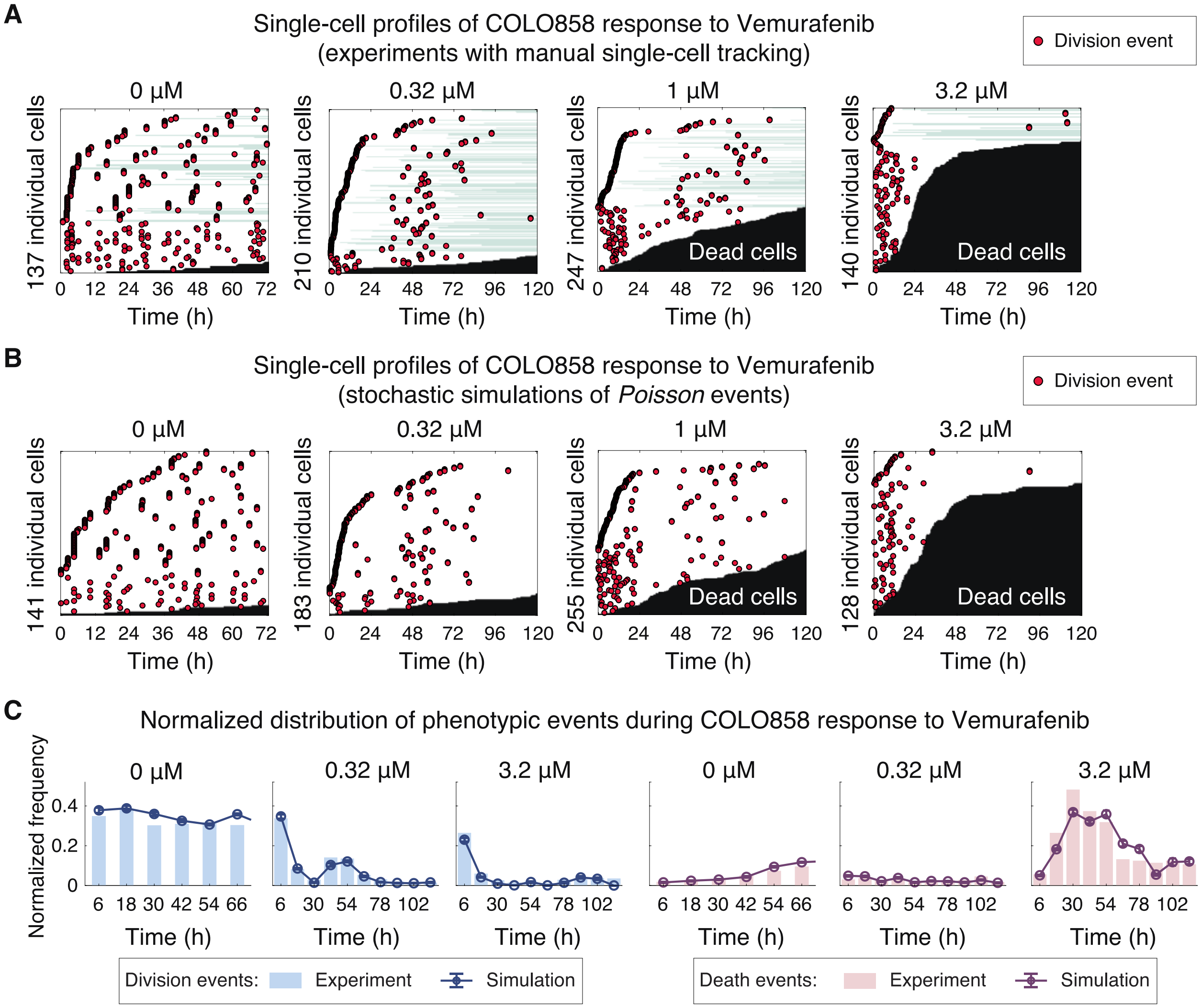

Figure 2.9 Simulations based on Poisson processes recapitulate the cell-to-cell variability of phenotypic drug-responses and distributions of phenotypic events observed experimentally.

(A) Single-cell profiles of COLO858 response to Vemurafenib depicted based on manual tracking of individual cells exposed to different concentrations of Vemurafenib as described in (Figure 2.8A). Each cell track is presented horizontally along time axis. Division events are marked as red circles. Transition from white to black represents a cell death event. Times at which cells spend out of field of view are shown in light green. **(B)** Single-cell profiles of COLO858 response to Vemurafenib simulated based on *Poisson* processes using rate parameters estimated from COLO858 experimental data along 12 h time intervals. **(C)** Comparison of normalized distributions of division and death events along 12 h time intervals between experiments performed in COLO858 cells and the simulated responses for the same conditions. Experimental data-points represent pooled data from all four replicates. Simulated data-points represent mean ± SEM across 30 simulations.

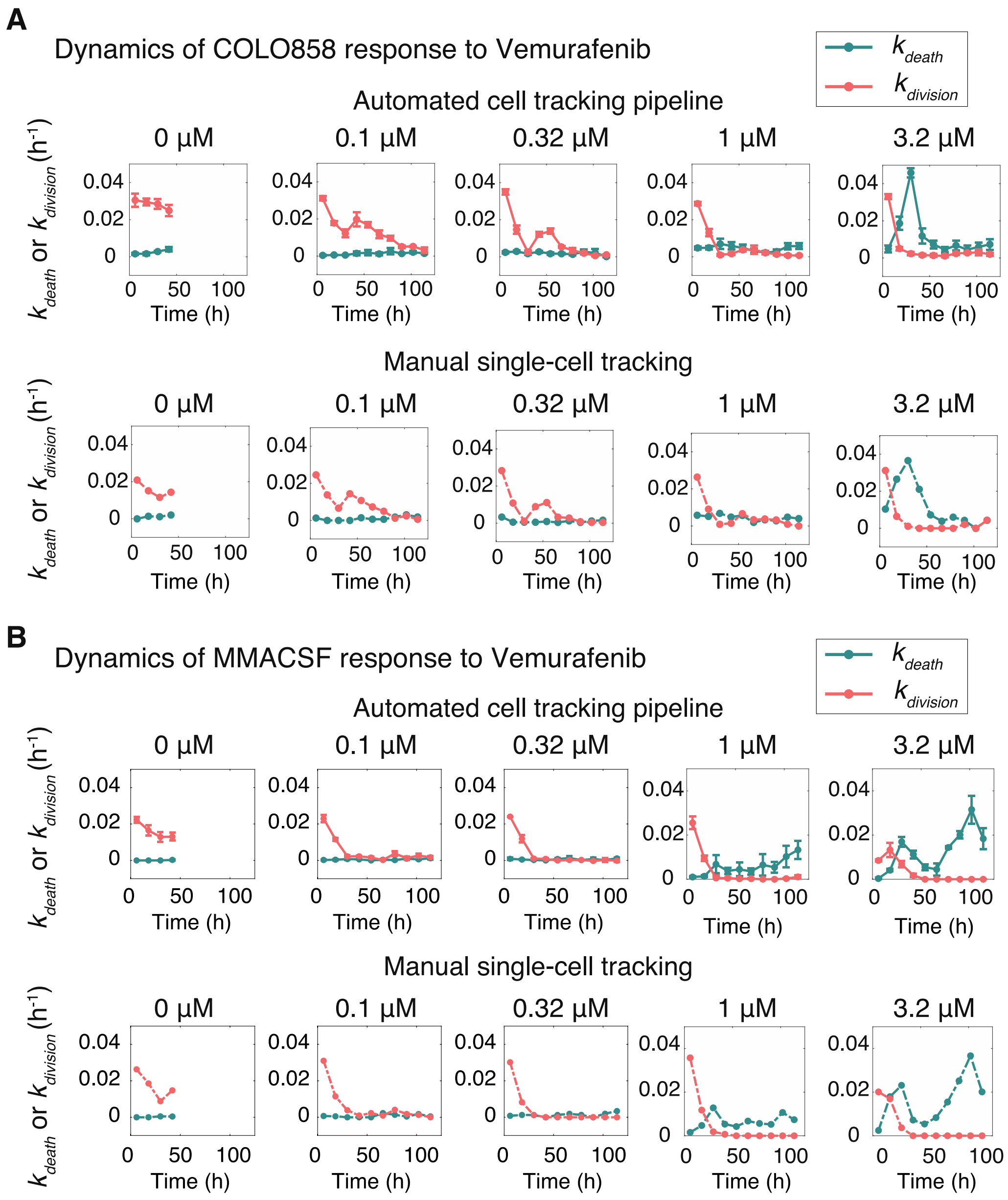

Figure 2.10 Probabilistic rate constants of phenotypic events measured using automated tracking is consistent with the rate constants acquired from manual single-cell tracking across different cell lines and drug conditions.

(A-B) Probabilistic rate constants of death (k_{death}) and division events ($k_{division}$) measured in (A) COLO858 and (B) MMACSF cells treated with Vemurafenib at the indicated doses, using automated tracking analysis pipeline (top row) versus manual tracking (bottom row) on the same set of time-lapse images. For each condition, the automated tracking estimates at each timepoint are the mean values across four replicated wells. Error bars represent SEM. The rate constants calculated from manual tracking data are based on individually tracked cells pooled from four replicated wells, including about 150-220 cells per condition.

2.2.4 Evaluating statistical independence of drug combination efficacies using probabilistic phenotype metrics

Among the most widely used reference models in evaluation of synergistic efficacy for cancer drug combinations is Bliss independence [16]. The Bliss model assumes that drug effects are consequences of probabilistic processes, and that two drugs act independently if their combined effect confers probabilistic or statistical independence:

$$P^{I}_{A+B} = P_{A} + P_{B} - P_{A}P_{B} \qquad \text{(Equation 2.8)}$$

where P^{I}_{A+B} describes the expected probability of the combinatorial effect of drugs A and B when they act independently. $0 \leq P_A \leq 1$ and $0 \leq P_B \leq 1$ represent probabilities of effect mediated by drugs A and B when tested individually. The Bliss combination index (CI) for drugs A and B is defined as:

$$CI^{Bliss}_{A+B} = \frac{P^{I}_{A+B}}{P_{A+B}} \qquad \text{(Equation 2.9)}$$

where P_{A+B} describes the actual probability of effect induced by drugs A and B when used in combination. Synergistic combination efficacy is concluded if $CI < 1$, i.e. when the observed combinatorial effect exceeds the expected effect from the Bliss independence model. Despite its probabilistic definition, however, the Bliss model is broadly applied to a variety of f_a metrics (such as normalized viability or net growth rate inhibition), thereby leading to unreliable conclusions which are largely due to the following limitations. First, although f_a measurements satisfy the mathematical requirement of $0 \leq f_a \leq 1$, they do not have a probabilistic nature and thus do not necessarily follow the rules of probability theory. Second, f_a quantities are the result of two distinct probabilistic processes, induction of cell death and inhibition of cell division. These processes, even when induced by drugs with the same probabilities, do not necessarily have the same impact on f_a. Third, for drugs A and B with $f_a < 1$, the Bliss model (when applied to f_a) is unable to account for the difference between being affected by drug A, drug B, or both. For example, consider the combined effect of two truly independent and purely cytostatic drugs

A and B, whose phenotypic effects (individually) are described by $P_{stasis} = 1$ (and $P_{death} = 0$). By Bliss independence when applied to f_a metrics such as viability or normalized growth rate inhibition, the combination of drugs A and B is expected to exhibit substantial cytotoxic effect and thus their combination would be scored incorrectly as antagonistic ($CI > 1$) (Figure 2.11). To overcome such limitations and to avoid erroneous conclusions about drug combination efficacies, we propose to use probabilities of phenotypic events or their associated rate constants in evaluation of Bliss independence according to its probabilistic definition.

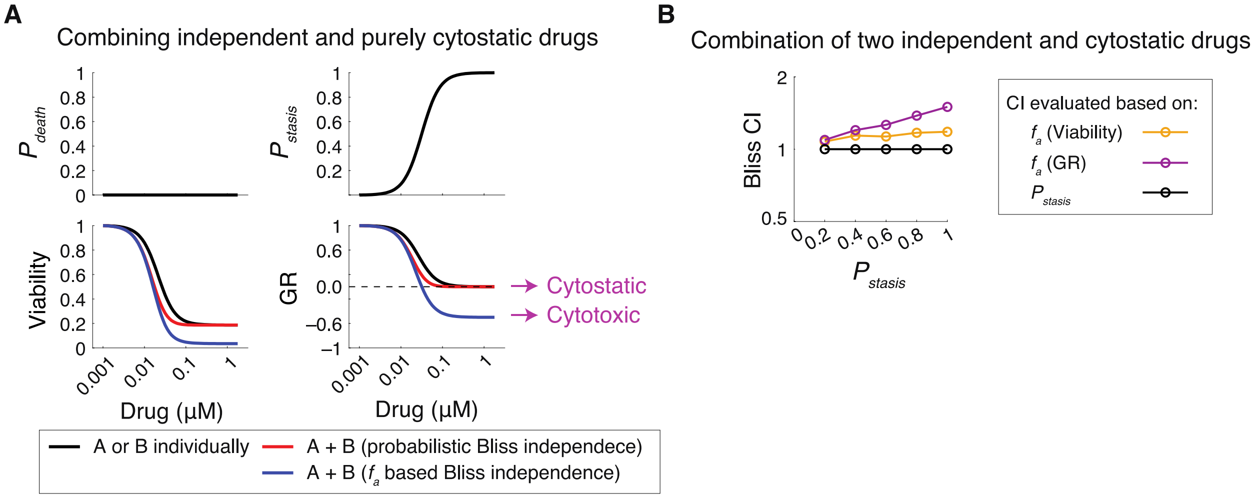

Figure 2.11 Probabilistic phenotype metrics, but not f_a-based metrics, reveal statistical independence in drug combination efficacies.

(A) Simulation results shown for the effect of two independent and purely cytostatic drugs, A and B, with identical dose-effect profiles used individually and in combination. Dose-effect profiles of drugs A and B are shown as P_{death} and P_{stasis}, quantified per unit of time (h). Normalized changes in relative viability and growth rate (GR) inhibition are reported for each condition at 48 h and the predicted combination effects are shown for scenarios where either the probabilistic metric P_{death} and P_{stasis} or f_a quantities (based on viability and GR) where used in the evaluation of Bliss independence. **(B)** Bliss combination index values calculated (at t = 48 h) using different drug response metrics, f_a (viability), f_a (GR) and P_{stasis}, in simulations of combined effects of two independent and identical drugs with variable cytostatic effects represented by variations in P_{satsis}. The rate of cell division in the absence of drug was simulated as $k_{division\ (no\ drug)} = 0.035\ h^{-1}$.

When applied to probabilistic events of drug-induced cell death, Bliss independence for the combined cytotoxic effect of drugs A and B is described as follows:

$$P^{I}_{death\ (A+B)} = k^{I}_{death\ (A+B)} dt = P_{death\ (A)} + P_{death\ (B)} - P_{death\ (A)} P_{death\ (B)}$$

$$\approx (k_{death\ (A)} + k_{death\ (B)})dt \qquad \text{(Equation 2.10)}$$

where $P_{death\ (A)}$ and $P_{death\ (B)}$ represent the probabilities with which drugs A and B induce cell death within a short time interval of dt, respectively. $P^{I}_{death\ (A+B)}$ represents the probability of death induced by the combination of drugs A and B when they act independently. $k_{death\ (A)}$, $k_{death\ (B)}$ and $k^{I}_{death\ (A+B)}$ represent rate constants associated with these probabilistic events, respectively. When applied to the conditional event of inhibition of cell division given that cells divide at a rate of $k_{division\ (no\ drug)}$ in the absence of drug, Bliss independence is described as follows:

$$P^{I}_{stasis\ (A+B)} = \frac{k^{I}_{stasis\ (A+B)}}{k_{division\ (no\ drug)}} = P_{stasis\ (A)} + P_{\ stasis(B)} - P_{stasis\ (A)} P_{stasis\ (B)}$$

(Equation 2.11)

where $P_{stasis\ (A)}$ and $P_{stasis\ (B)}$ represent the probabilities with which drugs A and B inhibit cell division given that cells would divide with a probability of $P_{division\ (no\ drug)} = k_{division\ (no\ drug)}dt$ within a short time interval of dt. $P^{I}_{stasis\ (A+B)}$ represents the cytostatic effect for the combination of drugs A and B when they act independently. $k_{stasis\ (A)}$, $k_{stasis\ (B)}$ and $k^{I}_{stasis\ (A+B)}$ represent rate constants associated with these probabilistic events. The Bliss combination index (for each of the drug-induced phenotypic effects) is thus defined as follows:

$$CI^{Bliss}_{death\ (A+B)} = \frac{P^{I}_{death\ (A+B)}}{P_{death\ (A+B)}} = \frac{k^{I}_{death\ (A+B)}}{k_{death\ (A+B)}} \qquad \text{(Equation 2.12)}$$

$$CI^{Bliss}_{stasis\ (A+B)} = \frac{P^{I}_{stasis\ (A+B)}}{P_{stasis\ (A+B)}} = \frac{k^{I}_{stasis(A+B)}}{k_{stasis\ (A+B)}} \qquad \text{(Equation 2.13)}$$

Systematic simulation results show that evaluating probabilistic independence based on drug-induced phenotypic events can distinguish a variety of possible drug interactions that would be otherwise overlooked when assessed on the basis of f_a quantities (Figure 2.12). The discrepancy is particularly substantial under conditions where drug combinations have uneven cytotoxic and cytostatic interactions, e.g., when two compounds act synergistically with respect to inhibition of division but act independently or antagonistically with respect to induction of cell death, and vice versa.

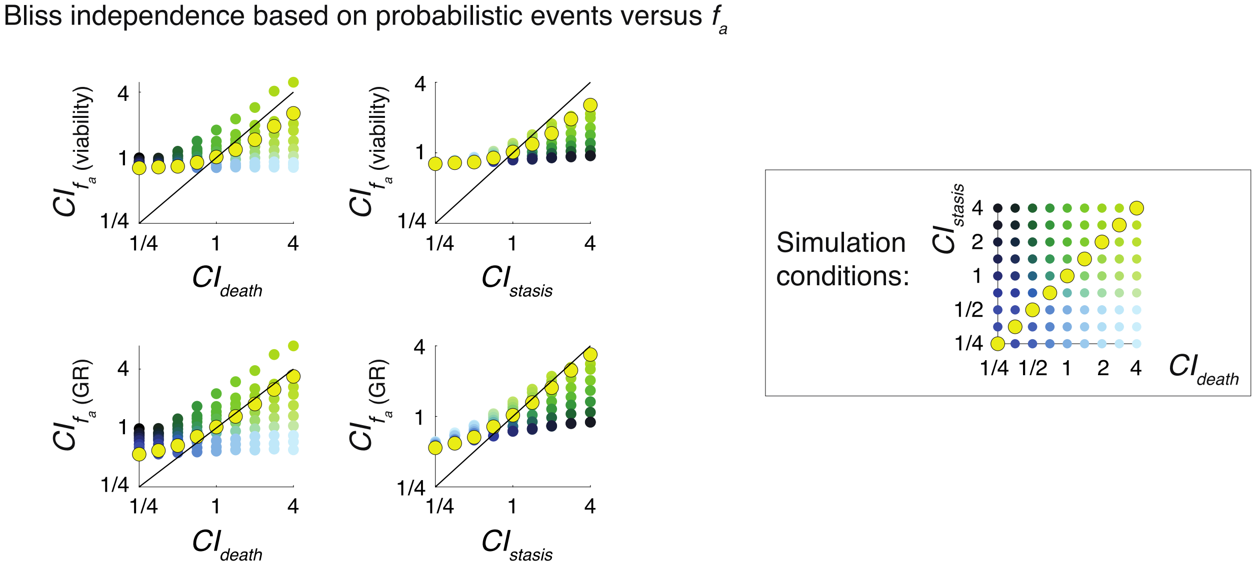

Figure 2.12 Bliss independence based on probabilistic phenotype metrics resolve the differential drug-interactions in death and stasis. Bliss independence based on f_a quantities, in contrast, can lead to biased conclusions of drug interactions.

Simulation results quantifying Bliss combination index values (at t = 48 h) calculated using f_a response metrics, f_a (viability) and f_a (GR), in comparison with probabilistic combination index values (CI_{death} and $CI_{statsis}$). Each data-point represents the mean of 10 simulations for a drug combination condition with a given set of probabilistic drug interaction condition quantified as CI_{death} and CI_{stasis}. Conditions where $CI_{death} = CI_{stasis}$ are highlighted in yellow. Representative simulations were performed using an initial live cell number of N_{live} (t = 0) = 2000, $k_{division\ (no\ drug)}$ = 0.035 h^{-1}, $k_{death\ (drug\ A)} = k_{death\ (drug\ B)}$ = 0.01 h^{-1}, $P_{stasis\ (drug\ A)} = P_{stasis\ (drug\ B)}$ = 0.2.

2.2.5 Probabilistic phenotype metrics uncover target-specific differences in drug combination efficacies

We applied the probabilistic definition of Bliss independence to evaluate time-dependent changes in the efficacies of a group of 12 compounds in sequential combination with BRAF kinase inhibitor, Vemurafenib, plus MEK kinase inhibitor, Trametinib, in two BRAF-mutated melanoma cell lines COLO858 and MMACSF over the course of five days (see Methods for details). Single-cell drug responses were monitored using time-lapse fluorescence microscopy, and changes in probabilistic rate constants k_{stasis} and k_{death} were tracked for the entire period of experiment for each drug condition individually or in combinations (Figure 2.13, Figure 2.14). The list of compounds based on their nominal targets included two HDAC inhibitors (Fimepinostat and Givinostat), two BET bromodomain inhibitors (Birabresib and I-BET762), two KDM1A inhibitors (SP2509 and ORY-1001), a pan Jmj-KDM inhibitor (JIB-04), a KDM5 inhibitor (CPI-455), two Tankyrase inhibitors (AZ6102 and NVP-TNKS656), and two CDK4/6 inhibitors (Palbociclib and Abemaciclib). These compounds were selected from two broad classes of anti-cancer drugs, referred to as epigenetic-modifying compounds and cell cycle inhibitors, which have been proposed to be used in combination with standard of care BRAF and MEK inhibitors to overcome drug-adapted subpopulations of cells in BRAF-mutant melanomas [10,21,41–49].

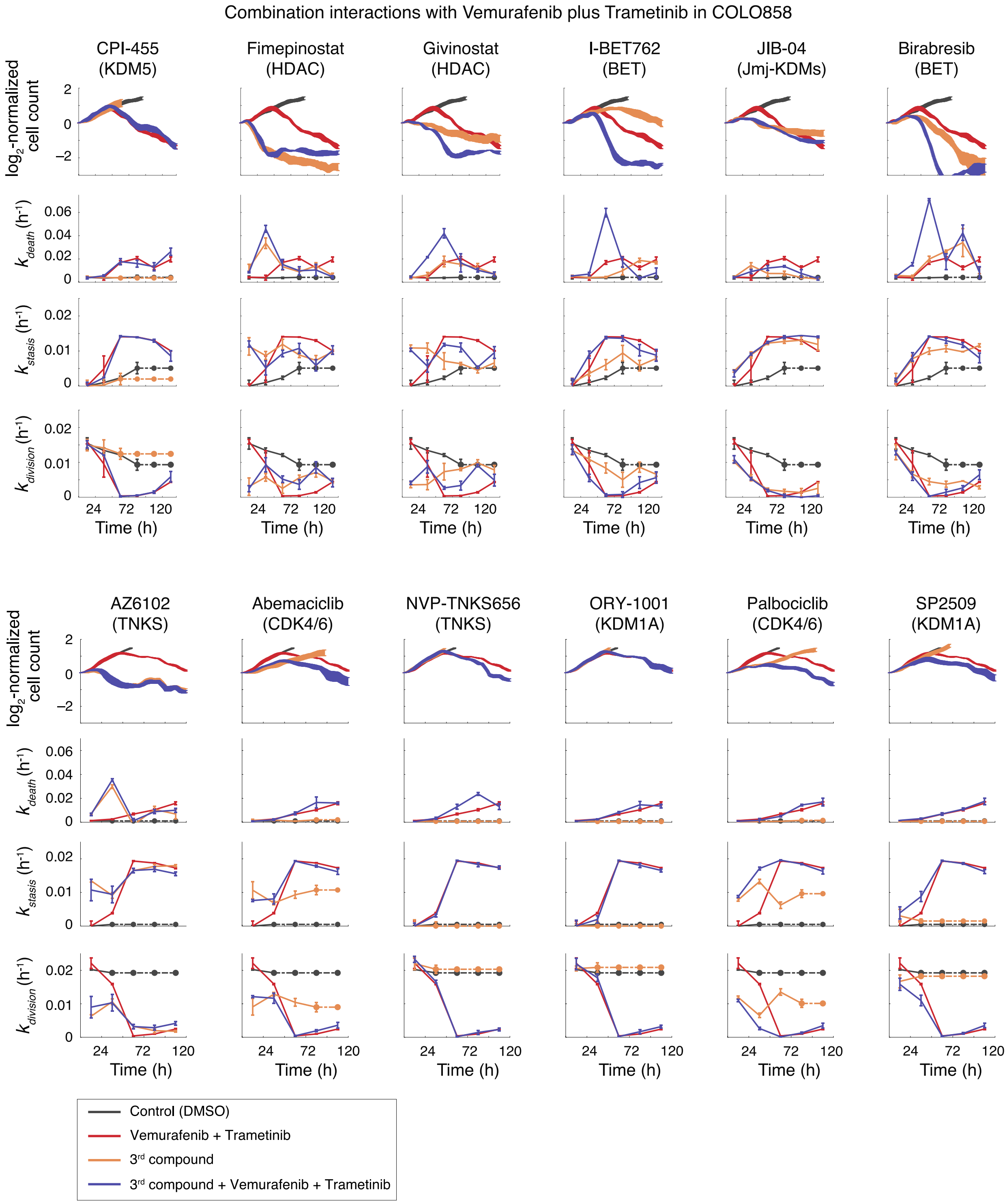

Figure 2.13 Dynamic responses of COLO858 cells to epigenetic-modifying compounds and cell cycle inhibitors in sequential combination with Vemurafenib plus Trametinib.

Estimated dynamics of changes in live cell count, k_{death}, k_{stasis} and $k_{division}$ measured from time-lapse live cell microscopy data for COLO858 cell responses to the combination of Vemurafenib (0.32 μM) and Trametinib (0.032 μM), a 3^{rd} compound (including epigenetic-modifying compounds or cell cycle inhibitors), their triple combination, or vehicle (DMSO) control. Cells were treated initially for 24 h with DMSO control or one of the epigenetic-modifying compounds or cell cycle inhibitors (3rd compound) at the following concentrations: Fimepinostat (0.02 μM), Givinostat (0.2 μM), Birabresib (0.5 μM), I-BET762 (1 μM), SP2509 (1 μM), ORY-1001 (1 μM), JIB-04 (0.2 μM), CPI-455 (5 μM), AZ6102 (1 μM), NVP-TNKS656 (1 μM), Palbociclib (1 μM), and Abemaciclib (1 μM). After 24 h, Vemurafenib at 0.3 μM plus Trametinib at 0.03 μM, or DMSO control were added to each treatment condition. $k_{division\ (no\ drug)}$ used for the estimation of k_{stasis} is estimated using cell division data averaged for the first 24 h in cells treated with DMSO only. In conditions where confluency was achieved, data-points were replaced with the last available data-point (dotted line). Data-points represent mean ± SEM across 2 or 3 replicates.

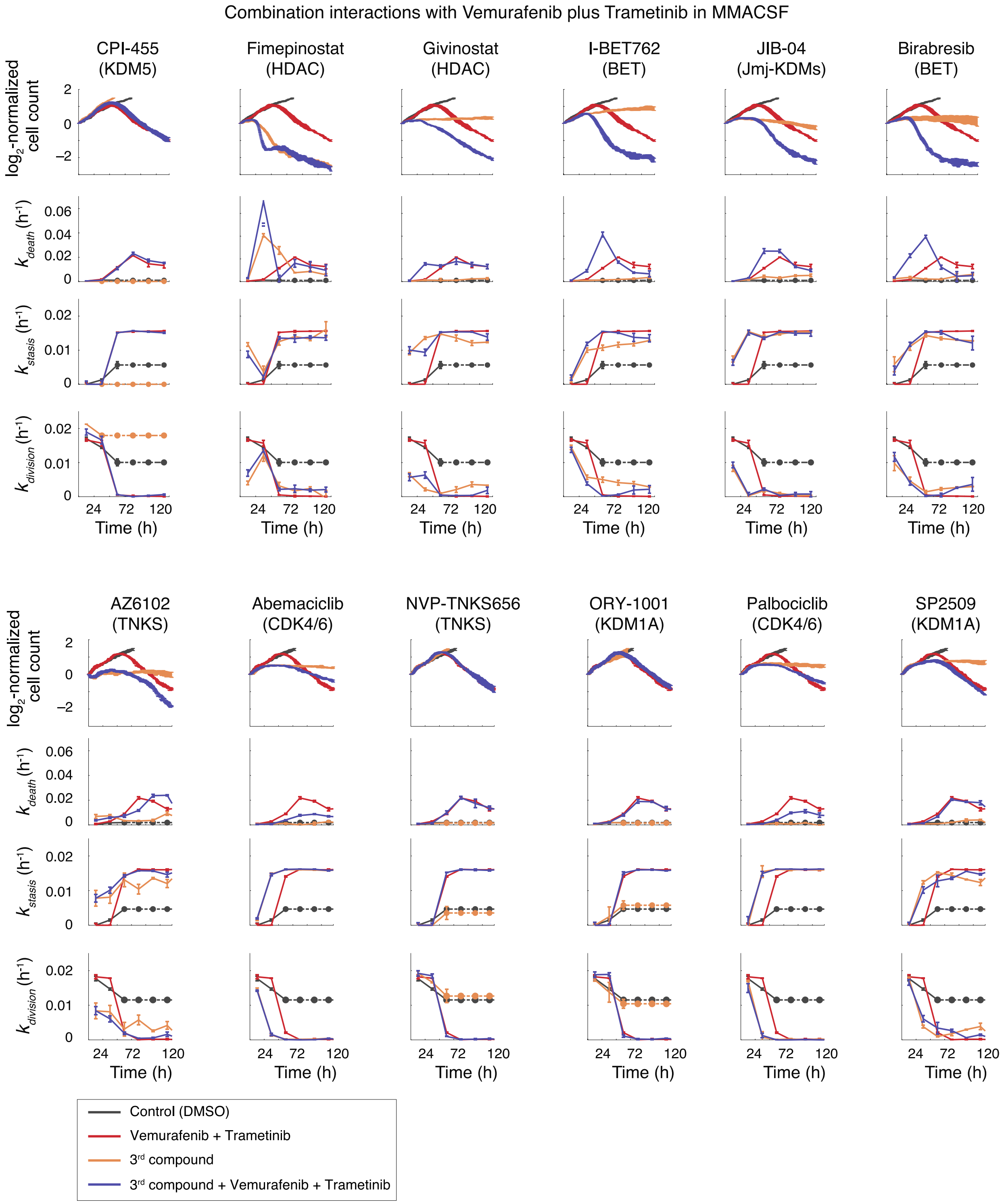

Figure 2.14 Dynamic responses of MMACSF cells to epigenetic-modifying compounds and cell cycle inhibitors in sequential combination with Vemurafenib plus Trametinib.

Estimated dynamics of changes in live cell count, k_{death}, k_{stasis} and $k_{division}$ measured from time-lapse live cell microscopy data for MMACSF cell responses to the combination of Vemurafenib (0.32 μM) and Trametinib (0.032 μM), a 3rd compound (including epigenetic-modifying compounds or cell cycle inhibitors), their triple combination, or vehicle (DMSO) control. Cells were treated initially for 24 h with DMSO control or one of the epigenetic-modifying compounds or cell cycle inhibitors (3rd compound) at the following concentrations: Fimepinostat (0.02 μM), Givinostat (0.2 μM), Birabresib (0.5 μM), I-BET762 (1 μM), SP2509 (1 μM), ORY-1001 (1 μM), JIB-04 (0.2 μM), CPI-455 (5 μM), AZ6102 (1 μM), NVP-TNKS656 (1 μM), Palbociclib (1 μM), and Abemaciclib (1 μM). After 24 h, Vemurafenib at 0.3 μM plus Trametinib at 0.03 μM, or DMSO control were added to each treatment condition. $k_{division\ (no\ drug)}$ used for the estimation of k_{stasis} is estimated using cell division data averaged for the first 24 h in cells treated with DMSO only. In conditions where confluency was achieved, data-points were replaced with the last available data-point (dotted line). Data-points represent mean ± SEM across 2 or 3 replicates.

The analysis of variations in Bliss combination index, defined based on probabilistic cytotoxic and cytostatic actions, with drug and time (followed by unsupervised clustering) led to two major conclusions (Figure 2.15A). First, effective drugs with comparable mechanisms of action (e.g. BET inhibitors, HDAC inhibitors or CDK4/6 inhibitors) exhibited similar dynamic patterns of interaction with BRAF and MEK kinase inhibitors, suggesting that differences in probabilistic drug action and interactions are target-specific. Second, cytostatic and cytotoxic drug interactions among efficacious drug combinations often varied in time and did not necessarily correlate with one another. BET inhibitors, for example, exhibited a strong synergistic cytotoxic interaction ($CI_{death} < 1$) with the combination of BRAF and MEK inhibitors within 48-72 h of treatment in both COLO858 and MMACSF cell lines, whereas their interaction was scored as independent ($CI_{stasis} \approx 1$) with respect to inhibition of cell division (Figure 2.15A, B). Furthermore, the benefit of BET inhibitors combined with Vemurafenib and Trametinib diminished following 96 h, concomitant with the emergence of a small proliferating subpopulation ($k_{division} > 0$) (Figure 2.15B). CDK4/6 inhibitors acted independently with BRAF and MEK inhibitor combination to inhibit cell division within 72-96 h in both cell lines (Figure 2.15A and Figure 2.13, Figure 2.14). Surprisingly, however, their effects on cell death appeared to be antagonistic especially in MMACSF cells (Figure 2.15C). This might be due the possibility that upon G0/G1 arrest, BRAF-mutant cells become less responsive to the effect of BRAF and

MEK inhibitors, an interesting observation which requires further investigation across more cell lines.

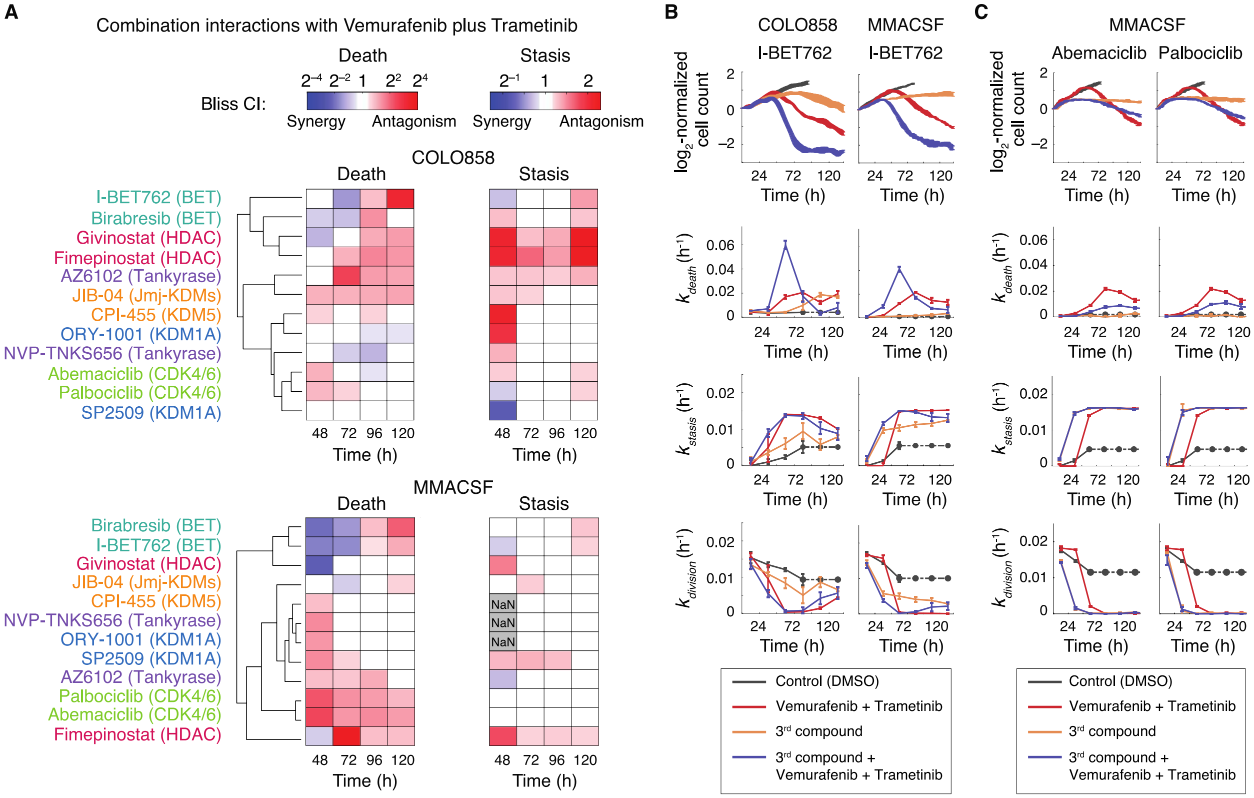

Figure 2.15 Probabilistic phenotype metrics uncover target-specific differences in drug combination efficacies and their interactions.

(A) Unsupervised clustering of Bliss combination index values (CI_{death} and CI_{stasis}) calculated using probabilistic metrics k_{death} and k_{stasis} in COLO858 and MMACSF cells between 48-120 h of exposure to various drugs in sequential combination with Vemurafenib and Trametinib. Cells were treated initially for 24 h with DMSO control or one of the epigenetic-modifying compounds or cell cycle inhibitors (3rd compound) at the following concentrations: Fimepinostat (0.02 μM), Givinostat (0.2 μM), Birabresib (0.5 μM), I-BET762 (1 μM), SP2509 (1 μM), ORY-1001 (1 μM), JIB-04 (0.2 μM), CPI-455 (5 μM), AZ6102 (1 μM), NVP-TNKS656 (1 μM), Palbociclib (1 μM), and Abemaciclib (1 μM). Nominal targets of compounds are highlighted. After 24 h, Vemurafenib at 0.3 μM plus Trametinib at 0.03 μM, or DMSO control were added to each treatment condition. Combination index data-points represent mean values across 2-3 replicates. NaN data-points represent conditions where the effect of drug combination or that of the independence model are within measurement error, making the ratio (combination index) unreliable. **(B)** Estimated dynamics of changes in live cell count, k_{death}, k_{stasis} and $k_{division}$ measured from time-lapse live cell microscopy data for COLO858 and MMACSF cell responses to the combination of Vemurafenib (0.32 μM) and Trametinib (0.032 μM), BET bromodomain inhibitor I-BET762 (1 μM), their triple combination, or vehicle (DMSO) control. **(C)** Estimated dynamics of changes in live cell count, k_{death}, k_{stasis} and $k_{division}$ measured from time-lapse live cell microscopy data for MMACSF cell responses to the combination of Vemurafenib (0.32 μM) and Trametinib (0.032 μM), CDK4/6 inhibitors Palbociclib (1 μM) and Abemaciclib (1 μM), their triple combination, or vehicle (DMSO) control. $k_{division\ (no\ drug)}$ used for the estimation of k_{stasis} for each cell line was estimated using cell division data averaged for the first 24 h in cells treated with DMSO only. In conditions where confluency was achieved (e.g. DMSO-treated cells after 60 h), data-points were replaced with the last available data-point (dotted line). Data-points represent mean ± SEM across 2 or 3 replicates.

Altogether, experimental results and simulation outcomes suggest that dynamic measurements of the phenotype metrics and probabilistic evaluation of combination index reveal distinctive responses of cells to drug combinations that might be indistinguishable when assessed based on conventional assays. Phenotype metrics deconvolve differential (and sometimes opposing) degrees of drug effect on tumor cell killing versus inhibition of cell division, a potentially important consideration in choosing appropriate drug combinations. Furthermore, the probabilistic nature of these metrics makes them sensitive to cell-to-cell heterogeneities which are typically overlooked in conventional bulk drug response assays. They are therefore appropriate choices to assess synergistic efficacy in drug combinations aimed at blocking heterogeneous subpopulations of drug-tolerant cells.

2.3 Discussion

Synergistic interactions in cancer drug efficacy are typically assessed using Bliss independence or other models (e.g. Highest Single Agent approach [2]). These models are commonly applied to drug response measurements, whose outcomes are normalized to those measured in untreated controls to identify the fraction of cells affected (f_a) by drugs. Examples of these metrics include drug-induced changes in viability (normalized live cell count) or net growth rate inhibition, which are analyzed across drug doses and combinations. Synergistic efficacy is then concluded when the observed combinatorial effect on f_a metrics exceeds the expected effect from the null model. In this paper, we use basic probability theory and computer simulations to demonstrate that using f_a metrics may bias our estimation of drug combination effectiveness and synergistic efficacy, especially when the ultimate goal is to block heterogeneous drug-tolerant subpopulations. Instead, we propose to use direct measures of time-dependent probabilities of key drug-induced phenotypic events, i.e. induction of cell death and inhibition of cell division, and their associated rate constants (k_{death} and k_{stasis}) to evaluate synergistic efficacy using probabilistic models such as Bliss.

Probabilistic phenotype metrics improve our ability to quantify drug efficacy and characterize drug combination interactions in the following three ways. First, in contrast to the commonly used f_a metrics, phenotype metrics are directly related to the probabilities of drug action in a cell population within any given time interval following drug exposure. Furthermore, they deconvolve differential degrees of drug effect on tumor cell killing versus inhibition of cell division, which may not be correlated in many cases. Second, k_{death} and k_{stasis} dramatically increase the sensitivity of short-term drug response assays to dynamic cell-to-cell heterogeneities and the presence (or emergence) of drug-resistant sub-clones, which are typically overlooked in conventional f_a based drug response analyses. This is a critical issue especially when heterogeneous tumor cell populations consist of cells that are differentially sensitive to drugs and that their sensitivity changes with time. Third, the probabilistic nature of phenotype metrics allows us to use them directly in unbiased evaluation of independence, synergistic or antagonistic efficacy in drug combinations using probabilistic models such as Bliss independence.

While we focused on Bliss independence as a probabilistic framework to study synergistic efficacy, phenotype metrics and their dose- and time-dependent variations could be used in other platforms for broad evaluation of synergy. A recently developed multi-dimensional framework (MuSyC) uses a two-dimensional extension of Hill equation to distinguish synergistic efficacy versus synergistic potency, thereby allowing for a comprehensive understanding of drug interactions. Such understanding not only helps with improving therapeutic efficacy via enhancing effect, but also reducing off-target toxicities via dose reduction [10]. Probabilistic phenotype rate constants follow dose-response patterns suitable to be fit by Hill equation and therefore can be used as input to platforms such as MuSyC.

Estimating probabilistic phenotype metrics requires continuous time-lapse experiments along periods of multiple days, followed by computational single-cell analysis. In this study, we used cell lines engineered to express fluorescent reporters to capture drug-induced changes in cellular death and division events. Such integrative methods may not be necessary for large-scale drug screening projects, in which many drugs are filtered out because of lack of potency. The benefit of these methods is significant, however, when there is a need for identifying more efficacious drugs or drug combinations among a selection of reasonably potent candidates. It has become increasingly evident that cell-to-cell variability is the cause of partial efficacy and incomplete responsiveness of tumor cell populations to a variety of highly potent cytotoxic and targeted therapies. Such heterogeneities are not captured using conventional population-based assays, but may originate residual cells from which drug-resistant clones can arise. Therefore, the probabilistic analysis of single-cell phenotypes has a great potential to improve our understanding of heterogeneity in drug response and facilitate the discovery of more efficacious combination therapies. We envision that the ongoing experimental and computational advances in single-cell tracking (including dye-based or label-free cell fate tracking and lineage construction by using machine learning and deep learning algorithms) will rapidly improve the efficiency, accuracy, and applicability of single-cell approaches to the analysis of cancer drug response.

2.4 Materials and Methods

2.4.1 Cell culture

BRAF-mutated melanoma cell lines used in this study were obtained from the Massachusetts General Hospital Cancer Center with the following primary sources: COLO858 (ECACC) and MMACSF (Riken Bioresource Center). Each cell line was independently authenticated by Short Tandem Repeats (STR) profiling by ATCC. COLO858 cells were grown in RMPI 1640 (Corning cellgro, Cat. 10-040 CV), and MMACSF cells were grown in DMEM/F-12 (Thermo Fisher Scientific, Cat. 11330-032). For both cell lines, growth media were supplemented with 5% fetal bovine serum (Thermo Fisher Scientific, Cat. 26140-079) and 1% sodium pyruvate (Thermo Fisher Scientific, Cat. 11360-070). We added penicillin and streptomycin at 100 U/ml (Thermo Fisher Scientific, Cat. 15140-122) and plasmocin at 0.5 μg/ml (InvivoGen, Cat. ant-mpp) to all growth media. Cells were engineered to stably express H2B-Venus and mCherry-Geminin fluorescent reporters as described previously [21]. Engineered and parental cell lines were confirmed to grow at comparable rates in the absence of any treatment or in the presence of different concentrations of BRAF inhibitor Vemurafenib over 72 hours of treatment.

2.4.2 Reagents

Chemical inhibitors used in this study were obtained from Selleck Chemicals with the following catalog numbers: Vemurafenib (Cat. S1267), Trametinib (Cat. S2673), SP2509 (Cat. S7680), ORY-1001 (Cat. S7795), Palbociclib (Cat. S1116), Abemaciclib (Cat. S7158), AZ6102 (Cat. S7767), NVP-TNKS656 (Cat. S7238), Givinostat (Cat. S2170), Fimepinostat (CUDC-907; Cat. S2759), JIB-04 (Cat. S7281), CPI-455 (Cat. S8287), I-BET762 (Cat. S7189) and Birabresib (OTX-015; Cat. S7360). All chemical inhibitors were dissolved in dimethyl sulfoxide (DMSO) as 10 mM stock solution, except Palbociclib of which the stock concentration was 5 mM.

2.4.3 Cell seeding and drug treatment

COLO858 and MMACSF cells expressing fluorescent reporters were seeded into Costar 96-well black clear-bottom tissue culture plates (Corning 2603) in 220 μL full growth medium without phenol red at a density of 2000 and 3000 cells/well, respectively. Cells were counted using a TC20™ Automated Cell Counter (Bio Rad). In the case of Vemurafenib dose-response experiments, cells were treated ~24 h after seeding with either DMSO or five different concentrations of Vemurafenib (0.0316, 0.1, 0.316, 1 and 3.16 μM) for a period of ~5 days. In the case of drug combination experiments, cells were treated (also 24 h after seeding) with DMSO control or one of the epigenetic-modifying compounds or cell cycle inhibitors at the following concentrations: Fimepinostat (0.02 μM), Givinostat (0.2 μM), Birabresib (0.5 μM), I-BET762 (1 μM), SP2509 (1 μM), ORY-1001 (1 μM), JIB-04 (0.2 μM), CPI-455 (5 μM), AZ6102 (1 μM), NVP-TNKS656 (1 μM), Palbociclib (1 μM), and Abemaciclib (1 μM); drug concentrations were chosen based on previous reports exhibiting maximal target inhibition in cells. After 24 h, Vemurafenib at 0.3 μM plus Trametinib at 0.03 μM, or DMSO control were added to each treatment condition. All drug treatments were performed in at least 4 replicates using a Hewlett-Packard (HP) D300 Digital Dispenser.

2.4.4 High-throughput time-lapse live cell microscopy

Within 50-60 min after each treatment, cells were imaged every 10 min (for COLO858) and every 15 min (for MMACSF) using a Nikon Ti2-E inverted microscope with motorized stage, Perfect Focus System, 20× objective, and a Photometrics Prime 95B camera followed by 2×2 binning. The process of image acquisition was controlled using NIS element software. Illumination was powered by the Lumencor Spectra X light engine. H2B-Venus fluorescence was captured using 510 nm excitation and 535 nm emission at 25 ms exposure for MMACSF cells and 20 ms exposure for COLO858 cells. mCherry-Geminin fluorescence was captured using 575 nm excitation and a 629.5 nm emission at 80 ms exposure for MMACSF cells and 100 ms exposure for COLO858 cells. Throughout the entire period of image acquisition, environmental conditions were maintained at 37°C, 5% CO_2, and 93% humidity using an OkoLab Enclosure.

2.4.5 Image analysis and automated cell tracking workflow

Images were first processed using Fiji [50] for rolling ball background subtraction with radius of 20 pixels. Background-subtracted images were then analyzed using CellProfiler (3.1.8) for segmentation and classification of cellular phenotypic states, including cells that express high and low levels of Geminin (referred to as $\text{Geminin}^{\text{high}}$ and $\text{Geminin}^{\text{low}}$ cells, respectively), or live versus dead cells. Briefly, CellProfiler analysis (Figure 2.7) involved: (1) edge enhancement and dark hole feature enhancement of the background-subtracted H2B images to facilitate segmentation; (2) segmenting individual cell nuclei using the Otsu thresholding method; (3) using nuclei segmentations as masks to measure object intensities for all channels as well as object sizes and shapes; (4) classification of phenotypic states of each cell object using the classification model output from CellProfiler Analyst (2.2.1) [51] based on features measured from the previous step. $\text{Geminin}^{\text{high}}$ versus $\text{Geminin}^{\text{low}}$ cell classifiers and live versus dead cell classifiers were trained separately using fast gentle boosting algorithm in CellProfiler Analyst with eight and fifteen maximum rules, respectively. The training set used to develop each phenotype classifier was an annotated set, generated via manually sorting the cell object tiles into their corresponding phenotype classes in CellProfiler Analyst. The process of manual sorting followed by model training was iterated until approximately 80% of true positive accuracy was achieved.

Based on phenotype classifications of individual cells for each image output from CellProfiler, corresponding synthetic images were generated in MATLAB (2018b) for each phenotype of interest. Synthetic images contained synthetic pixels at locations of cells. They were used to mark each of the phenotypes of interest (i.e. Geminin^{high} or dead cells) in each image, which were then tracked across series of timepoints using the Fiji plugin TrackMate (3.8.0), without additional need to perform image segmentation. In other words, we combined the power of CellProfiler analysis for accurate and high-throughput image segmentation with the ability of TrackMate to track individual cell phenotypes in a multi-day time-lapse experiment. To achieve this goal, synthetic images for Geminin^{high} cells, dead cells, background-subtracted H2B and Geminin images acquired from the same site were merged into a single multi-channel image composite using Fiji. Image composites were then analyzed using TrackMate with TrackMate extras and Track Analysis extensions [52] for automated tracking. Synthetic pixels of a selected channel were detected by the Laplacian of Gaussian detector and spots were linked with Linear Assignment Problem (LAP) Tracker. Additional spots filtering (based on intensities from multiple channels) and track filtering (based on track duration, track median velocity, and velocity standard deviation) were implemented to optimize tracking results.

2.4.6 Estimating probabilistic phenotype rate constants from individual cell tracking data

Single-cell tracking data generated using TrackMate was analyzed using MATLAB. Transition of a live cell from Geminin^{high} to Geminin^{low} was recorded as a division event, whereas the beginning of a dead cell track was recorded as a death event (Figure 2.7). To estimate time-dependent changes in probabilistic phenotype rate constants, k_{death} and $k_{division}$, the number of recorded cell death and division events (N_{death} and $N_{division}$) were quantified over a series of uniformly distributed time intervals ($t \rightarrow t + \Delta t$), where Δt = 12 h or 24 h. Normalizing

N_{death} and $N_{division}$ to the length of each time interval (Δt) and the average number of live cells within the same interval $[N_{live}(t \rightarrow t + \Delta t)]_{avg}$, phenotype rate constant were estimated using Equations 2.5-2.7. As expected, we observed that the magnitude of noise in single-cell tracking data and consequently the relative error in the estimation of $k_{division}$ and k_{death}, increased under conditions where Geminin^{high} and dead cells were highly concentrated, respectively. To mitigate the effect of noise under such conditions, we imposed the following constraints in our estimation of $N_{division}$ (when $N_{death} < N_{division}$) and N_{death} (when $N_{death} > N_{division}$) during each time interval, respectively:

$$N_{division}(t \rightarrow t + \Delta t) = \big(N_{live}(t + \Delta t) - N_{live}(t)\big) - N_{death}(t \rightarrow t + \Delta t)$$

(Equation 2.14)

$$N_{death}(t \rightarrow t + \Delta t) = N_{division}(t \rightarrow t + \Delta t) - (N_{live}(t + \Delta t) - N_{live}(t))$$

(Equation 2.15)

These constraints are consistent with the assumption that the overall change in the number of live cells during each time interval (Δt) must be equal to the number of division events minus the number of death events during the same time interval.

2.4.7 Verifying the accuracy of automated cell tracking workflow using manual single-cell tracking

To test the performance of our automated image analysis workflow, we compared the phenotype rate constants measured using data from the automated pipeline with those measured using data generated from manual single-cell tracking. This was accomplished using a MATLAB-based software, allowing accurate single-cell tracking and cell fate annotation of individual cells across time-lapse images taken over a period of multiple days [40]. Briefly, the manual tracking method relies on identification of individual cells using intensity and shape information of the nuclear marker (H2B-Venus), track propagation using nearest neighbor criteria, and real-time user correction of tracking, and annotation of cell death and division events based on H2B and Geminin signal intensities. For each condition, about 150-250 cells pooled from four replicates were manually tracked and cell death and division events were recorded. Phenotype rate constants were then calculated using Equations 2.5-2.7.

2.4.8 Estimating fraction of cells affected (f_a) by drug

Currently, evaluation of Bliss independence (and other drug interaction frameworks) is based on fraction of cells affected (f_a), a normalized parameter between zero and one, that represents the fractional effect of drugs individually or in combination [53]. Conventionally, relative viability (or cell count normalized to an untreated control) measured at a fixed time-point (typically 72 or 96 h) following drug treatment has been used to calculate f_a:

$$f_a(viability) = 1 - viability \qquad \text{(Equation 2.16)}$$

Despite its wide-spread usage, however, the relative viability approach in assessing drug response suffers from a fundamental flaw, which is being confounded by variation in cell proliferation rates and assay duration. The reason is that cell count, which is used as a normalization factor in this approach, is non-linearly time-dependent. Therefore, new generation drug response metrics have recently been introduced to correct for this bias [5,6]. The nature of these metrics is based on modeling drug-induced changes in the net growth rate of the cancer cell population (instead of relative viability) as a function of drug dose. These metrics include drug-induced proliferation (DIP) rate [6] and growth rate (GR) inhibition [5], both of which consider and correct for the variability in growth rate that is irrelevant to drug treatment via normalizing the net growth rate of the drug-treated cell population to that of the untreated control. DIP rate and GR inhibition are defined as follows:

$$DIP = \frac{k_{\text{net growth (with drug)}}}{k_{\text{net growth (no drug)}}} \qquad \text{(Equation 2.17)}$$

$$GR = 2^{\frac{k_{\text{net growth (with drug)}}}{k_{\text{net growth (no drug)}}}} - 1 \qquad \text{(Equation 2.18)}$$

where $k_{\text{net growth (with drug)}}$ and $k_{\text{net growth (no drug)}}$ are the net population growth rates measured in the drug-treated cell population and the untreated control at a particular time-point, respectively.

Given the dynamic range of each metric, the definition of fraction of cells affected (f_a) for these new metrics, f_a(DIP) and f_a(GR), is modified as follows so that $0 \leq f_a \leq 1$:

$$f_a(DIP) = \frac{1 - DIP}{1\text{-}min(DIP)} \qquad \text{(Equation 2.19)}$$

$$f_a(GR) = \frac{1 - GR}{2} \qquad \text{(Equation 2.20)}$$

2.4.9 Stochastic simulation of cytotoxic and cytostatic drug effects

We modeled phenotypic events in a heterogeneous tumor cell population as a series of independent stochastic reaction processes at a single-cell level. Drug-induced death events were described by the following reaction:

$$cell \xrightarrow{k_{death}} dead\ cell$$

where the rate constant of death k_{death} is defined such that a given cell dies with a probability of $k_{death}dt$ within a reasonably short time interval (dt). Cell division in the absence of drug may be described by the following reaction:

$$cell \xrightarrow{k_{\text{division (no drug)}}} 2\ cells$$

where $k_{\text{division (no drug)}}$ is the inherent rate of division of a given cell. The cytostatic effect of a drug on a cell was described by a conditional probability ($P_{stasis} = P_{\text{inhibition of division (with drug) | division (no drug)}}$) with which it prevents a cell from dividing given that it would have divided in the absence of drug with a probability of $P_{\text{division (no drug)}}$. Drugs that do not inhibit cell division and those that accelerate cell division are both characterized by $P_{stasis} = 0$. To satisfy this assumption, we consider an upper-bound limit for the probability of cell division that is equal to $P_{division\ (no\ drug)}$. For cancer drugs that have inhibitory effect on cell division, the relationship between P_{stasis} and $P_{division\ (with\ drug)}$ may be derived as follows:

$$P_{division\ (no\ drug)}$$

$$= P_{division\ (no\ drug)\ \cap\ division\ (with\ drug)} + P_{division\ (no\ drug)\ \cap\ inhibition\ of\ division\ (with\ drug)}$$

(Equation 2.21)

$$= P_{division\ (with\ drug)} + P_{inhibition\ of\ division\ (with\ drug)\ |\ division\ (no\ drug)} \cdot P_{division\ (no\ drug)}$$

(Equation 2.22)

$$P_{inhibition\ of\ division\ (with\ drug)\ |\ division\ (no\ drug)} = \frac{P_{division\ (no\ drug)} - P_{division\ (with\ drug)}}{P_{division\ (no\ drug)}}$$

(Equation 2.23)

$$P_{stasis} = 1 - \frac{P_{division\ (with\ drug)}}{P_{division\ (no\ drug)}}$$ (Equation 2.24)

$$P_{division\ (with\ drug)} = (1 - P_{stasis})P_{division\ (no\ drug)}$$ (Equation 2.25)

In the presence of drug, cell division and inhibition of cell division (stasis) may be described by the following reactions, respectively:

$$cell \xrightarrow{k_{division}} 2cells$$

$$cell \xrightarrow{k_{stasis}} cell$$

where the rate constants are as follow:

$$k_{stasis} = P_{stasis} k_{division\ (no\ drug)}$$ (Equation 2.26)

$$k_{division} = (1 - P_{stasis}) k_{division\ (no\ drug)}$$ (Equation 2.27)

The model assumes that the processes of drug-induced cell death and inhibition of cell division are independent of each other.

At the population level, *Poisson* processes of drug-induced phenotypic events in a tumor cell population were simulated using the Gillespie algorithm. Briefly, the Gillespie algorithm determines the time to the next reaction event in the cell population based on an exponential distribution that statistically characterizes the *Poisson* processes. The algorithm then stochastically determines whether the event is death or division based on probabilities that are proportional to the rates of these two processes (k_{death} and $k_{division}$). If the chosen event is division, then with probability P_{stasis} that division event is rejected.

2.4.10 Validation of non-stationary Poisson models for live cell microscopy data

The probabilistic modeling approach used in this study involves a commonly used formulation of stochastic chemical kinetics, describing the time evolution of a reacting system while taking into consideration the fact that individual reaction events (typically between individual molecules) are random point *Poisson* processes [54]. While using a similar formulation, we consider a single-cell event (death or division) as an individual event, rather than modeling any of the drug-induced molecular events that underlie such cellular processes. Previous work (based on live-cell measurement and modeling) has shown that apoptosis, for example, is controlled by a snap action switch at a single-cell level [55]. This switch, however, is associated with a delay that is variable from one cell to another within a population, preventing cells from dying en masse following exposure to a death stimulus. Such variability makes it possible for an all-or-none response at a single-cell level to be graded at the population level such that the concentration of stimulus (or drug) controls the probability with which a cell responds during a specific period of time. This is in general agreement with the definition of *Poisson* process to model the population behavior, where the rate of a cellular event is directly linked to the *Poisson* rate parameter. Such parameter is expected to be controlled by the concentration of a key set of molecular regulators that are not explicitly modeled. However, changes in cellular state (due to drug adaptation, for example) may influence the concentration of these regulators, causing time-dependent changes in the *Poisson* rate constant, making non-stationary *Poisson* process a potentially suitable framework to model such dynamic, adaptive responses.

To experimentally test whether a simplified model of non-stationary *Poisson* process may explain the distribution of drug-induced death and division events in time-lapse microscopy data, we used maximum likelihood estimation to fit two non-stationary *Poisson* models, one to the single-cell death data and one to the single-cell division data. The rate function $k(t)$ of the non-stationary *Poisson* models used for data fitting was assumed to be a piece-wise function in time, where for each 12 h interval the rate was given by a single parameter. Hence, to capture 120 h of data, we set the rate function for each *Poisson* process with 10 parameters. The log-likelihood function for fitting a non-stationary *Poisson* model is given as follows:

$$\ell(\vartheta)=\sum_{j=1}^{n} log\{k(t_j;\vartheta)\} - \int_0^T k(\tau;\vartheta)d\tau \qquad \text{(Equation 2.28)}$$

where θ is a vector of the 10 parameters to be estimated from the data, n is the number of datapoints, t_i is the time of the i^{th} event and T is the end time of the experiment. The log-likelihood function was then maximized using the constrained optimization function ‘fmincon()’ in MATLAB. Using the fit parameters, we then simulated drug responses for 30 times and the normalized mean counts of phenotypic events were compared to that of the same data used for parameter estimation.

2.4.11 Simulations of combined drug responses with variable modes of drug interaction

For combined drug response simulations, we modified the Gillespie algorithm as follows. After determining the time of the next event, the algorithm stochastically determines whether that event is a death event induced by drug A, a death event induced by drug B, or a division event based on probabilities proportional to their rates of occurrence. In cases where the two drugs confer statistically independent cell killing, the probabilities of the next event being drug A-induced death and drug B-induced death are respectively proportional to their single drug-induced rates of death, i.e. $k_{death(A)}$ and $k_{death(B)}$, whereas the probability of the next event being a division event is proportional to the inherent division rate of the cell, $k_{division\ (no\ drug)}$. If the next event is division, then with a probability of $P_{stasis(A+B)}$ that division event is rejected. For independent cytostatic interactions, $P_{stasis(A+B)}$ is set to $P^{I}_{stasis(A+B)}$ as defined in Equation 2.11. In cases where drug combinations are not independent, $P_{stasis(A+B)}$ and $P_{death(A+B)}$ will be calculated as $P^{I}_{stasis(A+B)}$ and $P^{I}_{death(A+B)}$ divided by CI_{death} and CI_{stasis} to simulate different modes of drug interaction, respectively. For the purpose of comparison, we also evaluated Bliss combination index while replacing probabilistic metrics with f_a quantities measured for each drug condition individually and in combination.

2.4.12 Simulations of heterogeneous drug response in the presence of drug-tolerant subpopulations

We simulated drug treatment scenarios where the initial cell population consisted of heterogeneous subpopulations, in which a small fraction of cells was substantially less sensitive to treatment relative to the majority of the cell population. Stochastic arrival of death and inhibition of division events were modeled using Gillespie algorithm as described above, while considering two subpopulations: a larger sensitive (S) subpopulation and a small drug-tolerant or resistant (R) subpopulation. We initialized simulations with 300 cells, a small fraction of which

(ω, varied from 0%-5%) had a more resistant phenotype, i.e. a lower death rate constant and a higher probability of stasis than that of the sensitive population, in the presence of drug. We modeled such resistant phenotype by defining the level of resistance ($r \geq 1$, varied from 1-16) as the fold-change in the rates of death and probability of stasis relative to the sensitive population. We used same fold-changes for death and cytostasis rates. We assumed a fixed inherent growth rate for the sensitive population $k^{S}_{division\ (no\ drug)} = 0.035\ h^{-1}$, while considering three different possible inherent growth rates for the resistant population $k^{R}_{division\ (no\ drug)} = 0.035\ h^{-1}$, $0.02\ h^{-1}$, and $0.009\ h^{-1}$. Drug response parameters for the drug-sensitive population include: $k^{S}_{death\ (drug)} = 0.03\ h^{-1}$, $P^{S}_{stasis\ (drug)} = 0.8$. Drug response parameters for the drug-tolerant subpopulation are: $k^{R}_{death\ (drug)} = k^{S}_{death\ (drug)} / r$, $P^{R}_{stasis\ (drug)} = P^{S}_{stasis\ (drug)} / r$. We assumed that phenotypic responses of both subpopulations are independent of each other and that daughter cells within the same subpopulation inherit the exact same probabilities of phenotypic events as their mother cells. The responses (i.e. number of live cells, death and division events) of the two subpopulations were summed together to show the overall response of the entire cell population. To compare quantitatively the sensitivity of different metrics in capturing the differences in drug effect in the presence of phenotypic heterogeneity, we systematically varied the initial fraction of drug-tolerant subpopulation (ω) and its level of resistance (r) as input parameters in simulations. For each simulation, overall drug effect using different metrics (fraction affected or phenotype rate constants) were calculated. To evaluate the sensitivity of each metric to the presence of drug-tolerant subpopulations, we defined and calculated “resistance enrichment ratio” as the ratio of these metrics between two treatment scenarios, one in the presence of a heterogeneous population (varying $\omega > 0$ and $r > 1$) and one in the absence of heterogeneity ($\omega = 0$ or $r = 1$).

The smaller the resistance enrichment ratio becomes, the more significant decrease in drug effect is captured by a given metric in the presence of drug-tolerant cells.

2.4.13 Hierarchical clustering

Unsupervised hierarchical clustering of combination index (*CI*) values estimated from the application of Bliss independence to probabilistic phenotype rate constants measured for 24 h time intervals of drug treatments was carried out using MATLAB 2018b with the Euclidean distance metric and the Complete (farthest distance) algorithm for computing the distance between clusters.

2.4.14 Sensitivity analysis

To compare the sensitivity of different metrics (with different units), to the variation of parameter P_{death}, we defined fractional sensitivity (S_f) as follows:

$$S_f(f_a, P_{death}) = \frac{\partial f_a / f_a}{\partial P_{death} / P_{death}} \qquad \text{(Equation 2.29)}$$

$$S_f(k_{death}, P_{death}) = \frac{\partial k_{death} / k_{death}}{\partial P_{death} / P_{death}} \qquad \text{(Equation 2.30)}$$

S_f values of less than 1 represent reduced sensitivity of the metric to changes in P_{death}.

2.4.15 Statistical analysis

All data with error bars were presented as mean ± standard error of the mean (SEM) using indicated numbers of replicates.

2.4.16 Data availability

Source data extracted from the analysis of time-lapse imaging in melanoma cells (presented in Figure 2.8, Figure 2.13 and Figure 2.14) are included in Supplementary Tables S1-S4 on the publication website (https://dx.plos.org/10.1371/journal.pcbi.1007688).

2.4.17 Code availability

Custom MATLAB scripts for probabilistic simulation of drug response in heterogeneous tumors cell populations (presented in Figure 2.3, Figure 2.5 and Figure 2.12) are available on GitHub at the following address: https://github.com/fallahi-sichani-lab/probabilisticDrugResponse

2.5 Acknowledgments

We thank Dr. Mehwish Khaliq and Dr. Mohan Manikkam for their assistance with the experiments, and Divya Venkat for performing single-cell manual tracking. We thank members of the Fallahi-Sichani laboratory and Wendy Thomas for help and discussion. This work was supported by awards from the Elsa Pardee Foundation and V Foundation for Cancer Research V2017-011, Department of Defense PRCRP Career Development Award W81XWH1810427, NIH grants R00-CA194163 and R35-GM133404 (to MFS), P30-CA046592 (University of Michigan Rogel Cancer Center), Rackham International Student Fellowship (to NCL), and NCI Training Grant award T32-CA009676 (to MK).

References

1. Greco WR, Bravo G, Parsons JC. The search for synergy: a critical review from a response surface perspective. Pharmacol Rev. 1995;47: 331–385.

2. Berenbaum MC. What is synergy? Pharmacol Rev. 1989;41: 93–141.

3. Foucquier J, Guedj M. Analysis of drug combinations: current methodological landscape. Pharmacol Res Perspect. 2015;3. doi:10.1002/prp2.149

4. Geary N. Understanding synergy. Am J Physiol Endocrinol Metab. 2013;304: E237-253. doi:10.1152/ajpendo.00308.2012

5. Hafner M, Niepel M, Chung M, Sorger PK. Growth rate inhibition metrics correct for confounders in measuring sensitivity to cancer drugs. Nat Methods. 2016;13: 521–527. doi:10.1038/nmeth.3853

6. Harris LA, Frick PL, Garbett SP, Hardeman KN, Paudel BB, Lopez CF, et al. An unbiased metric of antiproliferative drug effect in vitro. Nat Methods. 2016;13: 497–500. doi:10.1038/nmeth.3852

7. Margue C, Philippidou D, Kozar I, Cesi G, Felten P, Kulms D, et al. Kinase inhibitor library screening identifies synergistic drug combinations effective in sensitive and resistant melanoma cells. J Exp Clin Cancer Res. 2019;38. doi:10.1186/s13046-019-1038-x

8. Crystal AS, Shaw AT, Sequist LV, Friboulet L, Niederst MJ, Lockerman EL, et al. Patient-derived models of acquired resistance can identify effective drug combinations for cancer. Science. 2014;346: 1480–1486. doi:10.1126/science.1254721

9. de Lange J, Ly LV, Lodder K, Verlaan-de Vries M, Teunisse AF a. S, Jager MJ, et al. Synergistic growth inhibition based on small-molecule p53 activation as treatment for intraocular melanoma. Oncogene. 2012;31: 1105–1116. doi:10.1038/onc.2011.309

10. Meyer CT, Wooten DJ, Paudel BB, Bauer J, Hardeman KN, Westover D, et al. Quantifying Drug Combination Synergy along Potency and Efficacy Axes. Cell Syst. 2019;8: 97-108.e16. doi:10.1016/j.cels.2019.01.003

11. Yadav B, Wennerberg K, Aittokallio T, Tang J. Searching for Drug Synergy in Complex Dose–Response Landscapes Using an Interaction Potency Model. Comput Struct Biotechnol J. 2015;13: 504–513. doi:10.1016/j.csbj.2015.09.001

12. Bliss CI. The calculation of microbial assays. Bacteriol Rev. 1956;20: 243–258.

13. Chou TC, Talalay P. Quantitative analysis of dose-effect relationships: the combined effects of multiple drugs or enzyme inhibitors. Adv Enzyme Regul. 1984;22: 27–55.

14. Loewe S, Muischnek H. Effect of combinations: Mathematical basis of problem. Arch Exp Pathol Pharmacol. 1926;114: 313–326.

15. Gaddum JH. Pharmacology. 1st ed. Oxford University Press; 1940.

16. Bliss CI. The toxicity of poisons applied jointly. Ann Appl Biol. 1939;26: 585–615. doi:10.1111/j.1744-7348.1939.tb06990.x

17. Fallahi-Sichani M, Honarnejad S, Heiser LM, Gray JW, Sorger PK. Metrics other than potency reveal systematic variation in responses to cancer drugs. Nat Chem Biol. 2013;9: 708–714. doi:10.1038/nchembio.1337

18. Yang R, Niepel M, Mitchison TK, Sorger PK. Dissecting variability in responses to cancer chemotherapy through systems pharmacology. Clin Pharmacol Ther. 2010;88: 34–38. doi:10.1038/clpt.2010.96

19. Azad NS, Posadas EM, Kwitkowski VE, Steinberg SM, Jain L, Annunziata CM, et al. Combination Targeted Therapy With Sorafenib and Bevacizumab Results in Enhanced Toxicity and Antitumor Activity. J Clin Oncol. 2008;26: 3709–3714. doi:10.1200/JCO.2007.10.8332

20. Sosman JA, Flaherty KT, Atkins MB, McDermott DF, Rothenberg ML, Vermeulen WL, et al. Updated results of phase I trial of sorafenib (S) and bevacizumab (B) in patients with metastatic renal cell cancer (mRCC). J Clin Oncol. 2008;26: 5011–5011. doi:10.1200/jco.2008.26.15_suppl.5011

21. Fallahi-Sichani M, Becker V, Izar B, Baker GJ, Lin J-R, Boswell SA, et al. Adaptive resistance of melanoma cells to RAF inhibition via reversible induction of a slowly dividing de-differentiated state. Mol Syst Biol. 2017;13: 905. doi:10.15252/msb.20166796

22. Fallahi-Sichani M, Moerke NJ, Niepel M, Zhang T, Gray NS, Sorger PK. Systematic analysis of BRAF(V600E) melanomas reveals a role for JNK/c-Jun pathway in adaptive resistance to drug-induced apoptosis. Mol Syst Biol. 2015;11: 797. doi:10.15252/msb.20145877

23. Jenkins JL. Drug discovery: Rethinking cellular drug response. Nat Chem Biol. 2013;9: 669–670. doi:10.1038/nchembio.1365

24. Gascoigne KE, Taylor SS. Cancer cells display profound intra- and interline variation following prolonged exposure to antimitotic drugs. Cancer Cell. 2008;14: 111–122. doi:10.1016/j.ccr.2008.07.002

25. Cohen AA, Geva-Zatorsky N, Eden E, Frenkel-Morgenstern M, Issaeva I, Sigal A, et al. Dynamic proteomics of individual cancer cells in response to a drug. Science. 2008;322: 1511–1516. doi:10.1126/science.1160165

26. Berenbaum MC. In vivo determination of the fractional kill of human tumor cells by chemotherapeutic agents. Cancer Chemother Rep. 1972;56: 563–571.

27. Emmons MF, Faião-Flores F, Smalley KSM. The role of phenotypic plasticity in the escape of cancer cells from targeted therapy. Biochem Pharmacol. 2016;122: 1–9. doi:10.1016/j.bcp.2016.06.014

28. Kochanowski K, Morinishi L, Altschuler S, Wu L. Drug persistence - from antibiotics to cancer therapies. Curr Opin Syst Biol. 2018;10: 1–8. doi:10.1016/j.coisb.2018.03.003

29. Hangauer MJ, Viswanathan VS, Ryan MJ, Bole D, Eaton JK, Matov A, et al. Drug-tolerant persister cancer cells are vulnerable to GPX4 inhibition. Nature. 2017;551: 247–250. doi:10.1038/nature24297

30. Shaffer SM, Dunagin MC, Torborg SR, Torre EA, Emert B, Krepler C, et al. Rare cell variability and drug-induced reprogramming as a mode of cancer drug resistance. Nature. 2017;546: 431–435. doi:10.1038/nature22794

31. Sharma SV, Lee DY, Li B, Quinlan MP, Takahashi F, Maheswaran S, et al. A chromatin-mediated reversible drug-tolerant state in cancer cell subpopulations. Cell. 2010;141: 69–80. doi:10.1016/j.cell.2010.02.027

32. Bivona TG, Doebele RC. A framework for understanding and targeting residual disease in oncogene-driven solid cancers. Nat Med. 2016;22: 472–478. doi:10.1038/nm.4091

33. Wei G, Margolin AA, Haery L, Brown E, Cucolo L, Julian B, et al. Chemical Genomics Identifies Small-Molecule MCL1 Repressors and BCL-xL as a Predictor of MCL1 Dependency. Cancer Cell. 2012;21: 547–562. doi:10.1016/j.ccr.2012.02.028

34. Ramirez M, Rajaram S, Steininger RJ, Osipchuk D, Roth MA, Morinishi LS, et al. Diverse drug-resistance mechanisms can emerge from drug-tolerant cancer persister cells. Nat Commun. 2016;7: 10690. doi:10.1038/ncomms10690

35. Rambow F, Rogiers A, Marin-Bejar O, Aibar S, Femel J, Dewaele M, et al. Toward Minimal Residual Disease-Directed Therapy in Melanoma. Cell. 2018;174: 843-855.e19. doi:10.1016/j.cell.2018.06.025

36. Oxnard GR. The cellular origins of drug resistance in cancer. Nat Med. 2016;22: 232–234. doi:10.1038/nm.4058

37. Tyson DR, Garbett SP, Frick PL, Quaranta V. Fractional proliferation: a method to deconvolve cell population dynamics from single-cell data. Nat Methods. 2012;9: 923–928. doi:10.1038/nmeth.2138

38. Palmer AC, Sorger PK. Combination Cancer Therapy Can Confer Benefit via Patient-to-Patient Variability without Drug Additivity or Synergy. Cell. 2017;171: 1678-1691.e13. doi:10.1016/j.cell.2017.11.009

39. Sakaue-Sawano A, Kurokawa H, Morimura T, Hanyu A, Hama H, Osawa H, et al. Visualizing spatiotemporal dynamics of multicellular cell-cycle progression. Cell. 2008;132: 487–498. doi:10.1016/j.cell.2007.12.033

40. Reyes J, Chen J-Y, Stewart-Ornstein J, Karhohs KW, Mock CS, Lahav G. Fluctuations in p53 Signaling Allow Escape from Cell-Cycle Arrest. Mol Cell. 2018;71: 581-591.e5. doi:10.1016/j.molcel.2018.06.031

41. Smalley KSM, Lioni M, Dalla Palma M, Xiao M, Desai B, Egyhazi S, et al. Increased cyclin D1 expression can mediate BRAF inhibitor resistance in BRAF V600E-mutated melanomas. Mol Cancer Ther. 2008;7: 2876–2883. doi:10.1158/1535-7163.MCT-08-0431

42. Roesch A, Vultur A, Bogeski I, Wang H, Zimmermann KM, Speicher D, et al. Overcoming intrinsic multidrug resistance in melanoma by blocking the mitochondrial respiratory chain of slow-cycling JARID1B(high) cells. Cancer Cell. 2013;23: 811–825. doi:10.1016/j.ccr.2013.05.003

43. Emmons MF, Faião-Flores F, Sharma R, Thapa R, Messina JL, Becker JC, et al. HDAC8 Regulates a Stress Response Pathway in Melanoma to Mediate Escape from BRAF Inhibitor Therapy. Cancer Res. 2019;79: 2947–2961. doi:10.1158/0008-5472.CAN-19-0040

44. Maertens O, Kuzmickas R, Manchester HE, Emerson CE, Gavin AG, Guild CJ, et al. MAPK Pathway Suppression Unmasks Latent DNA Repair Defects and Confers a Chemical Synthetic Vulnerability in BRAF-, NRAS-, and NF1-Mutant Melanomas. Cancer Discov. 2019;9: 526–545. doi:10.1158/2159-8290.CD-18-0879

45. Wang L, Leite de Oliveira R, Huijberts S, Bosdriesz E, Pencheva N, Brunen D, et al. An Acquired Vulnerability of Drug-Resistant Melanoma with Therapeutic Potential. Cell. 2018;173: 1413-1425.e14. doi:10.1016/j.cell.2018.04.012

46. Echevarría-Vargas IM, Reyes-Uribe PI, Guterres AN, Yin X, Kossenkov AV, Liu Q, et al. Co-targeting BET and MEK as salvage therapy for MAPK and checkpoint inhibitor-resistant melanoma. EMBO Mol Med. 2018;10. doi:10.15252/emmm.201708446

47. Yu Y, Schleich K, Yue B, Ji S, Lohneis P, Kemper K, et al. Targeting the Senescence-Overriding Cooperative Activity of Structurally Unrelated H3K9 Demethylases in Melanoma. Cancer Cell. 2018;33: 322-336.e8. doi:10.1016/j.ccell.2018.01.002

48. Su Y, Lu X, Li G, Liu C, Kong Y, Lee JW, et al. Kinetic Inference Resolves Epigenetic Mechanism of Drug Resistance in Melanoma. Cancer Biology; 2019 Aug. doi:10.1101/724740

49. Khaliq M, Fallahi-Sichani M. Epigenetic Mechanisms of Escape from BRAF Oncogene Dependency. Cancers. 2019;11. doi:10.3390/cancers11101480

50. Schindelin J, Arganda-Carreras I, Frise E, Kaynig V, Longair M, Pietzsch T, et al. Fiji: an open-source platform for biological-image analysis. Nat Methods. 2012;9: 676–682. doi:10.1038/nmeth.2019

51. Jones TR, Carpenter AE, Lamprecht MR, Moffat J, Silver SJ, Grenier JK, et al. Scoring diverse cellular morphologies in image-based screens with iterative feedback and machine learning. Proc Natl Acad Sci. 2009;106: 1826–1831. doi:10.1073/pnas.0808843106

52. Tinevez JY. TrackMate: An open and extensible platform for single-particle tracking. 2016. Available: http://www.sciencedirect.com/science/article/pii/S1046202316303346

53. Roell KR, Reif DM, Motsinger-Reif AA. An Introduction to Terminology and Methodology of Chemical Synergy-Perspectives from Across Disciplines. Front Pharmacol. 2017;8: 158. doi:10.3389/fphar.2017.00158

54. Lecca P. Stochastic chemical kinetics : A review of the modelling and simulation approaches. Biophys Rev. 2013;5: 323–345. doi:10.1007/s12551-013-0122-2

55. Albeck JG, Burke JM, Spencer SL, Lauffenburger DA, Sorger PK. Modeling a snap-action, variable-delay switch controlling extrinsic cell death. PLoS Biol. 2008;6: 2831–2852. doi:10.1371/journal.pbio.0060299

Chapter 3 AP-1 Transcription Factor Network Explains Diverse Patterns of Cellular Plasticity in Melanoma

3.1 Introduction

Individual cells, even those derived from the same clone, respond heterogeneously to environmental perturbations [1,2]. Nongenetic heterogeneity can arise due to variances associated with transcriptional state plasticity [1,3–5]. Although such plasticity is required for the proper development of complex organisms [6], it limits the efficacy of therapies that target abnormally-activated signaling pathways [7,8]. An example of cell-to-cell transcriptional heterogeneity with phenotypic consequences for therapy resistance is observed in melanomas [9–11]. Numerous studies have associated fluctuations in the state of MAPK inhibitor sensitivity across BRAF-mutant melanoma cells to intrinsic variations in their differentiation state [12–17]. The reported heterogeneity spans a range of transcriptionally distinguishable states, including a relatively drug-sensitive, melanocytic phenotype that expresses melanocyte lineage markers SOX10 and MITF [18], to less drug-sensitive states, including neural crest-like cells that express NGFR [9,19], and undifferentiated cells characterized by the overexpression of AXL and loss of SOX10 and MITF [20,21]. In addition to intrinsic disparities in differentiation state, drug-induced adaptive responses may help a fraction of cells rewire their state of MAPK inhibitor sensitivity, most commonly through dedifferentiation (concomitant with loss of MITF and acquisition of NGFR) [9,13,22] or reactivation of the MAPK pathway [23,24]. Although the emergence and consequences of such intrinsic and adaptive heterogeneities are widely recognized, there is still more to learn about their origins and their possible connection at a molecular level. For example, it is unclear whether these seemingly distinct forms of heterogeneity arise from independent mechanisms, or whether the observed variability in the initial state of cells and their adaptive changes following MAPK inhibitor treatment could both be traced back to a common subset of molecular players.

Transcription factor networks that regulate the expression of genes in response to signaling pathway perturbations play a key role in creating the biological noise that leads to population heterogeneity [25,26]. The AP-1 protein family comprises one such network that serves as a major transcription node, integrating inputs from the upstream MAPK signaling pathway [27]. In addition to linking signal transduction to transcription, AP-1 proteins have been recently identified to serve as pioneer factors, establishing chromatin states that predispose cells to transcriptional programs driven by other transcription factors or histone modifications, thereby guiding cells towards paths of differentiation or epigenetic reprogramming [28–31]. These roles are consistent with numerous reports on AP-1 proteins being involved in resistance to MAPK inhibitors, cell state heterogeneity, and therapy-induced dedifferentiation in melanomas and other cancers [9,14,32–40]. Despite these reports, we lack a clear understanding of the rules that define AP-1 behavior and its role in explaining the intrinsic plasticity and the diversity of adaptive responses to MAPK signaling perturbations. This gap in our knowledge may be addressed by a system-wide analysis with single-cell precision to reveal interdependencies between an array of AP-1 proteins, which comprise over a dozen transcription factors, including JUN, FOS, and ATF subfamilies [41], their post-translational modification states, and their association with melanoma cell phenotypes at a single-cell level.

In this chapter, we test the hypothesis that the state of the AP-1 transcription factor network determines the intrinsic diversity of phenotypic states (i.e., differentiation states) and adaptive responses to MAPK inhibitors in BRAF-mutated melanoma cells. We define the AP-1 state as the combinatorial concentrations of AP-1 proteins, their phosphorylation state, and their transcriptional activity, which are either measurable experimentally, or inferable by using bioinformatics tools. Our systems biology approach combines multiplexed measurements of the AP-1 state, MAPK signaling activity and differentiation state, at population and single-cell levels, across many genetically characterized melanoma cell lines before and after their exposure to BRAF/MEK inhibitors. We apply statistical learning to capture the predictivity of AP-1 states, and corresponding AP-1 factors, for phenotypic heterogeneity in melanoma cultures and patient-derived tumors. We then employ RNAi-mediated knockdown experiments combined with single-cell analysis to validate the causality of our statistical predictions in a heterogeneous melanoma cell population. We find that a tightly regulated balance between AP-1 transcription factors cJUN, FRA2, FRA1 and cFOS and their transcriptional activity determines the baseline differentiation state of melanoma cells. This balance is perturbed following MAPK pathway inhibition. Nevertheless, MAPK-inhibitor-induced changes in the AP-1 state, including the abundance of cJUN and its phosphorylation, as well as the phosphorylation state of FRA1, remain strong predictors of drug-induced dedifferentiation and adaptive MAPK pathway reactivation, respectively. These results show that the state of AP-1 network offers a critical context, which controls not only the initial state of melanoma cells and their population heterogeneity, but also their adaptive changes immediately following MAPK pathway inhibition. Thus, AP-1 may serve as a critical node for strategies to manipulate cellular plasticity in melanoma with potential therapeutic implications.

3.2 Results

3.2.1 Single-cell AP-1 protein levels predict differentiation state heterogeneity in melanoma cells

To quantify the baseline heterogeneities in differentiation state and to assess their covariation with AP-1 proteins across genetically diverse or isogenic melanoma cell populations, we utilized an iterative indirect immunofluorescence imaging (4i) protocol [42] in conjunction with high-throughput automated microscopy (Figure 3.1). Dr. Douglas Baumann, our experimental collaborator from the Fallahi-Sichani lab, collected multiplexed measurements of 21 proteins using 4i-validated antibodies in 19 BRAF-mutant melanoma cell lines (Figure 3.2). The measurements included total levels of eleven AP-1 transcription factors (including cFOS, FRA1, FRA2, cJUN, JUNB, JUND, ATF2, ATF3, ATF4, ATF5 and ATF6), six AP-1 phosphorylation states (including p-cFOS^{S32}, p-FRA1^{S265}, p-cJUN^{S73}, p-ATF1^{S63}, p-ATF2^{T71} and p-ATF4^{S245}) and four differentiation state markers MITF, SOX10, NGFR and AXL.

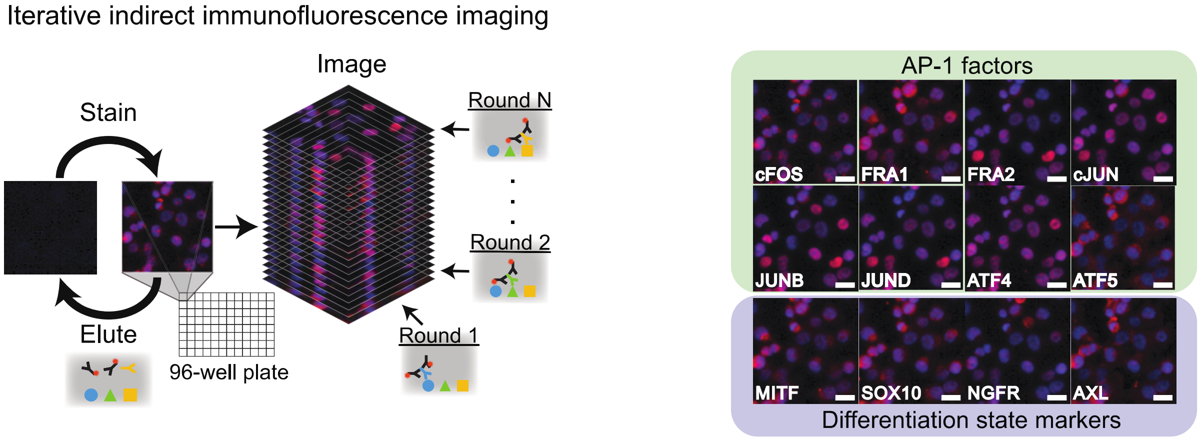

Figure 3.1 Schematic representation of the iterative indirect immunofluorescence imaging (4i) procedure used in this study

Illustration of the 4i procedure used to generate multiplexed single-cell data on 17 AP-1 proteins and 4 differentiation state markers. Representative images of selected AP-1 transcription factors and differentiation state markers are shown for LOXIMVI cells. Scale bars represent 20 µm. Hoechst staining of nuclei is shown in blue while staining of the indicated protein is shown in red.

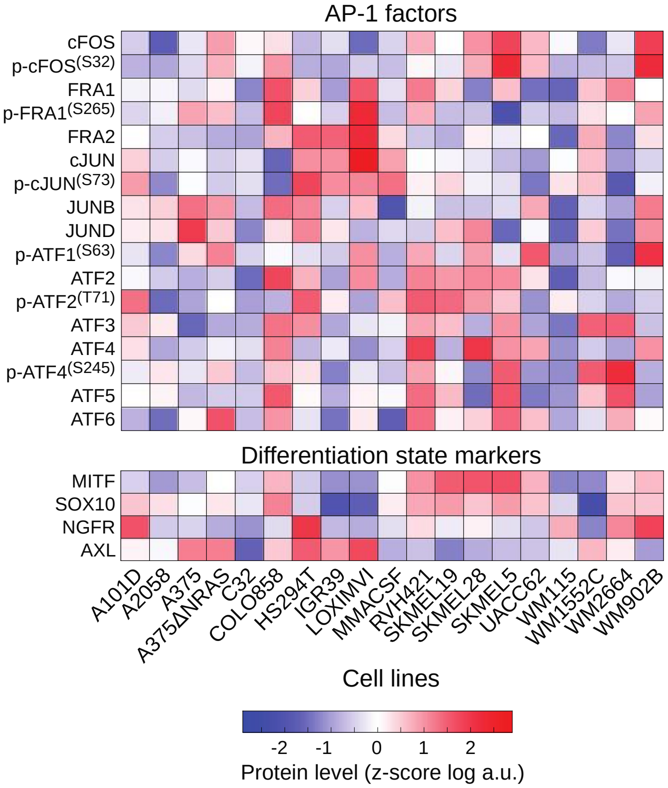

Figure 3.2 Population-averaged measurements of AP-1 proteins and differentiation state markers across BRAF-mutant melanoma cell lines

Population-averaged measurements of 17 AP-1 proteins and 4 differentiation state markers acquired across 19 BRAF-mutant melanoma cell lines. Protein data shown for each condition represent the log-transformed mean values for two replicates, followed by z-scoring across all cell lines.

Importantly, these four differentiation state markers were previously reported to represent transcriptionally distinct melanoma differentiation states [12,16]. The panel of 19 melanoma cell lines tested represented a broad spectrum of differentiation states, including populations of melanocytic ($MITF^{High}$ /$SOX10^{High}$ /$NGFR^{Low}$ /AXL^{Low}), transitory ($MITF^{High}$ /$SOX10^{High}$ /$NGFR^{High}$ /AXL^{Low}), neural crest-like ($MITF^{Low}$ /$SOX10^{High}$ /$NGFR^{High}$ /AXL^{High}) and undifferentiated ($MITF^{Low}$ /$SOX10^{Low}$ /$NGFR^{Low}$ /AXL^{High}) cells (Figure 3.3, Figure 3.4). We and others have shown that the frequency of these states in melanoma cell populations varies from one tumor to another and predicts their overall sensitivity to MAPK inhibitors [13,16,43].

Here, we asked whether the observed heterogeneities in differentiation state could be explained by variations in patterns of AP-1 measurements at a single-cell level.

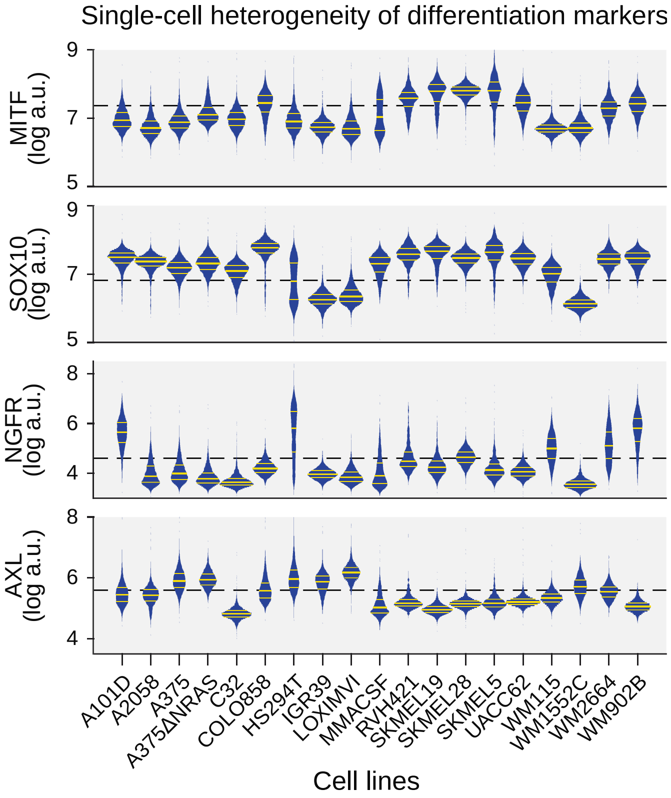

Figure 3.3 Single-cell heterogeneity in differentiation states within and across melanoma cell lines

Single-cell distribution of differentiation state markers MITF, SOX10, NGFR and AXL across 19 cell lines, shown by violin plots highlighting the median and interquartile (25% and 75%) ranges.

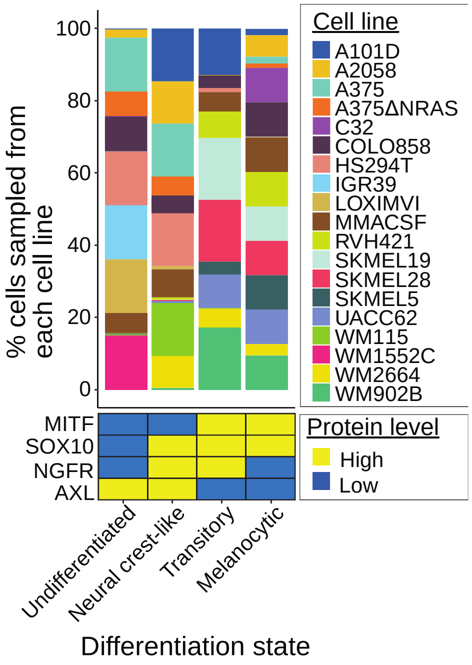

Figure 3.4 Cell-line representations across differentiation states of the sampled cell population.

The percentage of cells sampled from each of the 19 cell lines, and their corresponding differentiation states (defined based on MITF, SOX10, NGFR and AXL levels) used in the random forest model.

The population-averaged and single-cell protein data revealed a high degree of variation in differentiation state markers and AP-1 proteins across genetically distinct cell lines (Figure 3.2, Figure 3.3, Figure A.1). To test whether there is a relationship between AP-1 variations and the differentiation state of individual cells regardless of their genetic differences, we randomly sampled a total of 10,000 cells, including 2,500 from each of the four differentiation states, in a way that they represented all 19 cell lines and 4 distinctive differentiation states as equally as possible (Figure 3.4). We used the multiplexed AP-1 data of 80% of the cells to train a random forest classification model to predict the differentiation state of each individual cell. We then used the remaining 20% of the cell population to independently validate model predictions. Model-predicted single-cell differentiation states matched true (measured) differentiation states with an accuracy of 0.74, representing a remarkable performance relative to a random 4-class classifier with an expected accuracy of 0.25 (Figure 3.5). A close look at model predictions showed that they matched true states for ~88% of undifferentiated cells, ~72% of neural crest-like cells and >66% of melanocytic cells. In cases where the true and predicted state of a cell did not match, the model predicted a closely related neighboring state along the differentiation state trajectory. When we combined cells from these related states, e.g., cells in melanocytic and transitory states, the model was able to distinguish them from the other two states with an accuracy of >90% (Figure 3.5).

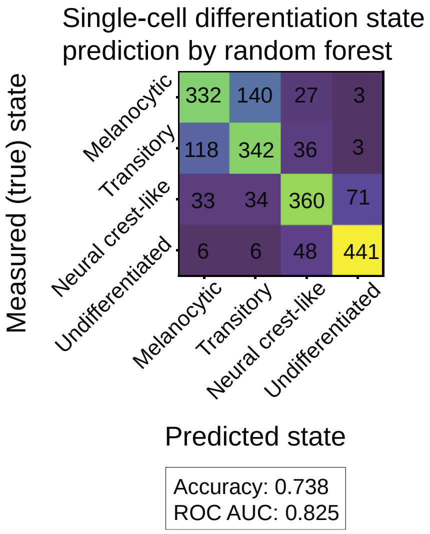

Figure 3.5 Single-cell AP-1 protein levels predict differentiation state heterogeneity in melanoma

Confusion matrix showing the independent validation performance of the random forest classifier in predicting the differentiation state of cells based on single-cell AP-1 measurements. The model was trained using a group of 8,000 cells and validated using an independent group of 2,000 cells. The prediction accuracy and area under the receiver operating characteristic curve (ROC AUC) are shown as an overall measure of the classifier performance.

To identify those AP-1 measurements that most strongly predicted single-cell differentiation state, we computed the SHapley Additive exPlanations (SHAP) values for the random forest classifications [44]. SHAP assigns each AP-1 factor an importance value, quantifying its contribution, either positively or negatively, to the predicted differentiation state of any given cell (Figure 3.6A). Among the most important AP-1 factors (ranked based on mean absolute SHAP values) were p-cFOS, FRA2, ATF4, cFOS, p-FRA1 and cJUN. Single-cell measurements of these six factors made it possible to predict the differentiation state of a cell with an accuracy of 67% (Figure 3.6B). In agreement with the SHAP analysis results, dimensionality reduction by Uniform Manifold Approximation and Projection (UMAP) [45] using only the top six AP-1 factors resulted in a continuous trajectory ordered from melanocytic to undifferentiated states (Figure 3.7). Together, these analyses revealed that the heterogeneity in melanoma differentiation state was associated with distinguishable patterns of variation in the expression of a few key AP-1 proteins. Melanocytic and transitory cells expressed substantially higher levels of p-cFOS, cFOS and ATF4, while undifferentiated cells exhibited lower levels of all these factors and instead exhibited increased levels of FRA2, cJUN and p-FRA1.

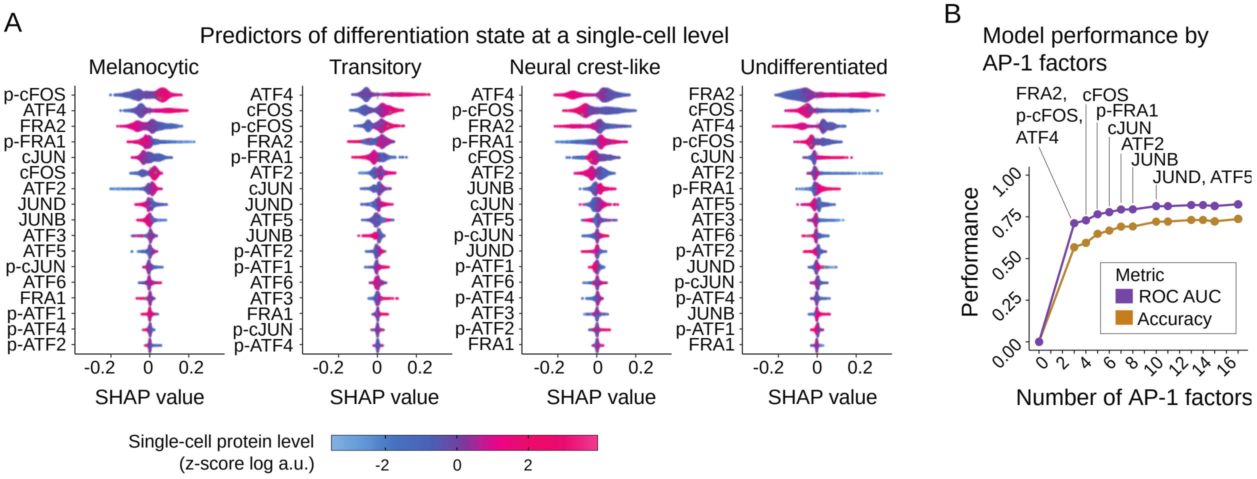

Figure 3.6 Identifying the most important AP-1 factors for single-cell differentiation-state prediction using SHAP

(A) Distributions of Shapley Additive exPlanations (SHAP) scores for each AP-1 factor across individual cells from the independent validation set. The color indicates the z-score scaled, log-transformed level of each AP-1 protein at a single-cell level. For each differentiation state, AP-1 factors are ordered based on the mean absolute values of their SHAP scores. **(B)** Classification performance of the random forest model based on varying numbers of top AP-1 factors (based on their SHAP values) used as predictors.

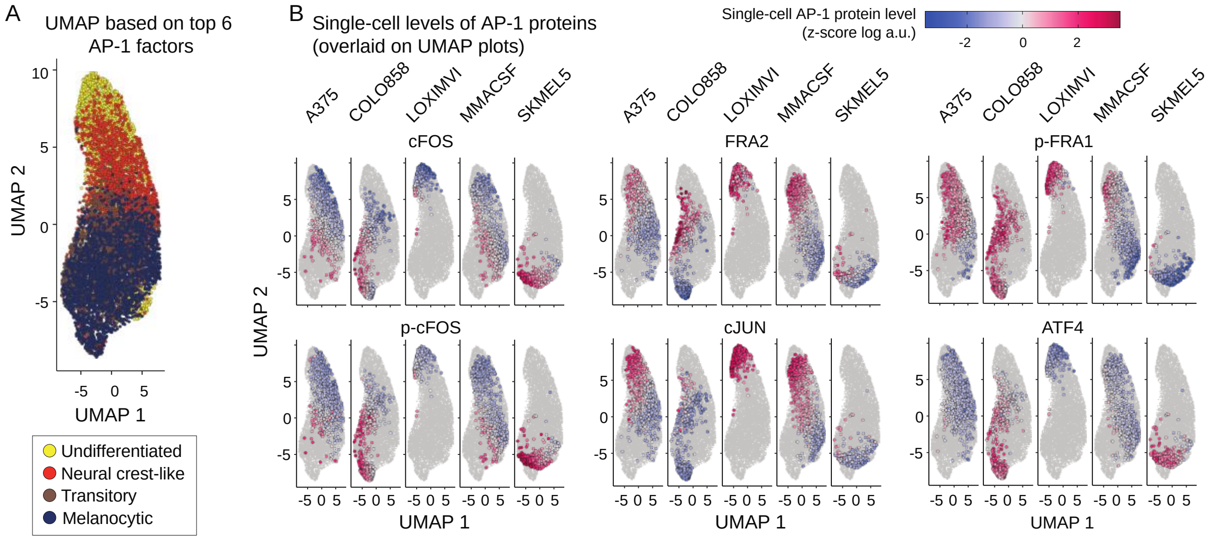

Figure 3.7 Top six AP-1 factors identified from the random forest model resolve the melanoma differentiation trajectory.

(A) UMAP analysis of the sampled melanoma cells (as shown in Figure 3.4) based on their multiplexed levels of top 6 predictive AP-1 measurements (FRA2, p-cFOS, ATF4, cFOS, p-FRA1 and cJUN) results in a continuous trajectory of differentiation states. **(B)** Single-cell levels of the top six AP-1 proteins overlaid on UMAP plots.

3.2.2 AP-1 transcript levels predict variations in differentiation state programs across melanoma lines

To test whether the relationships between the patterns of AP-1 expression and melanoma differentiation state were recapitulated at the transcriptional level, we analyzed a previously published dataset, including RNA sequencing of 53 melanoma cell lines [12]. Each cell line was assigned a series of seven signature scores, defined as the average of z-scores for the expression levels of differentiation state signature genes [12]. The differentiation signature scores were then related to the transcript levels of 15 AP-1 genes for each cell line by partial least square regression (PLSR) (Figure 3.8A). The overall performance of the PLSR model was evaluated by computing the fraction of variance in signature scores explained (R^2) or predicted (Q^2) by changes in AP-1 gene expression (Figure 3.8B). The model revealed a high performance and prediction accuracy with R^2 of 0.72 and Q^2 of 0.55 (using leave-one-out cross-validation) for four PLSR components. To evaluate the accuracy of predictions for each differentiation state, we assessed the correlation between the signature scores derived from the differentiation signature genes and scores predicted by the PLSR model. The model showed consistent accuracy with an average Pearson's correlation coefficient of 0.74 ± 0.08 ($P = 3.2\times10^{-17}$ to 1.3×10^{-6}) between the actual and predicted signature scores (Figure 3.8A). To independently validate the model predictions, we used RNA sequencing data from a different panel of 32 BRAF-mutant melanoma cell lines in the Cancer Cell Line Encyclopedia (CCLE) [46]. The PLSR model trained against the original set of 53 cell lines was able to predict the differentiation signature scores in the new set of 32 melanoma cell lines, leading to an average Pearson's correlation coefficient of 0.65 ± 0.13 ($P = 2.3\times10^{-8}$ to 6.8×10^{-3}) between the actual and predicted scores (Figure 3.8C).

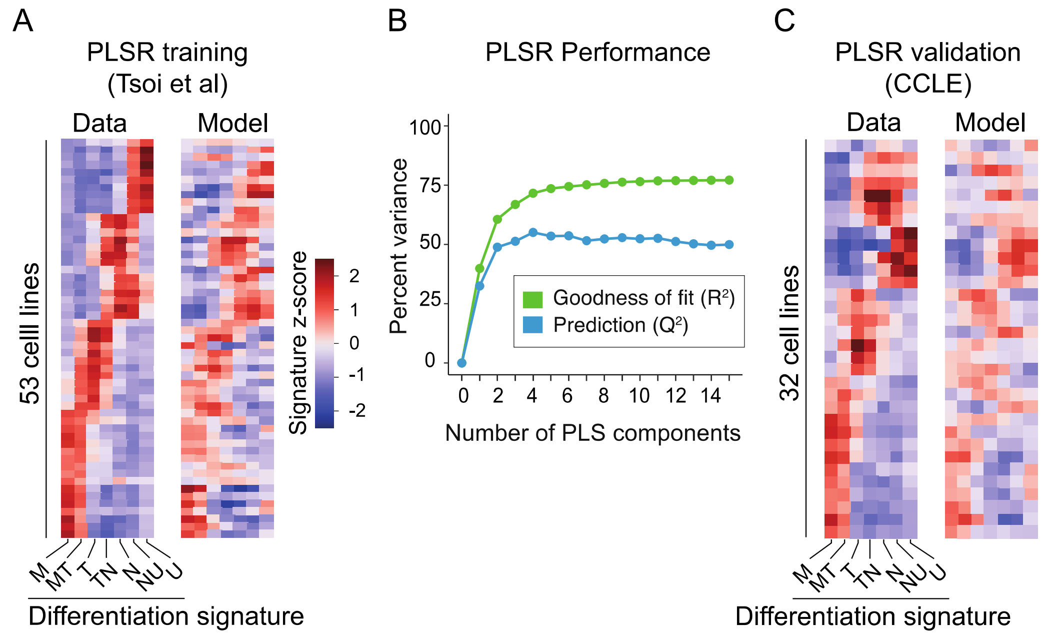

Figure 3.8 AP-1 transcript levels predict variations in differentiation state across melanoma lines.

(A) Comparison between differentiation signature scores computed based on RNA sequencing data for 53 cell lines reported by Tsoi *et al* [12] (left) and PLSR-predicted scores (following leave-one-out cross-validation) for each cell line based on their transcript levels of 15 AP-1 genes (right). M: melanocytic; MT: melanocytic-transitory; T: transitory; TN: transitory-neural crest-like; N: neural crest-like; NU: neural crest-like-undifferentiated; U: undifferentiated. **(B)** Performance of the PLSR model evaluated by computing the fraction of variance in differentiation signature scores explained (R^2) or predicted based on leave-one-out cross validation (Q^2) with increasing number of PLS components. **(C)** Comparison between differentiation signature scores computed based on

RNA sequencing data of 32 CCLE cell lines (left) and predicted scores based on the PLSR model built for the original set of 53 cell lines (right).

The high performance of the PLSR model shows that variations in the transcriptional levels of at least some AP-1 genes may explain the variability in differentiation states across melanoma cell lines. In agreement with this expectation, different cell lines could be separated by their PLSR scores based on their position along the different state trajectory (Figure 3.9). Because the PLSR model achieved its maximum prediction accuracy by four components, we computed the Variable Importance in the Projection (VIP) scores across all these components to determine the overall contribution of each AP-1 gene to each differentiation state (Figure 3.10). Among the most important predictors of differentiation state (determined by $|VIP| > 1$) were the expression of FOS (encoding cFOS), FOSL1 (encoding FRA1), FOSL2 (encoding FRA2), JUN (encoding cJUN), JUNB, JUND, ATF2 and ATF4 (Figure 3.10). Importantly, a model created using only these AP-1 genes was able to significantly outperform most PLSR models that were built based on combinations of eight randomly chosen transcription factors from the basic leucine zipper (bZIP) family (the family to which AP-1 factors belong) ($P = 0.008$) or based on any eight randomly chosen transcription factors ($P = 0.01$) (Figure 3.11).

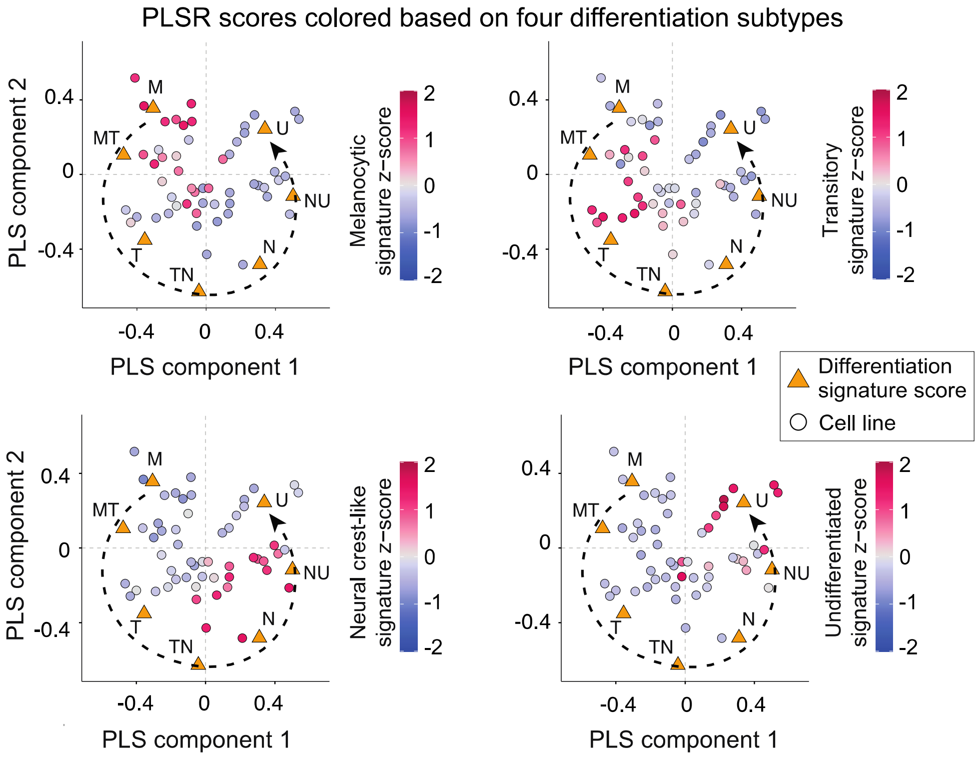

Figure 3.9 PLSR scores of the first two PLS components separate cell lines following the differentiation trajectory.

PLSR scores (of the first two PLS components) for each cell line colored according to their differentiation signature scores for melanocytic, transitory, neural crest-like and undifferentiated states. M: melanocytic; MT: melanocytic-transitory; T: transitory; TN: transitory-neural crest-like; N: neural crest-like; NU: neural crest-like-undifferentiated; U: undifferentiated.

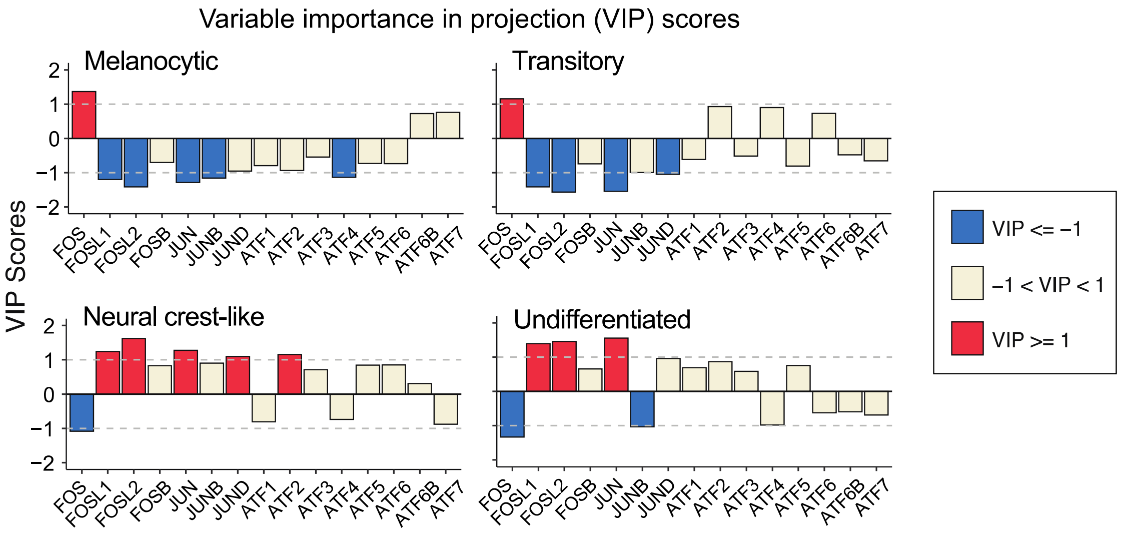

Figure 3.10 VIP scores quantifying AP-1 transcript importance across differentiation states.

PLSR-derived variable importance in projection (VIP) scores, highlighting combinations of AP-1 transcripts that are predictive of differentiation signature scores for melanocytic, transitory, neural crest-like and undifferentiated states. The sign of the VIP score shows whether the indicated variable (AP-1 transcript level) positively or negatively contributes to a given differentiation signature. Only significant VIP scores (of greater than 1 or smaller than -1) are highlighted.

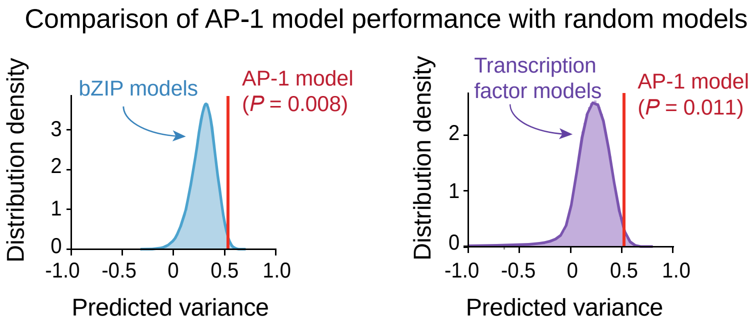
Comparison of AP-1 model performance with random models

Figure 3.11 PLSR model built based on the transcript levels of top 8 AP-1 genes outperforms most models built based on other bZIP transcription factors or transcription factors in general.

Comparison of performance (with respect to differentiation state prediction) between the PLSR model based on transcript levels of the top 8 AP-1 transcription factors with models based on transcript levels of combinations of 8 randomly chosen bZIP family transcription factors ($n = 1\times10^5$ iterations; left panel) or built based on 8 randomly chosen transcription factors ($n = 5\times10^5$ iterations; right panel). Empirical *P* values were reported for the comparison of predicted variances based on ten-fold cross-validation.

Together, these analyses revealed that the predictivity of patterns of AP-1 variation for melanoma differentiation state could also be captured at the level of transcription of these factors. Except for ATF4, the statistical association of AP-1 factors with differentiation state was generally consistent across bulk transcript and single-cell protein measurements. Melanocytic and transitory cells expressed substantially higher levels of FOS transcript and cFOS protein levels, whereas undifferentiated cells were associated with increased levels of FOSL1, FOSL2 and JUN transcripts and their corresponding proteins FRA1, FRA2 and cJUN, respectively.

3.2.3 Single-cell network inference reveals the role of AP-1 activity in regulation of differentiation programs

Next, we asked whether the statistical associations between the identified key AP-1 proteins and single-cell differentiation states resulted from the active regulation of differentiation programs by the AP-1 factors. To address this question, we applied single-cell regulatory network inference and clustering (SCENIC) [47,48] to analyze a previously published single-cell RNA sequencing dataset of 10 melanoma cell lines [14]. SCENIC uses single-cell gene expression data to infer transcription factors alongside their candidate target genes (collectively called a regulon), enabling the identification of regulatory interactions and transcription factor activities with high confidence. Enrichment analysis of differentiation signature genes among 10 cell lines showed that they predominantly consisted of cells in the melanocytic, transitory, or undifferentiated states. In line with our results from the gene and protein expression analyses, SCENIC analysis found the FOSL2 and JUN motif regulons to be substantially enriched in populations of undifferentiated cells in comparison with melanocytic or transitory cells (Figure 3.12A, B). The activity of the FOSL1 regulon was low in melanocytic cells but gradually increased among transitory and undifferentiated cells (Figure 3.12C). The FOS regulon, on the other hand, was substantially enriched in melanocytic and transitory cells, but its activity was low in undifferentiated cells (Figure 3.12D).

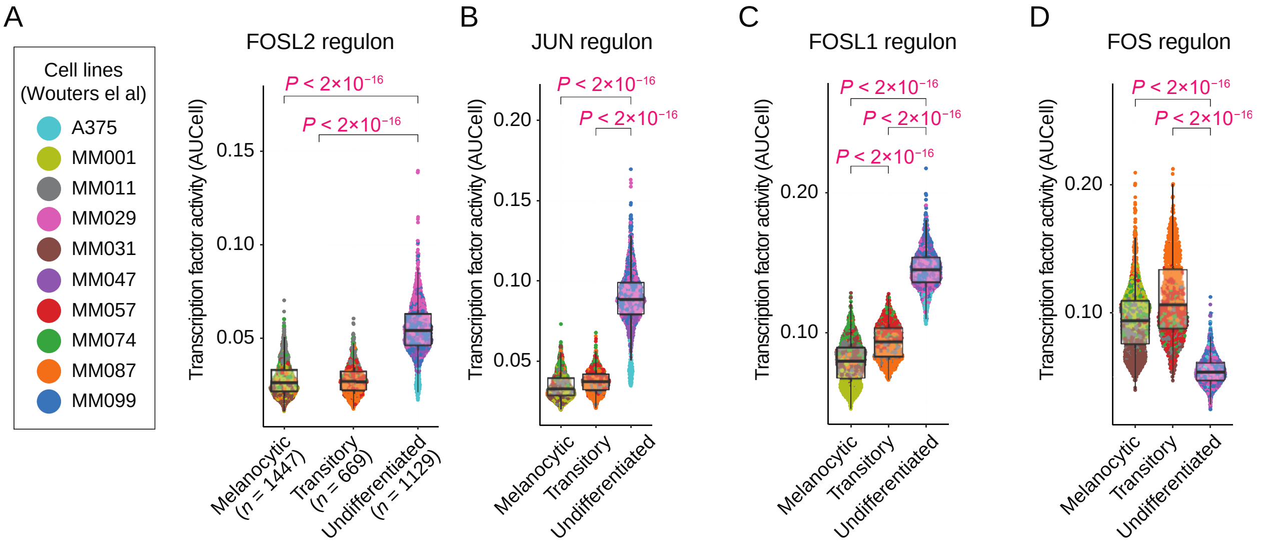

Figure 3.12 Single-cell network inference from melanoma cell lines reveals the role of AP-1 activity in regulation of differentiation state programs.

(A-D) Single-cell distributions of the activity of SCENIC regulons for FOSL2 **(A)**, JUN **(B)**, FOSL1 **(C)** and FOS **(D)** motifs, measured using AUCell in individual cells (from 10 melanoma cell lines profiled by Wouters *et al* [14]) across distinct differentiation states. The differentiation state of individual cells was determined based on their gated levels of enrichment (quantified by AUCell) for the differentiation gene signatures as defined by Tsoi *et al* [12].

Boxplot hinges correspond to the lower and upper quartiles, with a band at median. Whiskers indicate 1.5 times interquartile ranges.

To test whether the relationship between AP-1 regulon activities and melanoma differentiation states existed in single cells derived from tumor biopsies, we performed differentiation state enrichment and SCENIC analysis on single-cell RNA sequencing data previously collected via dissociation and profiling of patient-derived melanoma samples [43,49]. Enrichment analysis of differentiation signature genes among 11 treatment-naïve malignant melanoma samples showed that they consisted of cells in either melanocytic or undifferentiated states. In agreement with the analysis results from the established melanoma cultures, SCENIC analysis of patient tumors showed that FOSL2, JUN and FOSL1 regulons were significantly enriched in undifferentiated cells in comparison with melanocytic cells (Figure 3.13A-C). In contrast to a substantially higher FOS regulon activity observed in cultured melanocytic cells, the activity of FOS regulon was only slightly higher in melanocytic tumor cells in comparison with undifferentiated cells (Figure 3.13D). Interestingly, however, the FOS/JUN activity ratio at a single-cell level was able to distinguish melanocytic cells from undifferentiated cells more efficiently than either of these AP-1 factors alone (Figure 3.13E), suggesting that it is the balance between AP-1 factor activities that determines a cell’s differentiation state. Together, these analyses revealed that melanoma cells of diverse differentiation states are associated with distinct regulatory network activities by AP-1 transcription factors. In particular, the role of FOS, FOSL1, FOSL2 and JUN regulon activities was consistent with their corresponding patterns of gene and protein expression across melanoma differentiation states at both population and single-cell levels.

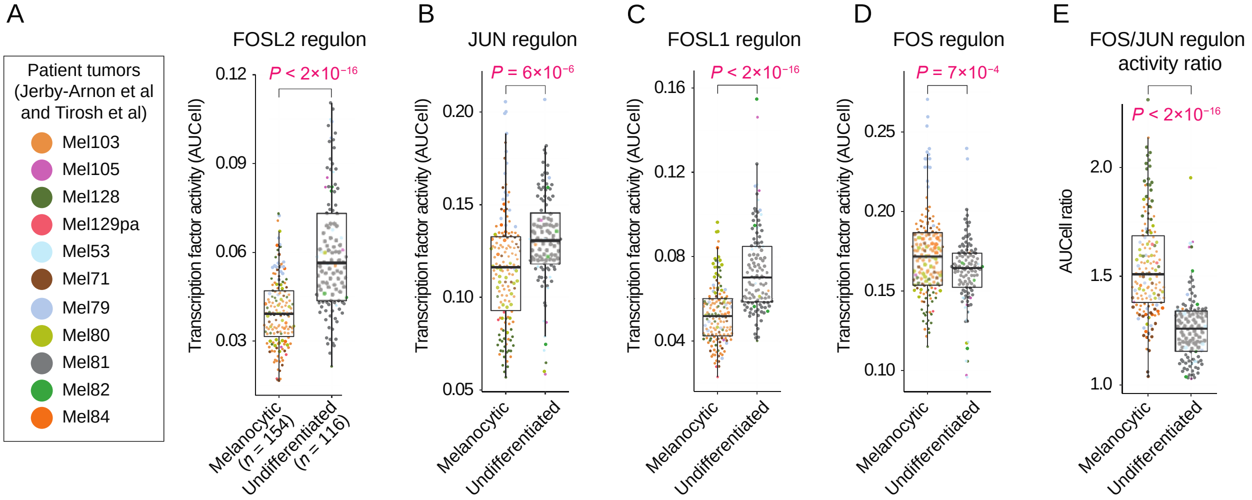

Figure 3.13 Single-cell network inference from patient-derived melanoma tumors reveals the role of AP-1 activity in regulation of differentiation state programs.

(A-E) Single-cell distributions of the AUCell activity of SCENIC regulons for FOSL2 **(A)**, JUN **(B)**, FOSL1 **(C)**, and FOS **(D)** motifs, as well as the ratio of FOS and JUN regulon activities **(E)**, quantified in individual cells from 11 treatment-naïve melanoma tumors as profiled by Tirosh *et al* [43] and Jerby-Arnon *et al* [49]. Statistical comparisons were performed using two-sided unpaired *t* test. Boxplot hinges correspond to the lower and upper quartiles, with a band at median. Whiskers indicate 1.5 times interquartile ranges.

3.2.4 MAPK inhibitor-induced changes in the AP-1 state predict patterns of drug-induced dedifferentiation and ERK pathway reactivation

Although melanoma populations consist of stable mixtures of cells in diverse differentiation states at baseline, they can switch state in response to environmental perturbations. Treatment with MAPK inhibitors, for example, may induce the dedifferentiation of melanocytic cells toward the neural crest-like phenotype. Such adaptive phenotype switching occurs as early as 2-3 days of exposure to MAPK inhibitors, concomitantly with loss of MITF and acquisition of NGFR [16]. In addition to drug-induced dedifferentiation, adaptive reactivation of the ERK pathway following a transient period of ERK inhibition is known as a common mechanism of adaptive resistance that helps tumor cells escape the effect of drug [23,24]. To determine common patterns of AP-1 changes that might be associated with these adaptive responses, we exposed 18 BRAF-mutant cell lines to the BRAF inhibitor vemurafenib (at 0.316 µM) either alone or in combination with the MEK inhibitor trametinib (at 0.0316 µM). We fixed the cells following 24 or 72 h of treatment and then used the 4i procedure to measure the abundance or phosphorylation state of AP-1 transcription factors, MITF, NGFR, and p-ERK$^{T202/Y204}$ (Figure 3.14, Figure A.2, Figure A.3).

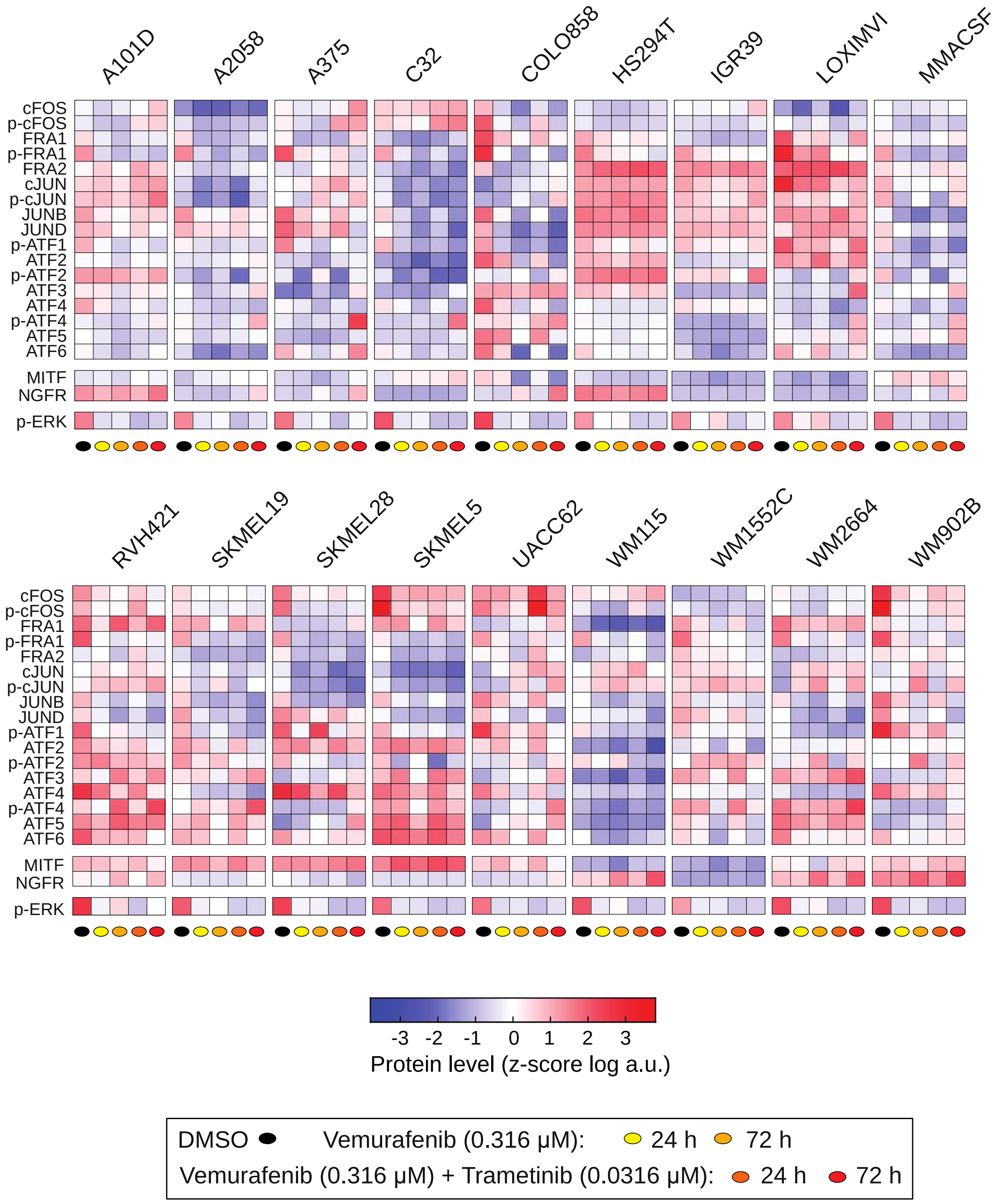

Figure 3.14 Population-averaged measurements of AP-1 proteins, differentiation state markers and ERK activity across BRAF-mutant melanoma cell lines upon 24 h and 72 h of MAPK inhibitor treatment.

Population-averaged measurements of 17 AP-1 proteins, differentiation state markers MITF and NGFR, and p-ERK$^{T202/Y204}$ levels acquired across 18 BRAF-mutant melanoma cell lines. Protein data shown for each condition represent the log-transformed mean values for two replicates, followed by z-scoring across all cell lines and treatment conditions, including DMSO, vemurafenib alone (at 0.316 µM) or the combination of vemurafenib (at 0.316 µM) and trametinib (at 0.0316 µM) for 24 or 72 h.

To identify possible associations between AP-1 factors and drug-induced dedifferentiation, we first calculated the relative enrichment of dedifferentiated cells at baseline (DMSO) or following MAPK inhibitor treatments by subtracting the fraction of cells that are NGFR^{Low}/MITF^{High} from the fraction of cells that are NGFR^{High}/MITF^{Low}. We then used pairwise partial correlation analysis to reveal statistical associations between each of the AP-1 measurements and the enrichment of dedifferentiated cells following MAPK inhibitor treatments across 18 cell lines, while controlling for the intrinsic (drug-naïve) variance in the enrichment of dedifferentiated cells across cell lines (Figure 3.15). This analysis identified cJUN and p-cJUN as the strongest predictors of drug-induced dedifferentiation in melanoma cells following 72 h of exposure to either of the MAPK inhibitors (Figure 3.16A). In agreement with population-level correlation analysis, single-cell analysis revealed significant increases in cJUN and p-cJUN levels of melanoma cells that switched from an NGFR^{Low}/ MITF^{High} state to an NGFR^{High}/ MITF^{Low} state following drug treatment (Figure 3.16B).

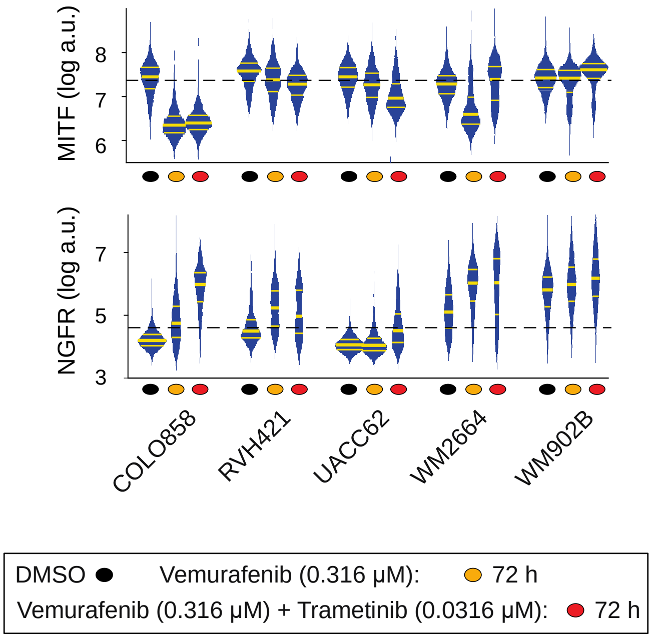

Figure 3.15 Single-cell distributions of differentiation state markers measured in five cell lines under the control or 72 h of MAPK inhibitor treatment.

Single-cell distributions of differentiation state markers MITF and NGFR in 5 cell lines that show MAPK inhibitor-induced dedifferentiation, shown by violin plots highlighting the median and interquartile (25% and 75%) ranges.

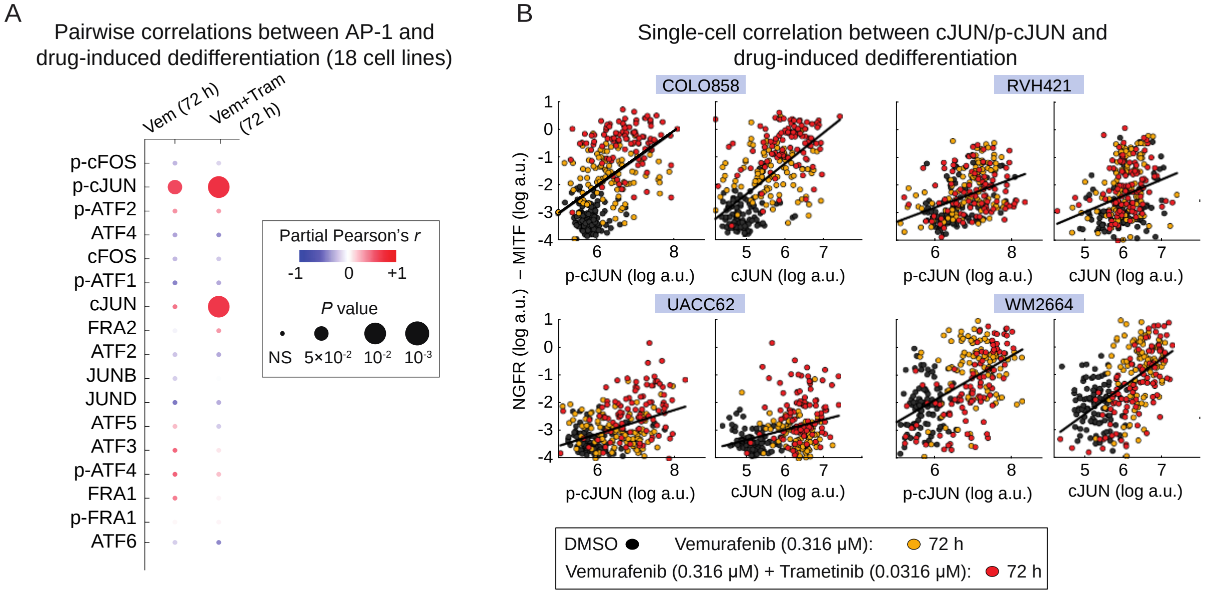

Figure 3.16 MAPK inhibitor-induced changes in cJUN/p-cJUN levels correlate with drug-induced dedifferentiation.

(A) Pairwise partial correlations (evaluated across 18 cell lines) between each of the 17 AP-1 measurements and the enrichment of NGFR^{High}/MITF^{Low} cells relative to NGFR^{Low}/MITF^{High} cells following 72 h treatment with MAPK inhibitors, while correcting for the baseline (drug-naïve) differentiation state of cell lines. Vem: vemurafenib alone; Vem+Tram: vemurafenib and trametinib in combination. **(B)** Analysis of covariance between the levels of p-cJUN or c-JUN and the difference between NGFR and MITF protein levels at the single-cell level across indicated treatment conditions.

We then asked which, if any, of AP-1 factors might capture drug-induced adaptive changes in ERK signaling. Consistent with previous data [24], treatment of cells with vemurafenib at 0.316 µM strongly suppressed the average p-ERK levels within 24 h in all cell lines (Figure 3.17). Each cell line, however, showed long-tailed single-cell distributions of p-ERK level, indicating significant cell-to-cell heterogeneity in ERK pathway inhibition. Over the following 48 h of vemurafenib treatment (i.e., t = 72 h), p-ERK levels were further elevated because of adaptive reactivation of ERK signaling (Figure 3.17). Cells treated with the combination of vemurafenib (at 0.316 µM) and trametinib (at 0.0316 µM), however, exhibited reduced p-ERK levels in comparison with cells treated with vemurafenib alone for either 24 or

72 h (Figure 3.17). To assess if any of the AP-1 factors would capture such time-dependent and drug-specific changes in ERK signaling, we used partial correlation analysis to determine pairwise correlations between p-ERK and AP-1 levels across 18 drug-treated cell lines. This analysis identified p-FRA1 as a consistent predictor of p-ERK changes following both MAPK inhibitor conditions (Figure 3.18A). In agreement with population-level correlation analysis, single-cell analysis also revealed a significant covariance between p-ERK and p-FRA1 levels (Figure 3.18B). Such strong connection between p-FRA1 and p-ERK is consistent with FRA1 serving as a tightly coupled sensor of ERK activity [50]. Together, these data reveal that in addition to predicting the differentiation state of melanoma cells at baseline, AP-1 changes following exposure to MAPK inhibitors are strong predictors of the ways that melanoma cells respond to MAPK inhibition.

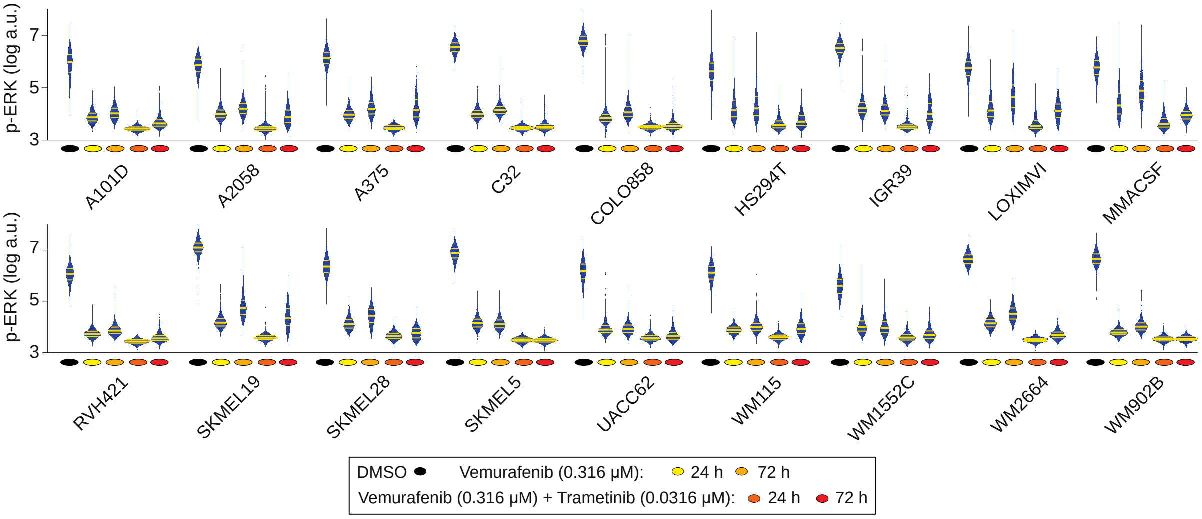

Figure 3.17 Single-distributions of p-ERK levels across melanoma cell lines under the control or MAPK inhibitor treatment.

Single-cell distribution of p-ERK$^{T202/Y204}$ level and its changes across different conditions, including DMSO, vemurafenib alone (at 0.316 µM) or the combination of vemurafenib (at 0.316 µM) and trametinib (at 0.0316 µM) for 24 or 72 h. Violin plots highlight the median and interquartile (25% and 75%) ranges.

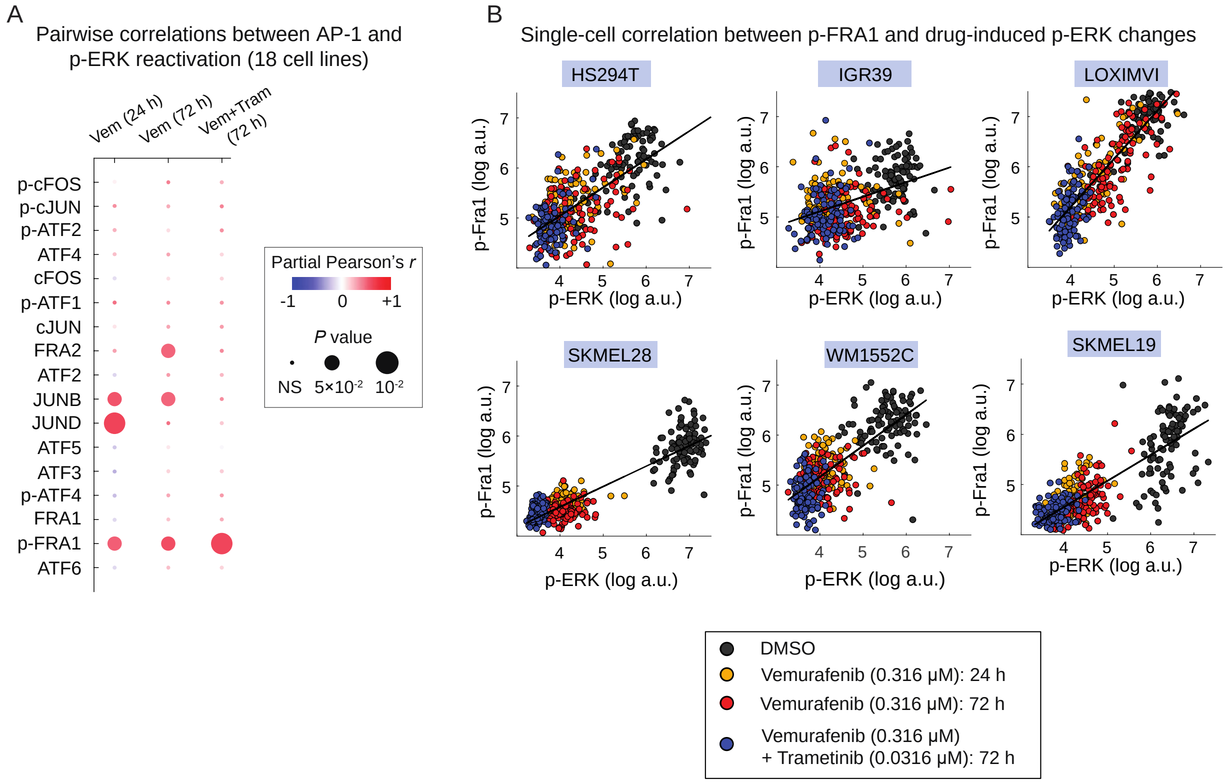

Figure 3.18 MAPK inhibitor-induced changes in p-FRA1 levels correlate with adaptive changes in ERK pathway activity.

(A) Pairwise partial correlations (evaluated across 18 cell lines) between each of the 17 AP-1 measurements and p-ERK levels following 24 or 72 h of treatment with MAPK inhibitors, while correcting for the corresponding baseline (drug-naïve) AP-1 levels of cell lines. **(B)** Analysis of covariance between p-FRA1 and p-ERK levels across indicated treatment conditions at the single-cell level.

3.2.5 Perturbation of AP-1 state by siRNA confirms its role in driving differentiation state heterogeneity

We hypothesized that if the AP-1 state drives melanoma differentiation programs, then inducing perturbations in the AP-1 state will shift differentiation states in predictable ways. To test this hypothesis, we perturbed AP-1 factors in COLO858 melanoma cells by using pools of previously validated siRNAs to deplete four AP-1 proteins cFOS, FRA2, cJUN, and JUND, either individually or in pairwise combinations. COLO858 represents a heterogenous population composed of both melanocytic and undifferentiated cells, thereby allowing us to track changes in the heterogeneity of differentiation state after AP-1 perturbations. Following 96 h of AP-1 gene knockdown in COLO858 cells, we measured (in three replicates) protein levels of differentiation markers MITF, SOX10 and AP-1 factors cFOS, FRA1, FRA2, cJUN, and JUND using 4i (Figure 3.19). As shown above, cFOS, FRA1, FRA2, and cJUN were able to consistently distinguish melanocytic/transitory (MITF^{High}/ SOX10^{High}) cells from undifferentiated (MITF^{Low}/ SOX10^{Low}) cells at the levels of gene expression, protein expression, and regulon activity. We thus asked whether siRNA-induced changes in the levels of these AP-1 proteins would be followed by predictable changes in the fractions of melanocytic/transitory or undifferentiated cells as evaluated by single-cell expression of MITF and SOX10 proteins.

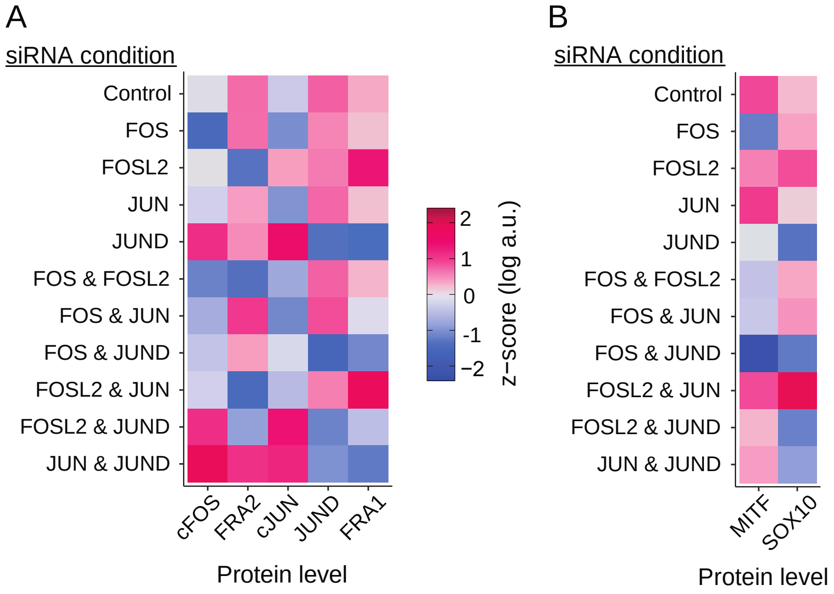

Figure 3.19 Population-averaged measurements of AP-1 proteins and differentiation state markers upon siRNA-mediated perturbation of the AP-1 state.

(A, B) The effect of siRNA-mediated depletion (for 96 h) of AP-1 proteins cFOS, FRA2, cJUN, and JUND, either individually or in pairwise combinations, on protein levels of cFOS, FRA1, FRA2, cJUN, and JUND **(A)** or differentiation state markers MITF and SOX10 **(B)** in COLO858 cells. Protein data shown for each condition represent the log-transformed mean values for three replicates, followed by z-scoring across all knockdown conditions.

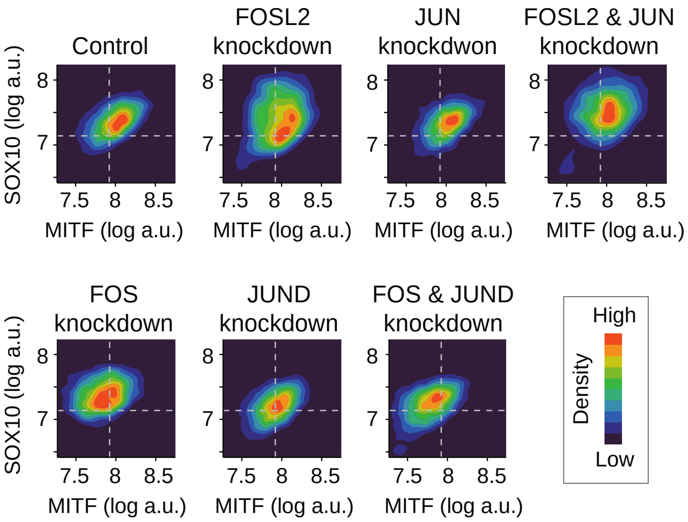

Figure 3.20 Changes in single-cell covariance between SOX10 and MITF upon siRNA-mediated perturbation of the AP-1 state.

Analysis of covariance between SOX10 and MITF protein levels across indicated knockdown conditions at the single-cell level. Dashed lines indicate the gating thresholds for each protein.

Interestingly, siRNA-mediated knockdowns not only reduced the levels of AP-1 proteins targeted by their corresponding siRNAs but also, in some cases, led to changes in the expression of other AP-1 proteins (Figure 3.19A). For example, FOSL2 knockdown substantially reduced FRA2 levels, but also induced the expression of FRA1 and cJUN, when compared to cells treated with non-targeting (control) siRNA. JUND knockdown reduced JUND levels, but also led to an increase in cFOS and cJUN levels. These observations agree with previous reports [51] indicating that the state of AP-1 network is controlled by feedback regulation and interactions among different AP-1 factors. Combinations of siRNAs against pairs of AP-1 genes may help reveal those interactions that are phenotypically consequential. To identify such interactions, we quantified the levels of SOX10 and MITF proteins across all knockdown conditions (Figure 3.19B, Figure 3.20), then computed the percentage of melanocytic/ transitory (SOX10^{High}/ MITF^{High}) cells and undifferentiated (SOX10^{Low}/ MITF^{Low}) cells in each condition (Figure 3.21A) and examined them along a two-dimensional plot (Figure 3.21B).We found that knocking down FOSL2 and JUN in combination, but not individually, reduced the percentage of undifferentiated cells most significantly and by approximately 2-fold (*P* = 0.002) (Figure 3.21B, C). This behavior is consistent with our finding regarding the role of FRA2 and cJUN in regulation of the undifferentiated state. Furthermore, it shows that the co-depletion of FRA2 and cJUN is essential for blocking the undifferentiated cells that otherwise up-regulate cJUN following the knockdown of FOSL2 alone (Figure 3.19A). On the other hand, knocking down FOS reduced the percentage of melanocytic/ transitory cells (*P* = 0.03) (Figure 3.21B, D), which is consistent with our finding regarding its role in driving the melanocytic lineage. Furthermore, the combination of FOS and JUND knockdown dramatically enhanced this effect, leading to a reduction of >2-fold in the percentage of melanocytic /transitory cells (*P* = 0.0001) and an increase of >2-fold in the percentage of undifferentiated cells (*P* = 0.01) (Figure 3.21B, D, E). As discussed above, this observation also could be explained by the induction of cJUN expression (a driver of dedifferentiation) following JUND knockdown.

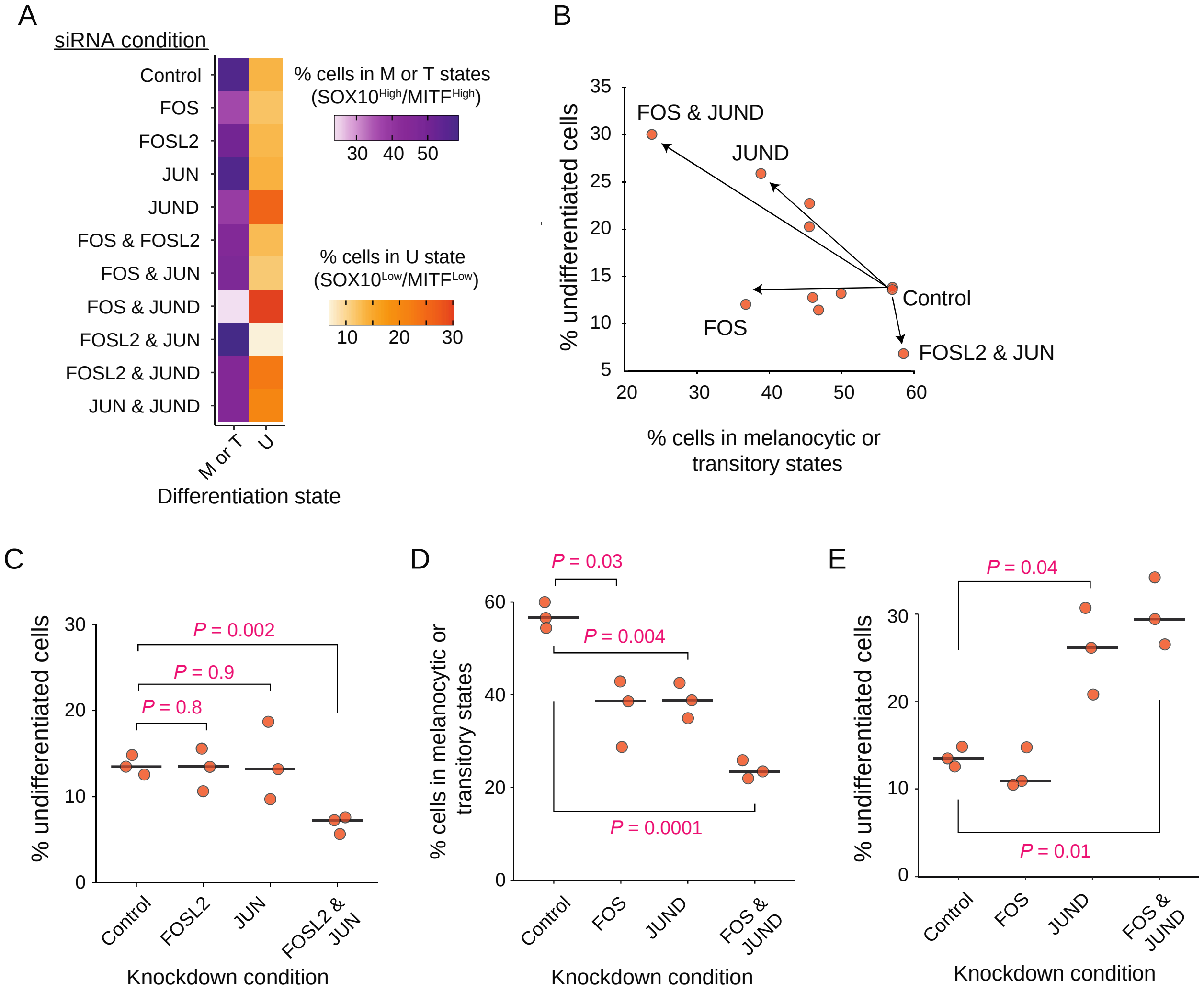

Figure 3.21 Perturbation of AP-1 state by siRNA confirms its role in driving differentiation state heterogeneity.

(A) Variation of the percentage of SOX10^{High}/MITF^{High} (melanocytic or transitory; M or T) cells and SOX10^{High}/MITF^{High} (undifferentiated; U) cells following each knockdown condition. **(B)** Two-dimensional projection of siRNA conditions in terms of percentages of melanocytic or transitory cells versus undifferentiated cells at 96 h. **(C-E)** Statistical comparison (using two-sided *t* test) between fractions of cells in undifferentiated or melanocytic/transitory states and indicated siRNA knockdown conditions. The central mark on the plots indicates the median across three replicates.

Together, these results validate the causality of our statistical predictions for the AP-1 state in contributing to differentiation state plasticity in melanoma cells. They show that a tightly regulated balance between JUN and FOS subfamily members determines the baseline differentiation state of a cell. Directed perturbation of this state leads to changes in the composition of differentiation states in a predictable manner.

3.3 Discussion

The hyperactivation of MAPK signaling in BRAF-mutant melanomas is linked to their overall sensitivity to MAPK inhibition. The differentiation state heterogeneity, however, leads to variability in MAPK inhibitor responses both across genetically diverse tumors and among genetically homogeneous populations of cells. Understanding the origins of such heterogeneity is key to identifying effective strategies to overcome fractional responses that undermine the potential of MAPK-targeted therapies. It requires a detailed knowledge of the mechanisms and molecular players that link epigenetic plasticity and transcriptional regulation of differentiation state to therapy-induced changes in MAPK signaling. To begin to fill this gap in our knowledge, we used a multidimensional approach at single-cell resolution to systematically investigate the AP-1 transcription factor contributions to heterogeneity in BRAF-mutant melanomas. We focus on the AP-1 factors because they serve as downstream targets of MAP kinases, and previous work has connected several AP-1 proteins to MAPK inhibitor resistance, differentiation state heterogeneity, and therapy-induced dedifferentiation in melanomas.

Our data showed that a tightly regulated balance between a few key AP-1 family members and their activities strongly predict previously characterized heterogeneities in melanoma differentiation states. Specifically, cFOS and p-cFOS were associated with melanocytic and transitory cells, while FRA1/p-FRA1, FRA2, and cJUN/p-cJUN correlated with less differentiated cell states. The systematic nature of the study across many genetically different melanomas suggests that these associations are a general feature of melanomas and likely not unique to a particular cell line or linked to a certain genetic context. Furthermore, we showed that perturbing the molecular balance of AP-1 factors in melanoma cells by siRNAs that deplete specific AP-1 proteins, either alone or in combination, or by treatments with MAPK inhibitors can induce differentiation state switching and heterogeneity in a controllable manner. Together, these findings provide new insights into AP-1 function, its role in cell state plasticity, and its potential dysregulation in melanoma, while opening new avenues for interrogating the AP-1 behavior in the context of adaptive response to MAPK inhibitors. In theory, gaining the ability to target certain AP-1 states could force cells to remain in a more drug-sensitive state, thereby increasing the fractional killing of melanoma cells in response to MAPK inhibition.

Future studies may leverage the findings from this study to further elucidate transcriptional mechanisms that contribute to MAPK-targeted therapy escape in melanomas at a single-cell level. Furthermore, uncovering how the information encoded in the MAPK signaling dynamics is transduced through its downstream AP-1 network will be key for explaining the observed variability in tumor cell responses to MAPK inhibitors. For example, AP-1 family members FOS and FOSL1 are early ERK target genes whose regulation by ERK activity constitutes feedforward motifs that enable them to decode the dynamics of ERK signaling [52]. Differentiation state-specific variations in the baseline expression and activities of these AP-1 genes, as we observed in this study, could introduce variability in the transduction of MAPK signals, generating heterogeneity in cell fate under MAPK perturbations. Future studies that link dynamic fluctuations in ERK activity and other MAP kinases to AP-1 behavior could offer important insights into mechanisms of heterogeneity in drug response and adaptive resistance to MAPK inhibitors.

Consistent with our findings regarding the role of AP-1 state changes in determining the differentiation state plasticity, recent studies have highlighted a key role for AP-1 factors in chromatin organization and enhancer accessibility. AP-1 proteins have been reported to facilitate new cell fate transitions, such as cellular senescence or differentiation, by establishing the enhancer landscape and granting long-term chromatin access to other transcription factors, thereby allowing the timely execution of cell state-specific transcriptional programs [28–31]. Understanding which AP-1 factors and cofactors work to keep poised enhancers accessible and which function to shift enhancers from a poised to active state could connect transcription to dedifferentiation and genome reorganization following inhibition of MAPK signaling and its adaptive reactivation. Furthermore, AP-1 proteins like other bZIP proteins must form dimers before they could bind to the AP-1 motif site. For example, while FOS family members bind DNA as obligate heterodimers with members of the JUN family, JUN family members can bind the AP-1 motif site as both homodimers and heterodimers with FOS family members. Future studies, therefore, should also determine the extent to which the combinatorial activity of AP-1 family members is influenced by distinct patterns of dimerization among these transcription factors.

3.4 Acknowledgments

We thank Dr. Douglas Baumann for developing protocols and performing all the experiments described in this chapter. We thank Kevin Janes and members of the Fallahi-Sichani laboratory for helpful suggestions and discussion. This work was supported by NIH grant R35-GM133404 (to MFS), the Farrow Fellowship (to DB) and P30-CA044579 (University of Virginia Cancer Center Support Grant). We acknowledge Research Computing at The University of Virginia for providing computational resources and technical support.

3.5 Materials and Methods

3.5.1 Cell culture and drug treatments

BRAF-mutant melanoma cell lines used in this study were obtained from the following sources: COLO858 (from ECACC), RVH421 (from DSMZ), A375, A375(NRAS^{Q61K}), C32, A2058, WM115, SKMEL28, HS294T, WM1552C, SKMEL5, A101D, and IGR39 (all from ATCC), LOXIMV1 (from DCTD Tumor Repository, National Cancer Institute), MMACSF (RIKEN BioResource Center), WM902B and WM2664 (from Wistar Institute), UACC62 and SKMEL19 (from the Cancer Cell Line Encyclopedia). All cell lines have been subjected to re-confirmation by short tandem repeat (STR) profiling by ATCC and mycoplasma testing by MycoAlert™ PLUS Mycoplasma Detection Kit (Lonza). A375, A375(NRAS^{Q61K}), A2058, HS294T, A101D, and IGR39 cells were grown in DMEM with 4.5 g/l glucose (Corning, Cat# 10-013-CV) supplemented with 5% fetal bovine serum (FBS) (Gibco Cat. No. 26140079). SKMEL5 and WM2664 cells were grown in EMEM (Corning, Cat# 10-009-CV) supplemented with 5% FBS. C32, MMACSF, SKMEL28, and WM115 cells were grown in DMEM/F12 (Gibco, Cat# 11330-032) supplemented with 1% sodium pyruvate (Gibco Cat. No. 11360070) and 5% FBS. COLO858, LOXIMVI, RVH421, SKMEL19, UACC62, WM1552C, and WM902B cells were grown in RPMI 1640 (Corning, Cat# 10-040-CV) supplemented with 1% sodium pyruvate and 5% FBS. Cells were grown at 37°C with 5% CO_2 in a humidified chamber. 100 U/mL Penicillin-Streptomycin (10,000 U/mL), and 0.5 mg/mL Plasmocin Prophylactic (Invivogen Cat. No. NC9886956) were present in all cell cultures. Cells were seeded in 200 µl/well in Corning 96-well plates (Cat. No. 3904). Vemurafenib (Selleck Chemicals Cat. No. S1267), Trametinib (Selleck Chemicals Cat. No. S2673) or vehicle (DMSO) was added at indicated concentrations using the Tecan D300e Digital Dispenser 24 hours after cell seeding. Cells were fixed at the indicated timepoints with 4% paraformaldehyde in phosphate-buffered saline (PBS) for 30 minutes at room temperature.

3.5.2 AP-1 gene knockdown by siRNA

COLO858 cells were seeded in 100 µl of antibiotic-free growth media (RPMI supplemented with 5% FBS and 1 mM Sodium Pyruvate) in 96-well plates at a density of 2000 cells/well. After 24 h of incubation, cells were transfected using 0.05 µl of DharmaFECT 2 reagent (Horizon Discovery Cat. No. T-2002-01) per well with indicated Dharmacon ON-TARGETplus AP-1 siRNAs (at 25 nM) individually or in pairwise combinations. Knockdowns targeting a single AP-1 gene were supplemented with non-targeting siRNA to normalize the final siRNA concentration (to 50 nM siRNA) across all siRNA conditions. All siRNAs were tested for knockdown efficiency and specificity by measuring protein levels of each factor and members of the factor subfamily (i.e., measure single-cell protein levels of cFOS, FRA1, and FRA2 following FOS knockdown). Only siRNA species that showed knockdown of the protein target without off-target knockdown effects were used. Cells were fixed 96 hours after transfection with 4% paraformaldehyde in PBS for 30 minutes at room temperature. The siRNA sequences used for each condition are included below (Table 3.1).

Table 3.1 siRNA sequences used for AP-1 gene knockdown

Target Gene	**Dharmacon Cat#**	**siRNA sequence**
Non-targeting control	D-001810-10-05	UGGUUUACAUGUCGACUAA, UGGUUUACAUGUUGUGUGA, UGGUUUACAUGUUUUCUGA, UGGUUUACAUGUUUUCCUA
FOS	J-003265-09	GGGAUAGCCUCUCUUACUA
	J-003265-10	ACAGUUAUCUCCAGAAGAA
	J-003265-12	GCAAUGAGCCUUCCUCUGA
FOSL1	J-004341-06	GAGCUGCAGUGGAUGGUAC
	J-004341-07	AAUCUGGGCUGCAGCGAGA
	J-004341-08	GAGUAAGGCGCGAGCGGAA
FOSL2	J-004110-13	GGCCCAGUGUGCAAGAUUA
cJUN	J-003268-10	GAGCGGACCUUAUGGCUAC
	J-003268-12	GAAACGACCUUCUAUGACG
JUND	J-003900-12	GAAACACCCUUCUACGGCG
	J-003900-13	CCGACGAGCUCACAGUUCC
	J-003900-14	UCAAGAGUCAGAACACGGA
	J-003900-15	GUUCGAUUCUGCCCUAUUU

3.5.3 Iterative indirect immunofluorescence imaging (4i)

4i images were obtained using the protocol described by Gut et. al. [42] with minor modifications. After media aspiration, cells in 96-well plates were fixed with 4% paraformaldehyde in PBS for 30 minutes at room temperature. All washes were performed using a BioTek EL406 Washer Dispenser and consisted of 4 wash cycles of 200 µl with the indicated buffer while retaining approximately 20 µl liquid in each well during the aspiration step to limit cell loss. Cells were washed with PBS then permeabilized for 15 minutes at room temperature with 100 µl 0.5% Triton X-100 in PBS. Cells were washed with PBS followed by Milli-Q deionized water. Cells were next treated 3 times total for 12 minutes each instance with 40 µl elution buffer which consists of 0.5M L-Glycine (Sigma-Aldrich Cat. No. 50046), 3M Urea (Sigma-Aldrich Cat. No. U5128), 3 M Guanidinium chloride (Sigma-Aldrich Cat. No. G3272), and 70 mM TCEP-HCl (Sigma-Aldrich Cat. No. C4706) at pH of 2.5. Cells were washed with PBS as above. Samples were then blocked for 1 h at room temperature with 50 µl blocking buffer which consists of PBS-based Intercept buffer (LiCor Cat. No. 927-70001) supplemented with 150 mM maleimide (Millipore Sigma Cat. No. 129585-25G). Blocking buffer was prepared immediately prior to adding to the samples for each round. Following a PBS wash, samples were incubated overnight at 4°C with 40 µl primary antibody diluted in Intercept buffer. After overnight incubation, cells were washed with PBS then incubated for 1 hour at room temperature in 40 µl secondary antibody solution consisting of the appropriate species-specific Alexa Fluor-conjugated antibodies diluted 1:2000 in Intercept buffer. Cells were then washed with PBS and incubated with 50 µl Hoechst 33342 (Invitrogen Cat. No. H3570) diluted 1:20,000 in PBS. For the first round of imaging, cells were stained with a mixture of Hoechst and CellMask Green (ThermoFisher Cat. No. C37608) for 30 minutes at room temperature according to the manufacturer's instructions. Next, cells were washed with Milli-Q water and 80 µl imaging buffer consisting of 700 mM N-Acetyl-Cysteine (Sigma-Aldrich Cat. No. A7250) at pH of 7.4. Images were obtained using Operetta CLS high content imaging system (Perkin Elmer) using a 10x air objective lens. Following imaging, samples were washed with Milli-Q water after which antibodies were eluted with 3 successive 12-minute incubations at room temperature with elution buffer. Cells were washed with PBS followed by Milli-Q water. Next, 50 µl imaging buffer was added to each well and samples were imaged as above to assess removal of fluorescent signal. Cells were then washed with PBS and all steps were repeated starting at the blocking step for each round of 4i. In instances where the time between 4i rounds exceeded 3 days, following elution, the plates were fixed for 10 minutes at room temperature with 4% paraformaldehyde in PBS. In these cases, to resume staining, cells were then washed with PBS followed by Milli-Q water and treated with elution buffer lacking TCEP-HCl three times for 10 minutes, totaling 30 minutes. Afterwards, cells were washed with PBS and the next round of 4i commenced. The following primary antibodies were used in immunostaining assays (Table 3.2).

Table 3.2 Primary antibodies used in immunostaining assays

Target	**Antibody Name**	**Manufacturer**	**Cat#**
c-FOS	c-Fos (9F6) Rabbit mAb	Cell Signaling Technologies	2250
p-c-FOS	Phospho-c-Fos (Ser32) (D82C12) XP® Rabbit mAb	Cell Signaling Technologies	5348
FRA1	Recombinant Anti-FRA1 [EP4711] Rabbit mAb	Abcam	ab124722
p-FRA1	Phospho-FRA1 (Ser265) (D22B1) Rabbit mAb	Cell Signaling Technologies	5841
FRA2	Fra2 (D2F1E) Rabbit mAb	Cell Signaling Technologies	19967
cJUN	c-Jun (60A8) Rabbit mAb	Cell Signaling Technologies	9165
p-cJUN	Phospho-c-Jun (Ser73) (D47G9) XP® Rabbit mAb	Cell Signaling Technologies	3270
JUND	JunD (D17G2) Rabbit mAb	Cell Signaling Technologies	5000
JUNB	JunB (C37F9) Rabbit mAb	Cell Signaling Technologies	3753
p-ATF1	Phospho Anti-ATF1 (S63) Rabbit mAb	Abcam	ab76085
ATF2	Recombinant Anti-ATF2 [E243]	Abcam	ab32160
p-ATF2	Recombinant Anti-ATF2 (phospho T71) [E268]	Abcam	ab32019
ATF3	Anti ATF3	Abcam	ab87213
ATF4	Recombinant Anti-ATF4 antibody [EPR18111]	Abcam	ab184909
p-ATF4	Anti-ATF4 (phospho S245)	Abcam	ab28830
ATF5	Recombinant Anti-ATF5 [EPR18286]	Abcam	ab184923
ATF6	Anti-ATF6 antibody [1-7]	Abcam	ab122897

p-ERK	Phospho pErk1/2 (T202/Y204) Rabbit mAb	Cell Signaling Technologies	4370
MITF	Human MITF Antibody	R&D Systems	AF5769
SOX10	Anti-SOX10 antibody [SOX10/991]	Abcam	ab212843
NGFR	p75NTR Rabbit mAb	Cell Signaling Technologies	8238
AXL	Human Axl Antibody	R&D Systems	AF154

3.5.4 Image analysis

Images were background subtracted using the rolling ball subtraction algorithm in ImageJ. Background-subtracted images from each round of 4i were aligned using Hoechst nuclei staining with CellProfiler 3.1.9 using the normalized cross correlation method within the Align module. Nuclei were segmented from the aligned images using the Minimum Cross Entropy thresholding method within the IdentifyPrimaryObjects module in CellProfiler. The Threshold smoothing scale and correction factor were 2.4 and 1, respectively with lower and upper threshold bounds of 0 and 1. Cell segmentation was then performed using CellMask Green staining to propagate objects from the nuclei. This was done using the Propagation method within the IdentifySecondaryObjects module. The Minimum cross entropy thresholding method was employed with a smoothing scale of 0 and correction factor of 1, the lower and upper threshold bound values set to 0 and 1, and a regularization factor of 0.05. The TrackObjects module was used to multiplex data from individual rounds of 4i. Within TrackObjects, the Follow Neighbors method was used with the maximum pixel distance of 50 and average cell diameter of 15. Comma-separated text files containing quantitative single-cell measurements of tracked objects from CellProfiler were organized using Matlab. Only objects present in every round of imaging were included in the analysis. Additional data analysis was performed using Matlab, R, and Python.

3.5.5 Classifying melanoma differentiation states

To classify the differentiation state of cells based on image-based protein measurements, we generated histograms of single-cell data on each of the previously validated melanoma differentiation state markers (MITF, SOX10, NGFR and AXL) [12,16]. For each protein (X), we identified an appropriate binary gate, based on which individual melanoma cells were divided into two groups of X^{High} and X^{Low} cells. The gating thresholds used on background-subtracted image data for each protein included: log(MITF) = 7.37, log(SOX10) = 6.82, log(NGFR) = 4.61, and log(AXL) = 5.60. We then used these classifications to determine the differentiation subtype of each individual melanoma cell as follows: melanocytic (M): $MITF^{High}$ /$SOX10^{High}$ /$NGFR^{Low}$ /AXL^{Low}; transitory (T): $MITF^{High}$ /$SOX10^{High}$ /$NGFR^{High}$ /AXL^{Low}; neural crest-like (N): $MITF^{Low}$ /$SOX10^{High}$ /$NGFR^{High}$ /AXL^{High}; and undifferentiated (U): $MITF^{Low}$ /$SOX10^{Low}$ /$NGFR^{Low}$ /AXL^{High}; the single-cell analysis and baseline differentiation state classification were performed across 19 different melanoma cell lines representing a wide spectrum of differentiation states. To classify the differentiation state of cells in gene knockdown perturbation assays, we used a similar approach to distinguish melanocytic/transitory ($MITF^{High}$ /$SOX10^{High}$) cells from undifferentiated ($MITF^{Low}$ /$SOX10^{Low}$) cells.

To classify melanoma differentiation states using bulk transcriptomic data, each melanoma cell line was assigned a series of seven differentiation signature scores, defined as the average of z-scores for the expression levels of differentiation state signature genes identified previously by Tsoi *et al* [12]. These differentiation signatures included the four main differentiation signatures, i.e., melanocytic (M), transitory (T), neural crest-like (N) and undifferentiated (U), as well as mixtures of neighboring signatures, including melanocytic-transitory (MT), transitory-neural crest-like (TN) and neural crest-like-undifferentiated states (NU).

To determine the differentiation state of individual cells for each of the 10 melanoma cell lines profiled by single-cell RNA sequencing by Wouters *et al* [14], we used the R package AUCell to quantify the enrichment of differentiation signature genes (as defined by Tsoi *et al* [12]) in individual cells. Because not all differentiation states were equally represented by the 10 cell lines tested and not all signature genes were available in the expression matrix, we focused our single-cell differentiation state classification on melanocytic, transitory and undifferentiated states by combining two or three closely related signature gene sets as follows: M-MT gene set (combination of M and MT signature genes), MT-T-TN gene set (combination of MT, T and TN signature genes) and NU-U set (combination of NU and U genes). To minimize the impact of noise from single-cell analysis, we then selected cells that represented individual differentiation states based on their gated AUCell scores as follows: melanocytic cells: M-MT^{High}/NU-U^{Low}; transitory cells: MT-T-TN^{High}/NU-U^{Low}; undifferentiated cells: M-MT^{Low}/ MT-T-TN^{Low}/NU-U^{High}. The differentiation state of individual melanoma cells derived from treatment-naïve patient tumors profiled by Tirosh *et al* [43] and Jerby-Arnon *et al* [49] were determined in the same way, except that only melanocytic and undifferentiated cells were identified and analyzed.

3.5.6 Random forest classification

We used random forest classification to test the predictivity of AP-1 variations for melanoma differentiation state using single-cell protein data collected by immunofluorescence imaging of 19 melanoma cell lines. We randomly sampled a total of 10,000 cells, including 2,500 from each of the four differentiation states, in a way that they represented all 19 cell lines and 4 distinctive differentiation states (melanocytic, transitory, neural crest-like and undifferentiated) as equally as possible. By random sampling, we aimed to minimize potential biases associated with genotype differences among cell lines. We used the data from 80% of the sampled cells to train a random forest classification model to predict the differentiation state of each individual cell. We then used the remaining 20% of cells to independently validate model predictions. Model training, cross-validation and independent validation were all performed in Python (3.9.2) using the scikit-learn library (0.24.1) [53]. To standardize the model input, protein levels of each AP-1 measurement were normalized across cells to zero mean and unit variance (z-score scaled) using the StandardScaler() function. The random forest model was trained using the RandomForestClassifier() function. All parameters were as defined in the default settings, except the number of trees in the forest (n_estimators = 100) and maximum tree depth (max_depth = 14), which were separately optimized through 5-fold Stratified Shuffle Split cross-validation on the training set, using the StratifiedShuffleSplit() function with 10 times splitting iterations (n_splits = 10).

The random forest model performance was evaluated based on accuracy and Area Under the Receiver Operating Characteristic Curve (ROC AUC). Accuracy reports the fraction of correctly classified samples, i.e., true positives and true negatives, and it was calculated using the accuracy_score() function. The ROC AUC scores were calculated using the roc_auc_score() function with the One-vs-rest option (multi_class = ‘ovr’), which computes the AUC of each class against the rest. The ROC AUC scores consider both the sensitivity (true positive rate) and specificity (true negative rate) of the model predictions.

To assess the importance of each AP-1 factor in explaining the predictions made by the random forest model for each individual cell in the independent validation set, we used the SHapley Additive exPlanations (SHAP) package [54]. SHAP provides a model agnostic measure of feature importance based on Shapley values, which assign importance of input features based on their contribution to the model output prediction. Mathematically, given a specific prediction output by model *f* with input *x*, Shapley value for feature *i*, $\varphi_i(f,x)$, is the average of feature *i's* marginal contributions across all possible orders of features being included [54,55]:

$$\varphi_i(f, x) = \sum_{S \subseteq S_{all \setminus \{i\}}} \frac{|S|!(M-|S|-1)!}{M!} \left[f_x(S \cup \{i\}) - f_x(S) \right] \qquad \text{(Equation 3.1)}$$

where *M* is the total number of features, |*S*| denotes number of entries in set *S* and the term $f_x(S \cup \{i\}) - f_x(S)$ is the marginal contribution of feature *i*. In SHAP, the marginal impact of a feature is defined as the change in the expected value of the model output *f(x)* when that feature is observed versus unknown:

$$f_x(S \cup \{i\}) - f_x(S) = E\left[f(x) \mid x_{s \cup \{i\}}\right] - E\left[f(x) \mid x_s\right] \qquad \text{(Equation 3.2)}$$

where x_s is a subset of features with only set *S* is observed.

3.5.7 Partial least squares regression (PLSR) modeling

We used PLSR analysis to test whether the relationships between the patterns of AP-1 gene expression and melanoma differentiation state were recapitulated at the transcriptional level. Bulk RNA sequencing data of 53 melanoma cell lines used for PLSR analysis were deposited by Tsoi *et al* [12] in the Gene Expression Omnibus (GEO) database under accession number GSE80829. We first $\log_2$-transformed the gene expression data (reported as FPKM) with an offset of 1. Input vectors for PLSR analysis were then created by combining the z-scored expression data for fifteen AP-1 transcription factor family genes, including FOS, FOSL1, FOSL2, FOSB, JUN, JUNB, JUND, ATF1, ATF2, ATF3, ATF4, ATF5, ATF6, ATF6B and ATF7, across 53 cell lines. The response variables for each cell line were then assembled as a series of seven signature scores, defined as the average of z-scores for the expression levels of differentiation state signature genes [12]. The PLSR model was trained in python using the scikit-learn library and the PLSRegression() function. To evaluate the predictability of the linear relationship between the input and output variables using the same dataset, we used leave-one-out cross-validation by LeaveOneOut() function. To independently validate the model, we used RNA sequencing data from an independent panel of 32 melanoma cell lines in the Cancer Cell Line Encyclopedia (CCLE) [46]. The CCLE data (CCLE_RNAseq_genes_rpkm_20180929.gct data) was downloaded from https://sites.broadinstitute.org/ccle. As with the training dataset, we first $\log_2$-transformed the CCLE gene expression data (reported as RPKM) with an offset of 1. We then created input vectors by combining the z-scored expression data for fifteen AP-1 transcription factor family genes and used them in the optimized PLSR model (using the first four PLS components) trained against the original set of 53 cell lines to predict the differentiation signature scores in the new set of 32 cell lines.

The PLSR model performance was evaluated in terms of fraction of variance explained (R^2) or predicted (Q^2) using the explained_variance_score() function. We assessed the relative importance of each AP-1 factor in the PLSR model based on the variable importance in projection (VIP) scores, computed for the first four PLS components, at which the PLSR model achieves its optimal performance [56]. To help interpret the directionality of the contribution, we multiplied the VIP score for each AP-1 factor by the sign of Pearson correlation coefficient between its expression levels and differentiation signature z-scores.

We compared the performance (based on 10-fold cross validation) of optimized PLSR model, built based on the top eight AP-1 genes (FOS, FOSL1, FOSL2, JUN, JUNB, JUND, ATF2 and ATF4) with optimized models built using combinations of eight randomly chosen basic leucine zipper (bZIP) transcription factors [57] (Table A.1) or eight randomly chosen transcription factors [47] (excluding those that were explicitly involved in the differentiation signature genes) by computing empirical *P* values using 100,000 and 500,000 iterations, respectively.

3.5.8 Uniform manifold approximation and projection (UMAP)

UMAP was performed in R using the umap package. For single-cell protein data, we first performed principal component analysis (PCA) using the prcomp() function on the z-scored log-transformed data and selected the PCA scores from the first four principal component for UMAP analysis. The parameters used in generating the UMAP for single-cell protein data include nearest neighbor (n_neighbors) = 90, minimum distance (min_dist) = 0.7 and distance metric (metric) = Euclidean.

3.5.9 Single-cell regulatory network inference and clustering (SCENIC)

For the SCENIC analysis of melanoma cell lines, the baseline regulon activities inferred by the SCENIC workflow [47,48] were obtained from the .loom file (10_Baselines_filteredRegulons.loom) published by Wouters *et al* [14] (http://scope.aertslab.org/#/Wouters_Human_Melanoma). The .loom file was imported to R for downstream analysis using the SCopeLoomR package.

Single-cell RNA sequencing data for patient-derived melanoma tumors were obtained from previous studies published by Tirosh *et al* [43] and Jerby-Arnon *et al* [49] (GSE72056 and GSE115978). Single-cell gene expression analysis and SCENIC was focused on 2072 malignant melanoma cells, which were distinguished (by the authors) from non-malignant cells based on gene copy number variations We selected 14,689 genes which were detected in more than 1% of the cells (i.e., 20 cells) with at least 103 logged TPM counts. Using this dataset, we then inferred regulons using pySCENIC in a Nextflow pipeline adapted from Wouters *et al* [14] (https://github.com/aertslab/singlecellRNA_melanoma_paper), performing 100 SCENIC runs on the data. As in Wouters *et al*'s regulon filtering criteria, only regulons that had more than 10 target genes and recurred in at least 80/100 runs were retained. Target genes (used in AUCell calculation) that appear in at least 80% of the runs in regulons that recurred 100 times, and all target genes for regulons that recurred 80-100 times were retained. This analysis pipeline resulted in 373 motif regulons.

3.5.10 Partial correlation analysis

Partial correlation analysis is used for the evaluation of correlations between pairs of variables while controlling for the variance explained by a third variable. We used pairwise partial correlation analysis to evaluate correlations among changes induced by MAPK inhibitors in each of the AP-1 protein levels, dedifferentiation, and p-ERK levels across different cell lines, while controlling for the baseline (drug-naïve) variance of differentiation state or AP-1 levels across the same cell lines. To identify possible associations between AP-1 factors and drug-induced dedifferentiation, we first calculated the relative enrichment of dedifferentiated cells at each treatment condition (including the baseline) by subtracting the fraction of cells that are $\text{NGFR}^{\text{Low}}/\text{MITF}^{\text{High}}$ from the fraction of cells that are $\text{NGFR}^{\text{High}}/\text{MITF}^{\text{Low}}$ at that condition. AP-1 data were also averaged across two replicates and log-transformed. We then used the Matlab function partialcorr to evaluate the Pearson's partial correlation coefficients (and the associated *P* values) between the enrichment of dedifferentiated cells and AP-1 data for each MAPK inhibitor treatment condition, while correcting for the variance in the enrichment of dedifferentiated cells at baseline (DMSO condition). Similarly, to assess if any of the AP-1 factors would capture drug-specific changes in ERK signaling, we used partial correlation analysis to determine pairwise correlations between p-ERK and AP-1 levels across drug-treated cell lines, while correcting for differences in their baseline AP-1 levels.

3.5.11 Statistics and reproducibility

No statistical method was used to predetermine sample size. Sample sizes were chosen based on similar studies in the relevant literature. The experiments were not randomized. The investigators were not blinded to allocation during experiments and outcome assessment. All data with error bars were presented as mean values ± s.d. as indicated in figure legends using indicated numbers of replicates. The significance of pairwise correlations were evaluated based on P values associated with the corresponding two-sided Pearson's correlation analysis. To identify the statistical significance of differences between mean of measurements within two different groups *P* values from two-sided *t* test were used. Statistical analyses were performed using MATLAB (2020b), R (4.0.4), Python (3.9.2), Scikit-learn Library (0.24.1). All custom scripts used for data analysis are available on GitHub (https://github.com/fallahi-sichani-lab/AP1-networkPlasticityMelanoma).

References

1. Munsky B, Neuert G, van Oudenaarden A. Using gene expression noise to understand gene regulation. Science. 2012;336: 183–7. doi:10.1126/science.1216379

2. Mitchell S, Hoffmann A. Identifying Noise Sources governing cell-to-cell variability. Curr Opin Syst Biol. 2018;8: 39–45. doi:10.1016/j.coisb.2017.11.013

3. Battich N, Stoeger T, Pelkmans L. Control of Transcript Variability in Single Mammalian Cells. Cell. 2015;163: 1596–610. doi:10.1016/j.cell.2015.11.018

4. Symmons O, Raj A. What's Luck Got to Do with It: Single Cells, Multiple Fates, and Biological Nondeterminism. Mol Cell. 2016;62: 788–802. doi:10.1016/J.MOLCEL.2016.05.023

5. Gupta PB, Fillmore CM, Jiang G, Shapira SD, Tao K, Kuperwasser C, et al. Stochastic state transitions give rise to phenotypic equilibrium in populations of cancer cells. Cell. 2011;146: 633–644. doi:10.1016/j.cell.2011.07.026

6. Arias AM, Hayward P. Filtering transcriptional noise during development: concepts and mechanisms. Nat Rev Genet. 2006;7: 34–44. doi:10.1038/nrg1750

7. Boumahdi S, de Sauvage FJ. The great escape: tumour cell plasticity in resistance to targeted therapy. Nat Rev Drug Discov. 2020;19: 39–56. doi:10.1038/s41573-019-0044-1

8. Sharma SV, Lee DY, Li B, Quinlan MP, Takahashi F, Maheswaran S, et al. A chromatin-mediated reversible drug-tolerant state in cancer cell subpopulations. Cell. 2010;141: 69–80. doi:10.1016/j.cell.2010.02.027

9. Fallahi-Sichani M, Becker V, Izar B, Baker GJ, Lin J, Boswell SA, et al. Adaptive resistance of melanoma cells to RAF inhibition via reversible induction of a slowly dividing de-differentiated state. Mol Syst Biol. 2017;13: 905. doi:10.15252/MSB.20166796

10. Shaffer SM, Dunagin MC, Torborg SR, Torre EA, Emert B, Krepler C, et al. Rare cell variability and drug-induced reprogramming as a mode of cancer drug resistance. Nature. 2017;546: 431–435. doi:10.1038/nature22794

11. Emert BL, Cote CJ, Torre EA, Dardani IP, Jiang CL, Jain N, et al. Variability within rare cell states enables multiple paths toward drug resistance. Nat Biotechnol. 2021;39: 865–876. doi:10.1038/s41587-021-00837-3

12. Tsoi J, Robert L, Paraiso K, Galvan C, Sheu KM, Lay J, et al. Multi-stage Differentiation Defines Melanoma Subtypes with Differential Vulnerability to Drug-Induced Iron-Dependent Oxidative Stress. Cancer Cell. 2018;33: 890-904.e5. doi:10.1016/j.ccell.2018.03.017

13. Rambow F, Rogiers A, Marin-Bejar O, Aibar S, Femel J, Dewaele M, et al. Toward Minimal Residual Disease-Directed Therapy in Melanoma. Cell. 2018;174: 843-855.e19. doi:10.1016/j.cell.2018.06.025

14. Wouters J, Kalender-Atak Z, Minnoye L, Spanier KI, De Waegeneer M, Bravo González-Blas C, et al. Robust gene expression programs underlie recurrent cell states and phenotype switching in melanoma. Nat Cell Biol. 2020;22: 986–998. doi:10.1038/s41556-020-0547-3

15. Baron M, Tagore M, Hunter MV, Kim IS, Moncada R, Yan Y, et al. The Stress-Like Cancer Cell State Is a Consistent Component of Tumorigenesis. Cell Syst. 2020;11: 536-546.e7. doi:10.1016/j.cels.2020.08.018

16. Khaliq M, Manikkam M, Martinez ED, Fallahi-Sichani M. Epigenetic modulation reveals differentiation state specificity of oncogene addiction. Nat Commun. 2021;12: 1536. doi:10.1038/s41467-021-21784-2

17. Belote RL, Le D, Maynard A, Lang UE, Sinclair A, Lohman BK, et al. Human melanocyte development and melanoma dedifferentiation at single-cell resolution. Nat Cell Biol. 2021;23: 1035–1047. doi:10.1038/s41556-021-00740-8

18. Lin JY, Fisher DE. Melanocyte biology and skin pigmentation. Nature. 2007;445: 843–850. doi:10.1038/nature05660

19. Mica Y, Lee G, Chambers SM, Tomishima MJ, Studer L. Modeling neural crest induction, melanocyte specification, and disease-related pigmentation defects in hESCs and patient-specific iPSCs. Cell Rep. 2013;3: 1140–1152. doi:10.1016/j.celrep.2013.03.025

20. Konieczkowski DJ, Johannessen CM, Abudayyeh O, Kim JW, Cooper ZA, Piris A, et al. A Melanoma Cell State Distinction Influences Sensitivity to MAPK Pathway Inhibitors. Cancer Discov. 2014;4: 816–827. doi:10.1158/2159-8290.CD-13-0424

21. Müller J, Krijgsman O, Tsoi J, Robert L, Hugo W, Song C, et al. Low MITF/AXL ratio predicts early resistance to multiple targeted drugs in melanoma. Nat Commun. 2014;5: 5712. doi:10.1038/ncomms6712

22. Marin-Bejar O, Rogiers A, Dewaele M, Femel J, Karras P, Pozniak J, et al. Evolutionary predictability of genetic versus nongenetic resistance to anticancer drugs in melanoma. Cancer Cell. 2021;39: 1135-1149.e8. doi:10.1016/j.ccell.2021.05.015

23. Lito P, Pratilas CA, Joseph EW, Tadi M, Halilovic E, Zubrowski M, et al. Relief of profound feedback inhibition of mitogenic signaling by RAF inhibitors attenuates their activity in BRAFV600E melanomas. Cancer Cell. 2012;22: 668–682. doi:10.1016/j.ccr.2012.10.009

24. Gerosa L, Chidley C, Fröhlich F, Sanchez G, Lim SK, Muhlich J, et al. Receptor-Driven ERK Pulses Reconfigure MAPK Signaling and Enable Persistence of Drug-Adapted BRAF-Mutant Melanoma Cells. Cell Syst. 2020;11: 478-494.e9. doi:10.1016/j.cels.2020.10.002

25. Pedraza JM, van Oudenaarden A. Noise Propagation in Gene Networks. Science. 2005;307: 1965–1969. doi:10.1126/science.1109090

26. Huang S. Non-genetic heterogeneity of cells in development: More than just noise. Development. 2009;136: 3853–3862. doi:10.1242/dev.035139

27. Karin M. The Regulation of AP-1 Activity by Mitogen-activated Protein Kinases *. J Biol Chem. 1995;270: 16483–16486. doi:10.1074/jbc.270.28.16483

28. Vierbuchen T, Ling E, Cowley CJ, Couch CH, Wang X, Harmin DA, et al. AP-1 Transcription Factors and the BAF Complex Mediate Signal-Dependent Enhancer Selection. Mol Cell. 2017;68: 1067-1082.e12. doi:10.1016/j.molcel.2017.11.026

29. Martínez-Zamudio RI, Roux P-F, de Freitas JANLF, Robinson L, Doré G, Sun B, et al. AP-1 imprints a reversible transcriptional programme of senescent cells. Nat Cell Biol. 2020;22: 842–855. doi:10.1038/s41556-020-0529-5

30. Phanstiel DH, Van Bortle K, Spacek D, Hess GT, Shamim MS, Machol I, et al. Static and Dynamic DNA Loops form AP-1-Bound Activation Hubs during Macrophage Development. Mol Cell. 2017;67: 1037-1048.e6. doi:10.1016/j.molcel.2017.08.006

31. Madrigal P, Alasoo K. AP-1 Takes Centre Stage in Enhancer Chromatin Dynamics. Trends Cell Biol. 2018;28: 509–511. doi:10.1016/j.tcb.2018.04.009

32. Fallahi-Sichani M, Moerke NJ, Niepel M, Zhang T, Gray NS, Sorger PK. Systematic analysis of BRAFV600E melanomas reveals a role for JNK/c-Jun pathway in adaptive resistance to drug-induced apoptosis. Mol Syst Biol. 2015;11: 797–797. doi:10.15252/msb.20145877

33. Haas L, Elewaut A, Gerard CL, Umkehrer C, Leiendecker L, Pedersen M, et al. Acquired resistance to anti-MAPK targeted therapy confers an immune-evasive tumor microenvironment and cross-resistance to immunotherapy in melanoma. Nat Cancer. 2021;2: 693–708. doi:10.1038/s43018-021-00221-9

34. Emmons MF, Faião-Flores F, Sharma R, Thapa R, Messina JL, Becker JC, et al. HDAC8 Regulates a Stress Response Pathway in Melanoma to Mediate Escape from BRAF Inhibitor Therapy. Cancer Res. 2019;79: 2947–2961. doi:10.1158/0008-5472.CAN-19-0040

35. Ramsdale R, Jorissen RN, Li FZ, Al-Obaidi S, Ward T, Sheppard KE, et al. The transcription cofactor c-JUN mediates phenotype switching and BRAF inhibitor resistance in melanoma. Sci Signal. 2015;8: ra82. doi:10.1126/scisignal.aab1111

36. Maurus K, Hufnagel A, Geiger F, Graf S, Berking C, Heinemann A, et al. The AP-1 transcription factor FOSL1 causes melanocyte reprogramming and transformation. Oncogene. 2017;36: 5110–5121. doi:10.1038/onc.2017.135

37. Torre EA, Arai E, Bayatpour S, Jiang CL, Beck LE, Emert BL, et al. Genetic screening for single-cell variability modulators driving therapy resistance. Nat Genet. 2021;53: 76–85. doi:10.1038/s41588-020-00749-z

38. Kong X, Kuilman T, Shahrabi A, Boshuizen J, Kemper K, Song J-Y, et al. Cancer drug addiction is relayed by an ERK2-dependent phenotype switch. Nature. 2017;550: 270–274. doi:10.1038/nature24037

39. Riesenberg S, Groetchen A, Siddaway R, Bald T, Reinhardt J, Smorra D, et al. MITF and c-Jun antagonism interconnects melanoma dedifferentiation with pro-inflammatory cytokine responsiveness and myeloid cell recruitment. Nat Commun. 2015;6: 8755. doi:10.1038/ncomms9755

40. Johannessen CM, Johnson LA, Piccioni F, Townes A, Frederick DT, Donahue MK, et al. A melanocyte lineage program confers resistance to MAP kinase pathway inhibition. Nature. 2013;504: 138–142. doi:10.1038/nature12688

41. Rodríguez-Martínez JA, Reinke AW, Bhimsaria D, Keating AE, Ansari AZ. Combinatorial bZIP dimers display complex DNA-binding specificity landscapes. eLife. 2017;6. doi:10.7554/eLife.19272

42. Gut G, Herrmann MD, Pelkmans L. Multiplexed protein maps link subcellular organization to cellular states. Science. 2018;361: eaar7042. doi:10.1126/science.aar7042

43. Tirosh I, Izar B, Prakadan SM, Wadsworth MH, Treacy D, Trombetta JJ, et al. Dissecting the multicellular ecosystem of metastatic melanoma by single-cell RNA-seq. Science. 2016;352: 189–96. doi:10.1126/science.aad0501

44. Lundberg SM, Erion G, Chen H, DeGrave A, Prutkin JM, Nair B, et al. From local explanations to global understanding with explainable AI for trees. Nat Mach Intell. 2020;2: 56–67. doi:10.1038/s42256-019-0138-9

45. Becht E, McInnes L, Healy J, Dutertre C-A, Kwok IWH, Ng LG, et al. Dimensionality reduction for visualizing single-cell data using UMAP. Nat Biotechnol. 2018. doi:10.1038/nbt.4314

46. Ghandi M, Huang FW, Jané-Valbuena J, Kryukov GV, Lo CC, McDonald ER, et al. Next-generation characterization of the Cancer Cell Line Encyclopedia. Nature. 2019;569: 503–508. doi:10.1038/s41586-019-1186-3

47. Van de Sande B, Flerin C, Davie K, De Waegeneer M, Hulselmans G, Aibar S, et al. A scalable SCENIC workflow for single-cell gene regulatory network analysis. Nat Protoc. 2020;15: 2247–2276. doi:10.1038/s41596-020-0336-2

48. Aibar S, González-Blas CB, Moerman T, Huynh-Thu VA, Imrichova H, Hulselmans G, et al. SCENIC: single-cell regulatory network inference and clustering. Nat Methods. 2017;14: 1083–1086. doi:10.1038/nmeth.4463

49. Jerby-Arnon L, Shah P, Cuoco MS, Rodman C, Su M-J, Melms JC, et al. A Cancer Cell Program Promotes T Cell Exclusion and Resistance to Checkpoint Blockade. Cell. 2018;175: 984-997.e24. doi:10.1016/j.cell.2018.09.006

50. Gillies TE, Pargett M, Minguet M, Davies AE, Albeck JG. Linear Integration of ERK Activity Predominates over Persistence Detection in Fra-1 Regulation. Cell Syst. 2017;5: 549-563.e5. doi:10.1016/j.cels.2017.10.019

51. Lopez-Bergami P, Lau E, Ronai Z. Emerging roles of ATF2 and the dynamic AP1 network in cancer. Nat Rev Cancer. 2010;10: 65–76. doi:10.1038/nrc2681

52. Davies AE, Pargett M, Siebert S, Gillies TE, Choi Y, Tobin SJ, et al. Systems-Level Properties of EGFR-RAS-ERK Signaling Amplify Local Signals to Generate Dynamic Gene Expression Heterogeneity. Cell Syst. 2020;11: 161-175.e5. doi:10.1016/j.cels.2020.07.004

53. Pedregosa F, Varoquaux G, Gramfort A, Michel V, Thirion B, Grisel O, et al. Scikit-learn: Machine Learning in Python. Mach Learn PYTHON. : 6.

54. Lundberg SM, Lee S-I. A Unified Approach to Interpreting Model Predictions. Advances in Neural Information Processing Systems. Curran Associates, Inc.; 2017. Available: https://papers.nips.cc/paper/2017/hash/8a20a8621978632d76c43dfd28b67767-Abstract.html

55. Lundberg SM, Nair B, Vavilala MS, Horibe M, Eisses MJ, Adams T, et al. Explainable machine-learning predictions for the prevention of hypoxaemia during surgery. Nat Biomed Eng. 2018;2: 749–760. doi:10.1038/s41551-018-0304-0

56. Wold S. Exponentially weighted moving principal components analysis and projections to latent structures. Chemom Intell Lab Syst. 1994;23: 149–161.

57. Vinson C, Myakishev M, Acharya A, Mir AA, Moll JR, Bonovich M. Classification of Human B-ZIP Proteins Based on Dimerization Properties. Mol Cell Biol. 2002;22: 6321–6335. doi:10.1128/MCB.22.18.6321-6335.2002

Chapter 4 Conclusions and Future Directions

4.1 Summary

Resistance due to tumor cell heterogeneity is a fundamental challenge that faces the discovery and use of targeted therapies for cancer treatment. Patient responses to cancer drugs vary significantly in the extent and duration. Moreover, many patients eventually develop drug resistance despite their substantial initial responses to treatment. Understanding the molecular basis for such variations in treatment response is key to the development of better cancer therapies. Most of our current systematic approaches to understand variations in anticancer drug response rely on correlating drug responses to genomic profiles across tumor populations. Such genome-wide interrogations have already led to discoveries of targeted therapies tailored to patients with specific genomic signatures and significantly refined our understanding of the disease. However, emerging evidence has revealed that a considerable amount of non-determinism in tumor cell drug response may be traced back to non-genetic heterogeneity.

Advances in single-cell biology in the past two decades let us appreciate the numerous ways in which cells are different from one another. Non-genetic sources of molecular fluctuations diversify phenotypic responses of cells to drugs at the single-cell level. Such molecular fluctuations can prime a fraction of tumor cells to be intrinsically drug-tolerant or render them phenotypic plasticity to adapt to drug-induced stress. Such single-cell variability has profound clinical impact on tumor responses to targeted therapies. In fact, resistance of a rare subpopulation of tumor cells to therapy may be sufficient for tumors to relapse in patients after a transient period of good response. These rare drug-tolerant subpopulations diminish therapeutic efficacy, yet they are often masked by population-based measurements in most standard pre-clinical assays. Furthermore, there is a major gap in our understanding of the precise biochemical mechanisms that determine cellular plasticity and the variability in responses of cells to drugs that target specific oncogenic pathways.

The goal of this work is to address the current gaps in quantifying cell-to-cell variability in drug response and identifying intrinsic and adaptive mechanisms that lead to cell-to-cell heterogeneity in drug response. To this end, we developed a systems pharmacological framework to evaluate time-dependent drug responses based on probabilistic metrics that quantify drug-induced tumor cell killing and inhibition of division at the single-cell level. We revealed the time-varying impact of rare drug-tolerant cells in the assessment of drug response and combination interactions. We have also studied the origins of intrinsic diversity of phenotypic states and adaptive responses in melanoma cells by systematically interrogating the AP-1 transcription factor network. Our systems biology approach integrates data-driven modeling with multiplexed measurements capturing tumor cell heterogeneity at transcriptional and protein levels. This system-wide investigation uncovered previously unknown interdependencies among AP-1 factors and their associations with diverse patterns of cellular plasticity. Collectively, these studies are critical for designing therapeutic strategies at cellular precision, which is necessary to overcome fractional killing due to phenotypic heterogeneity and plasticity.

In this final chapter, I will briefly summarize the key findings from each aim of my PhD thesis proposal. I will then make suggestions for future studies based on these findings. In particular, I will focus on discussing the exciting next steps that we can take to elucidate the mechanisms that link transcriptional and epigenetic plasticity, heterogeneity in the state of oncogenic MAPK signaling, and the phenotypic diversity of MAPK inhibitor responses in melanoma cells.

4.2 Key findings by aim

4.2.1 Aim 1

We used basic probability theory, computer simulations, time-lapse live cell microscopy, and single-cell analysis to show that fraction of cells affected (f_a) metrics derived from conventional dose-response curves may bias our assessment of drug efficacy and combination effectiveness. This bias may be corrected when dynamic probabilities of drug-induced phenotypic events, i.e. induction of cell death and inhibition of division, at a single-cell level are used as metrics to assess drug efficacy. Probabilistic phenotype metrics offer the following three benefits. First, in contrast to the commonly used f_a metrics, they directly represent probabilities of drug action in a cell population. Therefore, they deconvolve differential degrees of drug effect on tumor cell killing versus inhibition of cell division, which may not be correlated for many drugs. Second, they increase the sensitivity of short-term drug response assays to cell-to-cell heterogeneities and the presence of drug-tolerant subpopulations. Third, their probabilistic nature allows them to be used directly in unbiased evaluation of synergistic efficacy in drug combinations using probabilistic models such as Bliss independence. Altogether, we envision that probabilistic analysis of single-cell phenotypes complements currently available assays via improving our understanding of heterogeneity in drug response, thereby facilitating the discovery of more efficacious combination therapies to block drug-tolerant cells.

4.2.2 Aim2

We tested the hypothesis that the intrinsic diversity of phenotypic states (i.e., differentiation states) and adaptive responses to MAPK inhibitors in BRAF-mutated melanoma cells can be traced back to a common set of molecular determinants. To test this hypothesis, we focused on the AP-1 transcription factor family, since they are major MAP kinase targets linking signaling to transcription, and that they have been implicated in previous studies for their roles in MAPK inhibitor resistance and differentiation. To systematically interrogate AP-1 contributions in BRAF-mutant melanoma plasticity, we combined multiplexed measurements of AP-1 state, MAPK signaling activity and differentiation state at population and single-cell levels, across genetically diverse melanoma cell lines before and after BRAF/MEK inhibitor exposure. Using multivariate statistically learning and single-cell regulatory network inference, we identified patterns of a subset of AP-1 factors that are highly predictive of phenotypic heterogeneity in melanoma cultures and patient-derived tumors. We validated the causality of these statistical predictions with RNAi-mediated knockdown experiments followed by single-cell analysis. We found that a tightly interdependent balance among AP-1 factors cJUN, FRA2, FRA1 and cFOS determines the intrinsic diversity of differentiation states of melanoma cells. Such balance is perturbed by MAPK pathway inhibition. We found that MAPK inhibitors induce changes in the AP-1 state, including the abundance of cJUN and its phosphorylation, as well as the phosphorylation state of FRA1, which are strong predictors of drug-induced dedifferentiation and adaptive MAPK pathway reactivation, respectively. Altogether, these results show that the state of AP-1 transcription factor network offers critical molecular context for the intrinsic and drug-adaptive response to MAPK pathway perturbation in melanoma, unifying these seemingly distinct forms of heterogeneity. Thus, AP-1 may serve as a critical node for manipulating cellular plasticity with potential therapeutic implications.

4.3 Future Directions

Molecular differences at the single-cell level can generate remarkably distinct phenotypic responses to drug treatment. Overcoming therapeutic resistance therefore requires uncovering the hidden molecular variables that explain the seemingly probabilistic mapping between oncogenic signaling and phenotypic outcomes at the single-cell level [1]. Most recent efforts have been focused on characterizing the intrinsic cell-to-cell variability (revealing e.g., differences in the abundance of receptor tyrosine kinases, epigenetic modifiers, and transcription factors) that may lead to resistant phenotypes [2–5]. However, mechanisms of cell-fate control, i.e., *how* variable phenotypic outcomes emerge in the context of specific signaling perturbations, remain unclear in most cases. Such mechanistic understanding is key to overcoming tumor-cell heterogeneity in therapeutic response, since phenotypic states that emerge in response to external cues may exhibit a rich diversity of cellular states rather than binary outcomes (e.g., resistant or sensitive) [6]. These cellular states can also vary depending on the external cue and molecular context. Therefore, future effort should shift towards gaining a systems and mechanistic understanding of cell-to-cell molecular differences as a network rather than as individual biomarkers and investigating how such network interprets oncogenic signaling perturbations differently from one cell to the next. Focusing on the deregulated MAPK signaling in melanoma, here I will discuss two future directions that aim at mechanistically elucidating the epigenetic and transcriptional mapping between MAPK signaling and phenotypic outcomes (differentiation states) in melanoma (Figure 4.1).

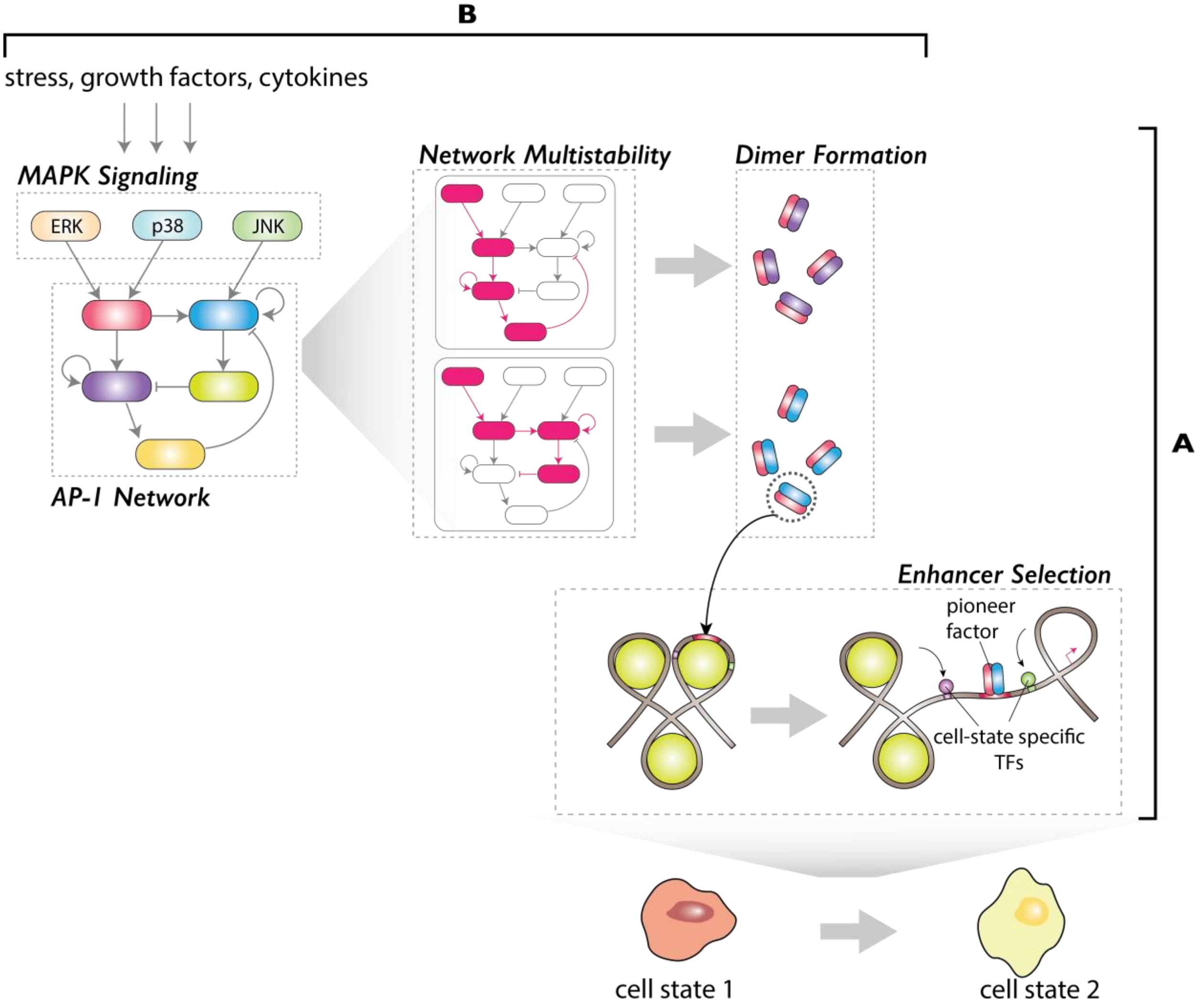

Figure 4.1 Future directions to elucidate the epigenetic and transcriptional mapping underlying MAPK-dependent cellular plasticity in melanoma

Intrinsic regulation of the MAPK-AP-1 network interactions may preferentially lead to formation of different AP-1 dimers, which in turn could select for different enhancer landscapes that ultimately lead to distinct cellular states. For future directions, identifying the variable states of the MAPK-AP-1 network and elucidating the epigenetic and transcriptional roles of different AP-1 dimers in cellular plasticity may reveal the hidden molecular mapping between MAPK signaling and phenotypic states.

4.3.1 Decipher the transcription-factor code for signal-dependent enhancer selection underlying tumor cell heterogeneity and drug-induced plasticity

Cell-fate decision and cell-state maintenance require cells to selectively read genetic regulatory information within the genome. Differences in the epigenetic landscape generate variability in such selective reading, thereby establishing diverse states of drug tolerance in tumor cells in the absence of genetic variability. In melanoma, numerous recent studies have linked heterogeneity in the state of MAPK signaling dependency to epigenetic differences, which result in a mixture of differentiation states at varying frequencies within genetically homogeneous cell populations [3,7–11]. Furthermore, remodeling of the epigenetic landscape enables cellular plasticity, through which cells can adapt to environmental perturbations such as drug treatment. For example, therapeutic inhibition of MAPK signaling in melanoma results in cell-state switching to a transiently drug-tolerant phenotype with an altered differentiation state [2,12]. However, the dynamic epigenetic mechanisms and regulatory networks that drive these distinct epigenetic states and their connection to oncogenic MAPK signaling remain poorly understood, leaving potential therapeutic strategies to manipulate cell state plasticity largely unrealized.

Enhancers are important regulatory elements that encode the instructions to execute cell-state specific gene expression programs. Such programs are encoded by the composition of transcription factor binding motifs within an enhancer [13]. Transcription factor binding to enhancers depends on chromatin accessibility of the epigenetic landscape. A subset of transcription factors, also known as pioneer factors, can bind cooperatively to nucleosomal enhancers, evicting nucleosomes and rendering enhancer accessibility for other non-pioneer transcription factors [14,15]. Importantly, cell-state specific responses to external stimuli are often specified by an enhancer landscape that is already primed by pioneer factors prior to signal-dependent activation [16–18]. Changes in transcription factor expression and/or activity, therefore, can influence not only gene regulation, but also enhancer selection for cell-state establishment and future cell-fate in response to stimuli. Identifying transcription factors that pioneer variable enhancer landscapes underpinning tumor cell state plasticity will provide a key to modulate tumor heterogeneity. It will also open up opportunities to link the global epigenetic landscape to upstream signaling that acts through these transcription factors.

In Chapter 3, we discovered that differentiation state heterogeneity and cellular plasticity in melanoma are associated with distinct states of the AP-1 transcription factor network. Moreover, recent studies have reported that AP-1 proteins pioneer the enhancer landscape to regulate specific gene expression programs [15,16,19,20]. As downstream effectors of the MAPK pathway and pioneer factors, the AP-1 family serves as an intriguing node for elucidating the mapping between oncogenic signaling and melanoma cell states. Furthermore, AP-1 dimers differ in their enhancer binding affinities and specificities depending on their compositions [21]. Therefore, different AP-1 dimer compositions, which likely select for different enhancer landscapes, could encode distinct cellular states. For future studies, I propose to investigate how enhancer landscapes are shaped by different AP-1 combinations across melanoma differentiation states and in response to MAPK inhibition (Figure 4.1 A). This investigation will uncover the transcription factor regulation principles of the enhancer landscapes that drive melanoma heterogeneity associated with both intrinsic and adaptive resistance to MAPK inhibitors. This goal may be accomplished using the following approaches:

1) Identify AP-1 dimer compositions associated with enhancer selection across heterogeneous melanoma cell populations

In Chapter 3, we determined that a regulated balance among specific AP-1 factors determines distinct differentiation states in melanoma. Based on these studies and the evidence from literature, I hypothesize that different AP-1 dimer compositions select distinct enhancer landscapes that establish melanoma differentiation states. To test this hypothesis, I propose to perform molecular profiling on melanocytic and undifferentiated cell subpopulations within a heterogeneous cell line (e.g., COLO858) sorted based on cell surface markers for these differentiation states. Enhancer landscape and AP-1 binding activity can be determined based on genome-wide profiling using CUT&RUN [22] for histone modifications H3K4me1 and H3K27ac, and AP-1 factors cFOS, FRA2, cJUN and ATF4. These AP-1 factors are chosen because they are associated with heterogeneity in differentiation state within the COLO858 cell line. Overlapping the genomic coordinates of the CUT&RUN signals for these markers in each cell subpopulation will reveal the AP-1 bound enhancers, enhancer state (active versus poised) and AP-1 binding compositions at these enhancers. I expect that comparing the enhancer landscapes between the melanocytic and undifferentiated subpopulations will suggest whether and which potential AP-1 bound enhancers are associated with the non-genetic heterogeneity in differentiation state. Motif enrichment analyses [23] on the enhancer regions of interest can also suggest binding of potential co-factors or other AP-1 members.

Building upon the findings from the study proposed above, I would also suggest a systematic study to interrogate the role of AP-1 combinations in shaping the enhancer landscape associated with differentiation state heterogeneity at the single-cell level. I propose simultaneous profiling of genome-wide chromatin accessibility and transcriptome at the single-cell level across a panel of melanoma cell lines using SHARE-Seq [24]. SHARE-Seq uniquely and simultaneously labels mRNA and chromatin fragments in the same cell with barcoded oligonucleotides, thereby allowing high-throughput joint profiling of chromatin accessibility and gene expression at the single-cell level. The selection of cell lines should be genetically diverse and covers a wide spectrum of melanoma differentiation state in order to avoid discoveries that may be biased to a particular cell line. Leveraging the single-cell resolution of the resulting dataset, computational strategies can be used to infer cis-regulatory interactions. In particular, chromatin regions containing high densities of gene interactions are likely super-enhancers that may serve as regulatory hubs for lineage-determining genes. To systematically identify the enhancer landscape associated with changes in melanoma differentiation, pseudo-temporal ordering [25,26] of cells based on differentiation signature gene expressions and/or cis-regulatory topics [27] (inferred from chromatin accessibility) can be used to resolve the differentiation trajectory. Using this pseudo-time trajectory, we can then determine changes in chromatin accessibility that may prime cells for lineage commitment. During lineage commitment, changes in these priming chromatin regions along the trajectory are expected to precede expression of differentiation programs [24]. Motif enrichment analysis of these key regions should reveal whether AP-1 members bind to those regions and possibly provide some information about their dimer or co-factor compositions. Furthermore, examining the pseudo-time dynamics for specific gene expressions and transcription factor motif activities (inferred from chromatin accessibility) can reveal the potential mechanisms governing the primed chromatin states based on the ordering of events [24]. Finally, to validate the findings, I propose using CRISPR interference [28] to disrupt the AP-1 dimer or co-factor binding sites (individually and in combinations) at the enhancer of interest, followed by CUT&RUN to measure components of the AP-1 dimer complex from the sorted melanocytic and undifferentiated cell subpopulations. This experiment should validate the functionality of the enhancer for maintaining certain differentiation states, and whether their function requires binding of both factors or just one of the factors.

2) Uncover MAPK inhibitor-induced changes in enhancer selection and the associated AP-1 dimer compositions

Perturbation of the MAPK signaling pathway can influence the concentrations, activities, and dimer composition of the AP-1 transcription factors. Accordingly, in Chapter 3, we showed that inhibiting MAPK signals with drugs in melanoma results in changes in certain AP-1 protein and phosphoprotein concentrations. These changes in AP-1 state are associated with drug-induced dedifferentiation and ERK signaling changes, both of which are known mechanisms connected to adaptive resistance in melanoma [12,29]. Based on such knowledge, I hypothesize that cellular plasticity induced by MAPK inhibition is mediated by specific AP-1 combinations altering the enhancer landscape. To test this hypothesis, I propose using SHARE-seq to profile chromatin accessibility and gene expression at the single-cell level in COLO858 cells at 48 h and 96 h upon different drug-treatment conditions. These treatment conditions include the untreated control, BRAF inhibitor vemurafenib alone and BRAF inhibitor in combination with MEK inhibitor trametinib at three different doses. Applying trajectory inference techniques on the SHARE-seq data as described above will uncover the pseudo-dose trajectories of COLO858 following MAPK inhibition. Based on similar preliminary results of inferred trajectories from the 4i single-cell protein data under the same proposed experimental conditions, I anticipate that this pseudo-dose analysis will result in two distinct, continuous trajectories between BRAF inhibitor treatment and BRAF/MEK inhibitor combination treatment. Based on these trajectories, we can determine which chromatin regulatory hubs become accessible upon MAPK inhibition and whether these chromatin regions are connected to known adaptive signaling pathways. We can also determine whether there are primed chromatin states that may distinguish MAPK inhibitor treatment conditions. Finally, examining these regulatory regions of interest using motif enrichment analysis, we can uncover whether and which AP-1 dimers or co-factors are potential regulators for the activities of these regulatory regions. A similar CRISPR interference approach described in the previous section can be used to validate these findings.

Altogether, following these directions will elucidate the mechanistic link between AP-1, a key MAPK-signaling dependent transcription factor node, and the enhancer landscapes underlying the intrinsic heterogeneity and drug-induced plasticity in melanoma. Uncovering regulators for enhancer selection will also inform potential therapeutic strategies for manipulating tumor cell state heterogeneity and plasticity.

4.3.2 Linking the state of MAPK signaling to phenotypic heterogeneity through modeling of the AP-1 network

Cellular responses to external cues depend on the molecular context. In the case of melanoma, inhibition of the hyperactivated MAPK signaling often generates variable responses that are associated with differentiation state plasticity and heterogeneity [2,12]. The mechanisms of how perturbing MAPK signals engenders such heterogeneity remain unclear. Conversely, it is also not well-understood as to why melanoma cells of distinct differentiation states tolerate MAPK inhibition differently (e.g., incomplete inhibition versus reduced dependency on MAPK signaling) [7]. Resolving such mapping between signaling and cell-fate decisions is fundamental to precision medicine and is key for implementing targeted therapies at cellular precision.

As a major target of the MAPK signaling cascade, the AP-1 transcription factor family is activated in response to a wide range of extracellular signals [30]. AP-1 factors play a critical role in the transcriptional regulation of many cellular processes, ranging from stress response and apoptosis to differentiation and proliferation [15,16,20,31,32]. In malignancy, dysregulation of different AP-1 factors has been linked to tumorigenesis, metastasis, and drug resistance

[12,31,33–36]. The crucial role of AP-1 in transcriptional regulation in response to extracellular stimuli places AP-1 at a functional epicenter that bridges upstream signals, transcription, and phenotypic outcomes [31]. Indeed, our study in Chapter 3, among others, has illuminated the possibility that the state of the AP-1 network provides important signaling context for distinct cell-fate decisions [15,30,37,38]. However, the detailed mechanistic interactions among AP-1 members and MAP kinases, and how such interactions influence cellular outcomes remain elusive. Elucidating these interactions as a network will open up new avenues for interrogating the connection between MAPK signaling and cell-fate decisions.

Our investigation in Chapter 3 was primarily focused on AP-1 function in terms of individual factors. Nevertheless, much of the upstream MAPK signaling information is likely interpreted by AP-1 as an interconnected network. In particular, while AP-1 transcription, activity and degradation are regulated by MAP kinases [15,39–41], crosstalk among AP-1 complexes and autoregulation can also influence AP-1 transcription and stability [31,42–46]. Furthermore, the diverse repertoire of transcriptional responses elicited by AP-1 is orchestrated by their expansive combinatorial arrays of homodimeric or heterodimeric complexes [34,37,42,47–49]. Such compositional diversity may explain why individual AP-1 members are often linked to contradictory functions in different contexts. JUN, for example, is associated with pro-apoptotic or anti-apoptotic functions, depending on the dimeric composition induced under different biochemical contexts [50,51].

Focusing on melanoma as a paradigm for understanding the connection between phenotypic heterogeneity and fluctuations in oncogenic signaling, I propose to elucidate the interactions within the AP-1 network in order to understand how such network encodes MAPK signals and directs distinct differentiation states in melanoma (Figure 4.1 B). I envision this investigation will uncover a previously hidden molecular mapping that links oncogenic signaling to phenotypic outcomes on the basis of the state of AP-1 network. Such knowledge can provide a roadmap for predicting and manipulating the state of oncogene dependency. This goal may be accomplished using the following approaches:

1) Elucidate the logic of the AP-1 network governing differentiation state heterogeneity in melanoma

AP-1 factors function in unison as a network to execute specific transcriptional programs. In Chapter 3, we showed that perturbation of certain AP-1 factors can influence the levels of other AP-1 factors. This is consistent with many reports showing the tightly regulated interactions among AP-1 factors [31,32,34]. Such interactions can be mediated by dimerization directly impacting the transcription and stability of one another, or indirectly through other downstream/upstream factors including MAP kinases [31,43,45,46,52]. From a systems perspective, these interactions comprise various network motifs (e.g., autoregulation, feedback, feedforward loops) that control the stability and dynamics of the state of the AP-1 network. Ultimately, tipping the balance of AP-1 interactions could impact the cellular states and responses regulated by the AP-1 network.

While many pairwise interactions among certain AP-1 members have been reported, there has not been a systematic study of AP-1 behaviors as a network, especially in the context of its regulation of melanoma differentiation state. For future directions, I propose combining single-cell measurements and mathematical modeling to elucidate the interactions among several key AP-1 factors identified in Chapter 3 and to understand the underlying network behaviors that drive melanoma differentiation state heterogeneity. To generate the data for network inference, I propose siRNA perturbation experiments as described in Chapter 3 to deplete key AP-1 factors (cFOS, FRA1, FRA2, cJUN, JUND) individually and in pairwise combinations in a cell line (e.g., COLO858) consisting of heterogeneous AP-1 state and differentiation state. Using 4i [53], we can then acquire multiplexed measurements of these five AP-1 factors, their phosphorylated states and differentiation state markers for each condition. Using this data, I suggest to first use data-driven techniques to generate a Boolean model describing the logic of the AP-1 network [54]. In a Boolean model, dependencies among nodes (i.e., molecular players in the signaling network) are specified by logic gates, which are described in terms of Boolean logic operators such as “AND”, “OR”, and “NOT”. Logic-based modeling is an attractive approach for our goal since it allows us to describe the dynamics of a system without explicitly modeling the detailed biochemical interactions which requires significantly higher numbers of parameters and higher amounts of prior knowledge [54,55]. In this case, literature reports on the detailed biochemical interactions remain largely disparate and likely depend on the biological context.

To infer an AP-1 Boolean network that explains melanoma differentiation state heterogeneity, I suggest to first train a Boolean model against the data from the control and individual knockdown conditions using CellNetOpt [54,56]. The training data will consist of the population-averaged AP-1 measurements from each differentiation state (classified as melanocytic or undifferentiated based on differentiation markers) across different experimental conditions. The *a priori* network used as input for CellNetOpt can be obtained by information theoretic analysis (e.g. DREMI [57,58]) that quantifies the directionality and connectivity between pairs of AP-1 factors across cells. Additional knowledge on the transcriptional regulatory interactions among AP-1 factors from the SCENIC analysis [59] in Chapter 3 can also be incorporated into this *a priori* network. Using this input network, CellNetOpt optimizes the model against the experimental data by searching through all possible logic gates compatible with the input. The optimization algorithm in CellNetOpt will generate a family of optimal models that balance model complexity and accuracy in explaining the data. Combinatorial knockdown conditions not used in model training can then be used to validate the models or to rule out alternative models.

Analyzing the validated Boolean model can yield the following biological insights or hypotheses. First, examining the model state-transition graph, we can identify the attractor states (a single state or a reoccurring sequence of states), which describe the long-term behavior of the model [60,61]. With such analysis, we can determine: I) whether the attractors represent the differentiation fates of COLO858; II) what circuitries (e.g., feedback loops) within the network are driving these attractors, and III) perturbations of which node(s) can shift the network from one attractor or differentiation state to another. Such information will provide insights into the key AP-1 combinations and interactions underlying each differentiation state.

Additionally, by examining the network topology we can generate hypotheses about mechanistic interactions between AP-1 factors. For example, an “AND” operator connecting two AP-1 factors suggests that their downstream activity possibly requires dimer formation. On the other hand, a toggle-switch-like topology between two AP-1 proteins could imply a scenario where each AP-1 self-activates as homodimers and mutually inhibits one another through heterodimerization. Such dimeric interactions between transcription factors have been shown recently to generate multi-stability in synthetic circuits [62]. To test these hypotheses derived from the Boolean model, we can then model these hypothetical key AP-1 interactions mechanistically and dynamically in greater detail using ordinary differential equations (ODE). Additional time-course perturbation experiments focusing on these key interactions can be used to calibrate and validate the ODE models. Analyzing such ODE models (e.g., by stability analysis and sensitivity analysis) can further generate novel insights into how we may be able to manipulate cell state stability and transition on the basis of key AP-1 factors in the model.

2) Understanding how the state of MAPK signaling is encoded by the AP-1 network.

As transcriptional effectors of the MAPK pathway, AP-1 plays an integral role in regulating transcription for diverse biological responses to extracellular stimuli. This suggests that the execution of appropriate cellular responses relies on the AP-1 network encoding the critical biochemical context (e.g., identity of environmental stimuli) that is relayed through MAPK signaling dynamics [30,37,38,48,63]. Indeed, several AP-1 factors have been associated with resistance to MAPK signaling inhibition in melanoma, further suggesting the link between AP-1 state and the state of MAPK signaling dependency [12,36,64,65]. However, it remains unclear how AP-1 as a network integrates upstream MAPK signals to direct cell fate decisions such as differentiation or drug resistance. Using melanoma as an example system, I propose integrating multiplexed measurements and mathematical modeling to elucidate the interactions between the AP-1 network and its key activators, ERK, JNK and p38 MAP kinases. Elucidating the mapping between the AP-1 network and MAPK signaling will be key to understand the molecular basis of cell-to-cell heterogeneity in differentiation state and sensitivity to MAPK inhibition.

To generate the data for network inference, I propose treating a heterogeneous cell line (e.g., COLO858) with ERK inhibitor, JNK inhibitor, or p38 inhibitor, individually and in pairwise combinations, for multiple time-points (e.g., 0.5 h, 2 h, 6 h, 15 h, 24 h, 72 h). Using 4i [53], we can then measure the activity of three MAP kinases, the key AP-1 factors (from the previous section), their phosphorylated states and differentiation state markers for each condition at the single-cell level. Applying a similar data-driven approach from the previous section, we can train a Boolean model of the AP-1-MAPK network against the time-course perturbation data

[66]. The optimized AP-1-MAPK Boolean model can then be validated with additional time-course experiments that simultaneously perturb MAP kinases and AP-1 (e.g., combining MAPK inhibitors with CRISPR activation or interference to overexpress or deplete specific AP-1 proteins, respectively [67,68]). Using the Boolean model of the AP-1-MAPK network, we can then: I) identify the attractors of the AP-1-MAPK network and their associations with differentiation states, II) determine whether certain AP-1 circuitries encode specific MAPK states or dynamics (e.g., ERK reactivation), and III) determine whether perturbations of particular AP-1 factors can alter the MAPK state or vice versa. Finally, transforming the Boolean model of the AP-1-MAPK network to an ODE model [69] and incorporating mechanistic interactions identified in the previous section, we can obtain more detailed dynamic insights into the AP-1-MAPK network behaviors. For example, we can ask the following questions: I) what MAPK states or dynamics drive certain AP-1 dimer formations that are responsible for a particular differentiation state and vice versa? II) what parameters control the number and stability of attractors? III) under what parameter regimes, transient MAPK perturbations can lead to irreversible changes (hysteresis) in the AP-1 network? Through modeling of the AP-1 network, answers to these questions can provide a deeper understanding of how phenotypic heterogeneity, memory and plasticity can be modulated by upstream signaling perturbations.

Altogether, combining systems biology and control systems theory, these directions will provide novel network-level principles connecting AP-1 behaviors, oncogenic signaling and cell-fate control. These principles can offer important insights into the mechanisms of drug response heterogeneity and adaptive resistance to MAPK inhibitors, while opening up new opportunities to explore therapeutic strategies that enforce oncogene dependency by modulating the state of the AP-1 network.

References:

1. Symmons O, Raj A. What's Luck Got to Do with It: Single Cells, Multiple Fates, and Biological Nondeterminism. Mol Cell. 2016;62: 788–802. doi:10.1016/J.MOLCEL.2016.05.023

2. Shaffer SM, Dunagin MC, Torborg SR, Torre EA, Emert B, Krepler C, et al. Rare cell variability and drug-induced reprogramming as a mode of cancer drug resistance. Nature. 2017;546: 431–435. doi:10.1038/nature22794

3. Wouters J, Kalender-Atak Z, Minnoye L, Spanier KI, De Waegeneer M, Bravo González-Blas C, et al. Robust gene expression programs underlie recurrent cell states and phenotype switching in melanoma. Nat Cell Biol. 2020;22: 986–998. doi:10.1038/s41556-020-0547-3

4. Roesch A, Fukunaga-Kalabis M, Schmidt EC, Zabierowski SE, Brafford PA, Vultur A, et al. A temporarily distinct subpopulation of slow-cycling melanoma cells is required for continuous tumor growth. Cell. 2010;141: 583–594. doi:10.1016/j.cell.2010.04.020

5. Torre EA, Arai E, Bayatpour S, Jiang CL, Beck LE, Emert BL, et al. Genetic screening for single-cell variability modulators driving therapy resistance. Nat Genet. 2021;53: 76–85. doi:10.1038/s41588-020-00749-z

6. Goyal Y, Dardani IP, Busch GT, Emert B, Fingerman D, Kaur A, et al. Pre-determined diversity in resistant fates emerges from homogenous cells after anti-cancer drug treatment. bioRxiv; 2021. p. 2021.12.08.471833. doi:10.1101/2021.12.08.471833

7. Khaliq M, Manikkam M, Martinez ED, Fallahi-Sichani M. Epigenetic modulation reveals differentiation state specificity of oncogene addiction. Nat Commun. 2021;12: 1536. doi:10.1038/s41467-021-21784-2

8. Tsoi J, Robert L, Paraiso K, Galvan C, Sheu KM, Lay J, et al. Multi-stage Differentiation Defines Melanoma Subtypes with Differential Vulnerability to Drug-Induced Iron-Dependent Oxidative Stress. Cancer Cell. 2018;33: 890-904.e5. doi:10.1016/j.ccell.2018.03.017

9. Rambow F, Rogiers A, Marin-Bejar O, Aibar S, Femel J, Dewaele M, et al. Toward Minimal Residual Disease-Directed Therapy in Melanoma. Cell. 2018;174: 843-855.e19. doi:10.1016/j.cell.2018.06.025

10. Tirosh I, Izar B, Prakadan SM, Wadsworth MH, Treacy D, Trombetta JJ, et al. Dissecting the multicellular ecosystem of metastatic melanoma by single-cell RNA-seq. Science. 2016;352: 189–196. doi:10.1126/science.aad0501

11. Verfaillie A, Imrichova H, Atak ZK, Dewaele M, Rambow F, Hulselmans G, et al. Decoding the regulatory landscape of melanoma reveals TEADS as regulators of the invasive cell state. Nat Commun. 2015;6: 6683. doi:10.1038/ncomms7683

12. Fallahi-Sichani M, Becker V, Izar B, Baker GJ, Lin J, Boswell SA, et al. Adaptive resistance of melanoma cells to RAF inhibition via reversible induction of a slowly dividing de-differentiated state. Mol Syst Biol. 2017;13: 905. doi:10.15252/msb.20166796

13. Heinz S, Romanoski CE, Benner C, Glass CK. The selection and function of cell type-specific enhancers. Nat Rev Mol Cell Biol. 2015;16: 144–154. doi:10.1038/nrm3949

14. Zaret KS, Carroll JS. Pioneer transcription factors: establishing competence for gene expression. Genes Dev. 2011;25: 2227–2241. doi:10.1101/gad.176826.111

15. Vierbuchen T, Ling E, Cowley CJ, Couch CH, Wang X, Harmin DA, et al. AP-1 Transcription Factors and the BAF Complex Mediate Signal-Dependent Enhancer Selection. Mol Cell. 2017;68: 1067-1082.e12. doi:10.1016/j.molcel.2017.11.026

16. Martínez-Zamudio RI, Roux P-F, de Freitas JANLF, Robinson L, Doré G, Sun B, et al. AP-1 imprints a reversible transcriptional programme of senescent cells. Nat Cell Biol. 2020;22: 842–855. doi:10.1038/s41556-020-0529-5

17. Samstein RM, Arvey A, Josefowicz SZ, Peng X, Reynolds A, Sandstrom R, et al. Foxp3 Exploits a Pre-Existent Enhancer Landscape for Regulatory T Cell Lineage Specification. Cell. 2012;151: 153–166. doi:10.1016/j.cell.2012.06.053

18. Heinz S, Benner C, Spann N, Bertolino E, Lin YC, Laslo P, et al. Simple Combinations of Lineage-Determining Transcription Factors Prime cis-Regulatory Elements Required for Macrophage and B Cell Identities. Mol Cell. 2010;38: 576–589. doi:10.1016/j.molcel.2010.05.004

19. Phanstiel DH, Van Bortle K, Spacek D, Hess GT, Shamim MS, Machol I, et al. Static and Dynamic DNA Loops form AP-1-Bound Activation Hubs during Macrophage Development. Mol Cell. 2017;67: 1037-1048.e6. doi:10.1016/j.molcel.2017.08.006

20. Madrigal P, Alasoo K. AP-1 Takes Centre Stage in Enhancer Chromatin Dynamics. Trends Cell Biol. 2018;28: 509–511. doi:10.1016/j.tcb.2018.04.009

21. Bakiri L, Macho-Maschler S, Custic I, Niemiec J, Guío-Carrión A, Hasenfuss SC, et al. Fra-1/AP-1 induces EMT in mammary epithelial cells by modulating Zeb1/2 and TGFβ expression. Cell Death Differ. 2015;22: 336–350. doi:10.1038/cdd.2014.157

22. Skene PJ, Henikoff S. An efficient targeted nuclease strategy for high-resolution mapping of DNA binding sites. Reinberg D, editor. eLife. 2017;6: e21856. doi:10.7554/eLife.21856

23. Bailey TL, Johnson J, Grant CE, Noble WS. The MEME Suite. Nucleic Acids Res. 2015;43: W39–W49. doi:10.1093/nar/gkv416

24. Ma S, Zhang B, LaFave LM, Earl AS, Chiang Z, Hu Y, et al. Chromatin Potential Identified by Shared Single-Cell Profiling of RNA and Chromatin. Cell. 2020;183: 1103-1116.e20. doi:10.1016/j.cell.2020.09.056

25. Street K, Risso D, Fletcher RB, Das D, Ngai J, Yosef N, et al. Slingshot: cell lineage and pseudotime inference for single-cell transcriptomics. BMC Genomics. 2018;19: 477. doi:10.1186/s12864-018-4772-0

26. Setty M, Kiseliovas V, Levine J, Gayoso A, Mazutis L, Pe'er D. Characterization of cell fate probabilities in single-cell data with Palantir. Nat Biotechnol. 2019;37: 451–460. doi:10.1038/s41587-019-0068-4

27. Bravo González-Blas C, Minnoye L, Papasokrati D, Aibar S, Hulselmans G, Christiaens V, et al. cisTopic: cis-regulatory topic modeling on single-cell ATAC-seq data. Nat Methods. 2019;16: 397–400. doi:10.1038/s41592-019-0367-1

28. Gasperini M, Hill AJ, McFaline-Figueroa JL, Martin B, Kim S, Zhang MD, et al. A Genome-wide Framework for Mapping Gene Regulation via Cellular Genetic Screens. Cell. 2019;176: 377-390.e19. doi:10.1016/j.cell.2018.11.029

29. Lito P, Pratilas CA, Joseph EW, Tadi M, Halilovic E, Zubrowski M, et al. Relief of profound feedback inhibition of mitogenic signaling by RAF inhibitors attenuates their activity in BRAFV600E melanomas. Cancer Cell. 2012;22: 668–682. doi:10.1016/j.ccr.2012.10.009

30. Wisdom R. AP-1: One Switch for Many Signals. Exp Cell Res. 1999;253: 180–185. doi:10.1006/excr.1999.4685

31. Lopez-Bergami P, Lau E, Ronai Z. Emerging roles of ATF2 and the dynamic AP1 network in cancer. Nat Rev Cancer. 2010;10: 65–76. doi:10.1038/nrc2681

32. Angel P, Karin M. The role of Jun, Fos and the AP-1 complex in cell-proliferation and transformation. Biochim Biophys Acta BBA - Rev Cancer. 1991;1072: 129–157. doi:10.1016/0304-419X(91)90011-9

33. Angel P, Szabowski A, Schorpp-Kistner M. Function and regulation of AP-1 subunits in skin physiology and pathology. Oncogene. 2001;20: 2413–2423. doi:10.1038/sj.onc.1204380

34. Eferl R, Wagner EF. AP-1: a double-edged sword in tumorigenesis. Nat Rev Cancer. 2003;3: 859–868. doi:10.1038/nrc1209

35. Maurus K, Hufnagel A, Geiger F, Graf S, Berking C, Heinemann A, et al. The AP-1 transcription factor FOSL1 causes melanocyte reprogramming and transformation. Oncogene. 2017;36: 5110–5121. doi:10.1038/onc.2017.135

36. Ramsdale R, Jorissen RN, Li FZ, Al-Obaidi S, Ward T, Sheppard KE, et al. The transcription cofactor c-JUN mediates phenotype switching and BRAF inhibitor resistance in melanoma. Sci Signal. 2015;8. doi:10.1126/scisignal.aab1111

37. van Dam H, Castellazzi M. Distinct roles of Jun : Fos and Jun : ATF dimers in oncogenesis. Oncogene. 2001;20: 2453–2464. doi:10.1038/sj.onc.1204239

38. Nakakuki T, Birtwistle MR, Saeki Y, Yumoto N, Ide K, Nagashima T, et al. Ligand-Specific c-Fos Expression Emerges from the Spatiotemporal Control of ErbB Network Dynamics. Cell. 2010;141: 884–896. doi:10.1016/j.cell.2010.03.054

39. Fuchs SY, Xie B, Adler V, Fried VA, Davis RJ, Ronai Z. c-Jun NH2-terminal Kinases Target the Ubiquitination of Their Associated Transcription Factors. J Biol Chem. 1997;272: 32163–32168. doi:10.1074/jbc.272.51.32163

40. Tanos T, Marinissen MJ, Leskow FC, Hochbaum D, Martinetto H, Gutkind JS, et al. Phosphorylation of c-Fos by Members of the p38 MAPK Family: ROLE IN THE AP-1 RESPONSE TO UV LIGHT. J Biol Chem. 2005;280: 18842–18852. doi:10.1074/jbc.M500620200

41. Ouwens DM, de Ruiter ND, van der Zon GCM, Carter AP, Schouten J, van der Burgt C, et al. Growth factors can activate ATF2 via a two-step mechanism: phosphorylation of Thr71 through the Ras-MEK-ERK pathway and of Thr69 through RalGDS-Src-p38. EMBO J. 2002;21: 3782–3793. doi:10.1093/emboj/cdf361

42. Angel P, Hattori K, Smeal T, Karin M. The jun proto-oncogene is positively autoregulated by its product, Jun/AP-1. Cell. 1988;55: 875–885. doi:10.1016/0092-8674(88)90143-2

43. Fuchs SY, Tappin I, Ronai Z. Stability of the ATF2 Transcription Factor Is Regulated by Phosphorylation and Dephosphorylation. J Biol Chem. 2000;275: 12560–12564. doi:10.1074/jbc.275.17.12560

44. Wolfgang CD, Liang G, Okamoto Y, Allen AE, Hai T. Transcriptional Autorepression of the Stress-inducible Gene ATF3. J Biol Chem. 2000;275: 16865–16870. doi:10.1074/jbc.M909637199

45. Chiu R, Boyle WJ, Meek J, Smeal T, Hunter T, Karin M. The c-fos protein interacts with c-Jun/AP-1 to stimulate transcription of AP-1 responsive genes. Cell. 1988;54: 541–552. doi:10.1016/0092-8674(88)90076-1

46. Matsuo K, Owens JM, Tonko M, Elliott C, Chambers TJ, Wagner EF. Fosl1 is a transcriptional target of c-Fos during osteoclast differentiation. Nat Genet. 2000;24: 184–187. doi:10.1038/72855

47. Chalmers CJ, Gilley R, March HN, Balmanno K, Cook SJ. The duration of ERK1/2 activity determines the activation of c-Fos and Fra-1 and the composition and quantitative transcriptional output of AP-1. Cell Signal. 2007;19: 695–704. doi:10.1016/j.cellsig.2006.09.001

48. Bakiri L, Matsuo K, Wisniewska M, Wagner EF, Yaniv M. Promoter Specificity and Biological Activity of Tethered AP-1 Dimers. Mol Cell Biol. 2002 [cited 7 Feb 2022]. doi:10.1128/MCB.22.13.4952-4964.2002

49. Rodríguez-Martínez JA, Reinke AW, Bhimsaria D, Keating AE, Ansari AZ. Combinatorial bZIP dimers display complex DNA-binding specificity landscapes. eLife. 2017;6: e19272. doi:10.7554/eLife.19272

50. Hettinger K, Vikhanskaya F, Poh MK, Lee MK, de Belle I, Zhang J-T, et al. c-Jun promotes cellular survival by suppression of PTEN. Cell Death Differ. 2007;14: 218–229. doi:10.1038/sj.cdd.4401946

51. Ham J, Babij C, Whitfield J, Pfarr CM, Lallemand D, Yaniv M, et al. A c-jun dominant negative mutant protects sympathetic neurons against programmed cell death. Neuron. 1995;14: 927–939. doi:10.1016/0896-6273(95)90331-3

52. Fuchs SY, Ronai Z. Ubiquitination and degradation of ATF2 are dimerization dependent. Mol Cell Biol. 1999;19: 3289–3298. doi:10.1128/MCB.19.5.3289

53. Gut G, Herrmann MD, Pelkmans L. Multiplexed protein maps link subcellular organization to cellular states. Science. 2018;361: eaar7042. doi:10.1126/science.aar7042

54. Saez-Rodriguez J, Alexopoulos LG, Epperlein J, Samaga R, Lauffenburger DA, Klamt S, et al. Discrete logic modelling as a means to link protein signalling networks with functional analysis of mammalian signal transduction. Mol Syst Biol. 2009;5: 331. doi:10.1038/msb.2009.87

55. Morris MK, Saez-Rodriguez J, Sorger PK, Lauffenburger DA. Logic-Based Models for the Analysis of Cell Signaling Networks. Biochemistry. 2010;49: 3216–3224. doi:10.1021/bi902202q

56. Terfve C, Cokelaer T, Henriques D, MacNamara A, Goncalves E, Morris MK, et al. CellNOptR: a flexible toolkit to train protein signaling networks to data using multiple logic formalisms. BMC Syst Biol. 2012;6: 133. doi:10.1186/1752-0509-6-133

57. Krishnaswamy S, Spitzer MH, Mingueneau M, Bendall SC, Litvin O, Stone E, et al. Conditional density-based analysis of T cell signaling in single-cell data. Science. 2014;346: 1250689. doi:10.1126/science.1250689

58. Qin X, Sufi J, Vlckova P, Kyriakidou P, Acton SE, Li VSW, et al. Cell-type-specific signaling networks in heterocellular organoids. Nat Methods. 2020;17: 335–342. doi:10.1038/s41592-020-0737-8

59. Aibar S, González-Blas CB, Moerman T, Huynh-Thu VA, Imrichova H, Hulselmans G, et al. SCENIC: single-cell regulatory network inference and clustering. Nat Methods. 2017;14: 1083–1086. doi:10.1038/nmeth.4463

60. Schwab JD, Kühlwein SD, Ikonomi N, Kühl M, Kestler HA. Concepts in Boolean network modeling: What do they all mean? Comput Struct Biotechnol J. 2020;18: 571–582. doi:10.1016/j.csbj.2020.03.001

61. Mendoza L. A network model for the control of the differentiation process in Th cells. Biosystems. 2006;84: 101–114. doi:10.1016/j.biosystems.2005.10.004

62. Zhu R, del Rio-Salgado JM, Garcia-Ojalvo J, Elowitz MB. Synthetic multistability in mammalian cells. Science. 2022;375: eabg9765. doi:10.1126/science.abg9765

63. Gillies TE, Pargett M, Minguet M, Davies AE, Albeck JG. Linear Integration of ERK Activity Predominates over Persistence Detection in Fra-1 Regulation. Cell Syst. 2017;5: 549-563.e5. doi:10.1016/j.cels.2017.10.019

64. Yang C, Tian C, Hoffman TE, Jacobsen NK, Spencer SL. Melanoma subpopulations that rapidly escape MAPK pathway inhibition incur DNA damage and rely on stress signalling. Nat Commun. 2021;12: 1747. doi:10.1038/s41467-021-21549-x

65. Falletta P, Sanchez-Del-Campo L, Chauhan J, Effern M, Kenyon A, Kershaw CJ, et al. Translation reprogramming is an evolutionarily conserved driver of phenotypic plasticity and therapeutic resistance in melanoma. Genes Dev. 2017;31: 18–33. doi:10.1101/gad.290940.116

66. MacNamara A, Terfve C, Henriques D, Bernabé BP, Saez-Rodriguez J. State–time spectrum of signal transduction logic models. Phys Biol. 2012;9: 045003. doi:10.1088/1478-3975/9/4/045003

67. Larson MH, Gilbert LA, Wang X, Lim WA, Weissman JS, Qi LS. CRISPR interference (CRISPRi) for sequence-specific control of gene expression. Nat Protoc. 2013;8: 2180–2196. doi:10.1038/nprot.2013.132

68. Maeder ML, Linder SJ, Cascio VM, Fu Y, Ho QH, Joung JK. CRISPR RNA–guided activation of endogenous human genes. Nat Methods. 2013;10: 977–979. doi:10.1038/nmeth.2598

69. Wittmann DM, Krumsiek J, Saez-Rodriguez J, Lauffenburger DA, Klamt S, Theis FJ. Transforming Boolean models to continuous models: methodology and application to T-cell receptor signaling. BMC Syst Biol. 2009;3: 1–21. doi:10.1186/1752-0509-3-98

Appendices

Appendix A Supplementary Information for Chapter 3

Table A.1 List of bZIP transcription factor genes used in constructing the random PLSR models in Figure 3.11.

Transcript levels of 8 randomly chosen bZIP transcription factors from this list were used to construct each random model.

Gene Name
BACH1
BACH2
BATF
BATF3
CEBPA
CEBPB
CEBPD
CEBPE
CEBPG
CREB1
CREB3
CREB3L1
CREB3L3
CREB5
CREM
DBP
DDIT3
HCFC1
HLF
JDP2
MAF
MAFB
MAFF
MAFG
MAFK
NFE2
NFE2L2
NFE2L3
NFIL3
NRF1
NRL
TEF
XBP1

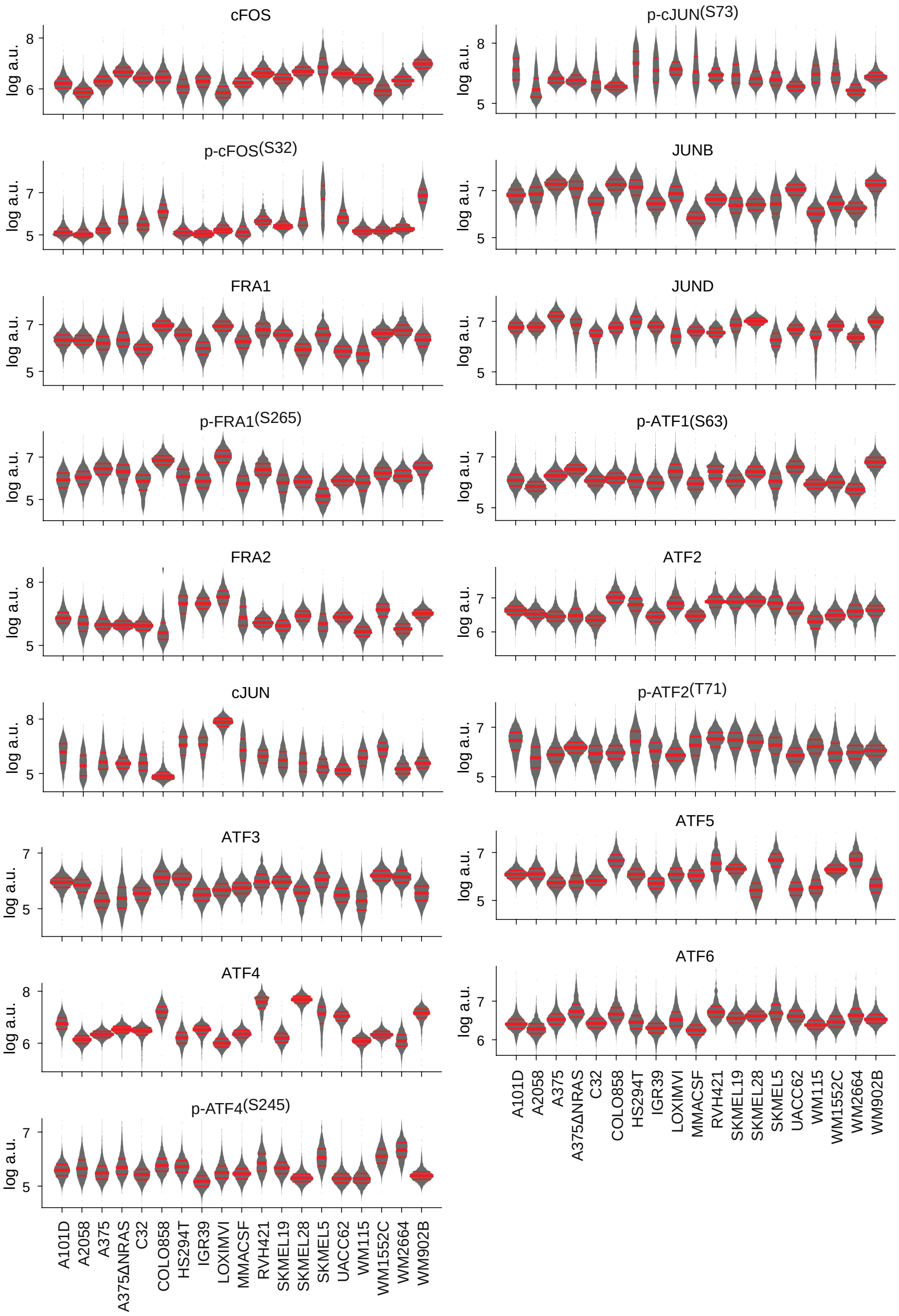

Figure A.1 Single-cell distribution of seventeen AP-1 factors measured across 19 cell lines and shown by violin plots highlighting the median and interquartile (25% and 75%) ranges. Related to Figure 3.2 and Figure 3.3.

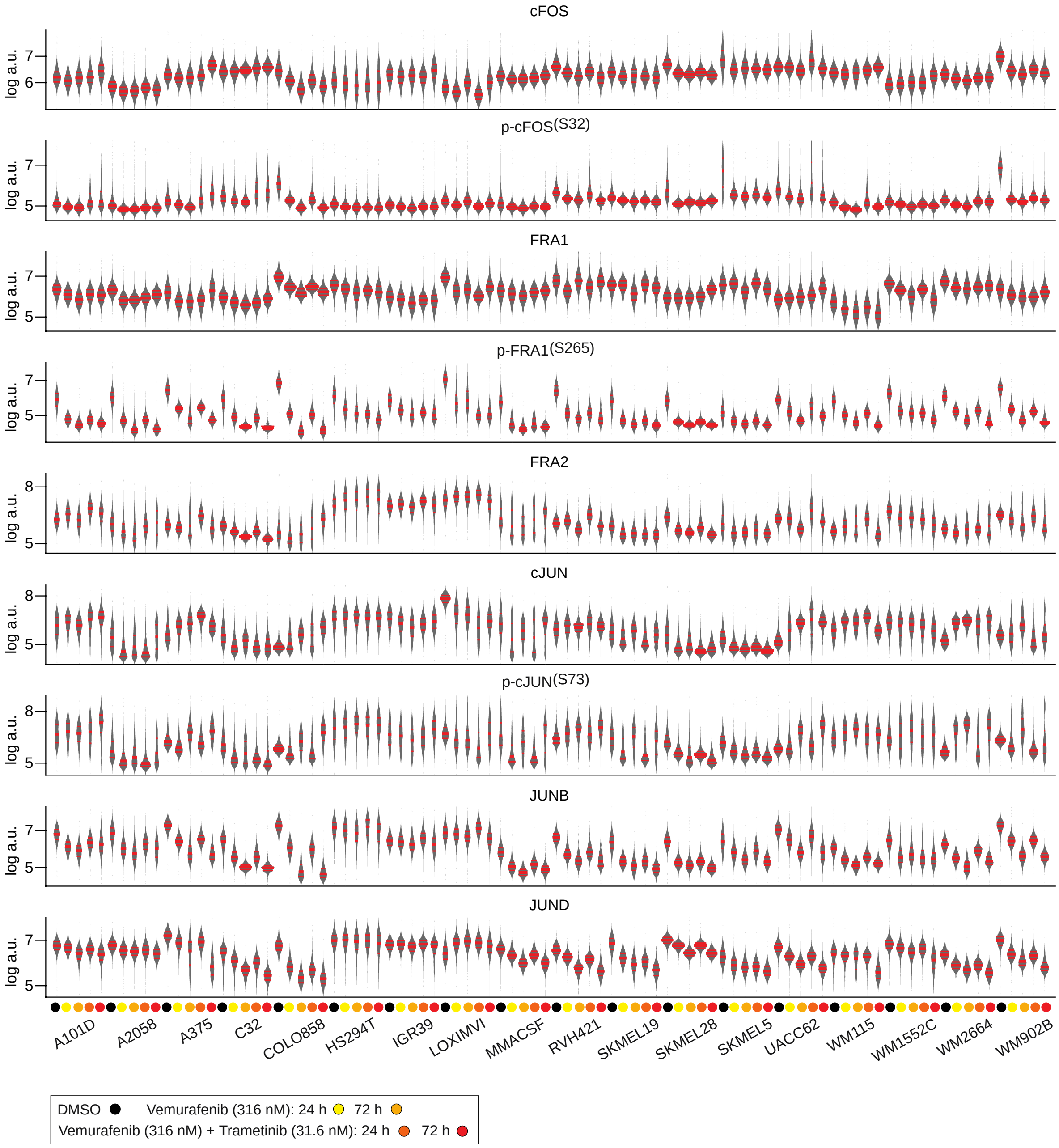

Figure A.2 Single-cell distribution of AP-1 protein measurements, including cFOS, p-cFOS, FRA1, p-FRA1, FRA2, cJUN, p-cJUN, JUNB, and JUND, measured in 18 cell lines before and following treatment with MAPK inhibitors for 24 and 72 h. Violin plots highlight the median and interquartile (25% and 75%) ranges. Related to Figure 3.14.

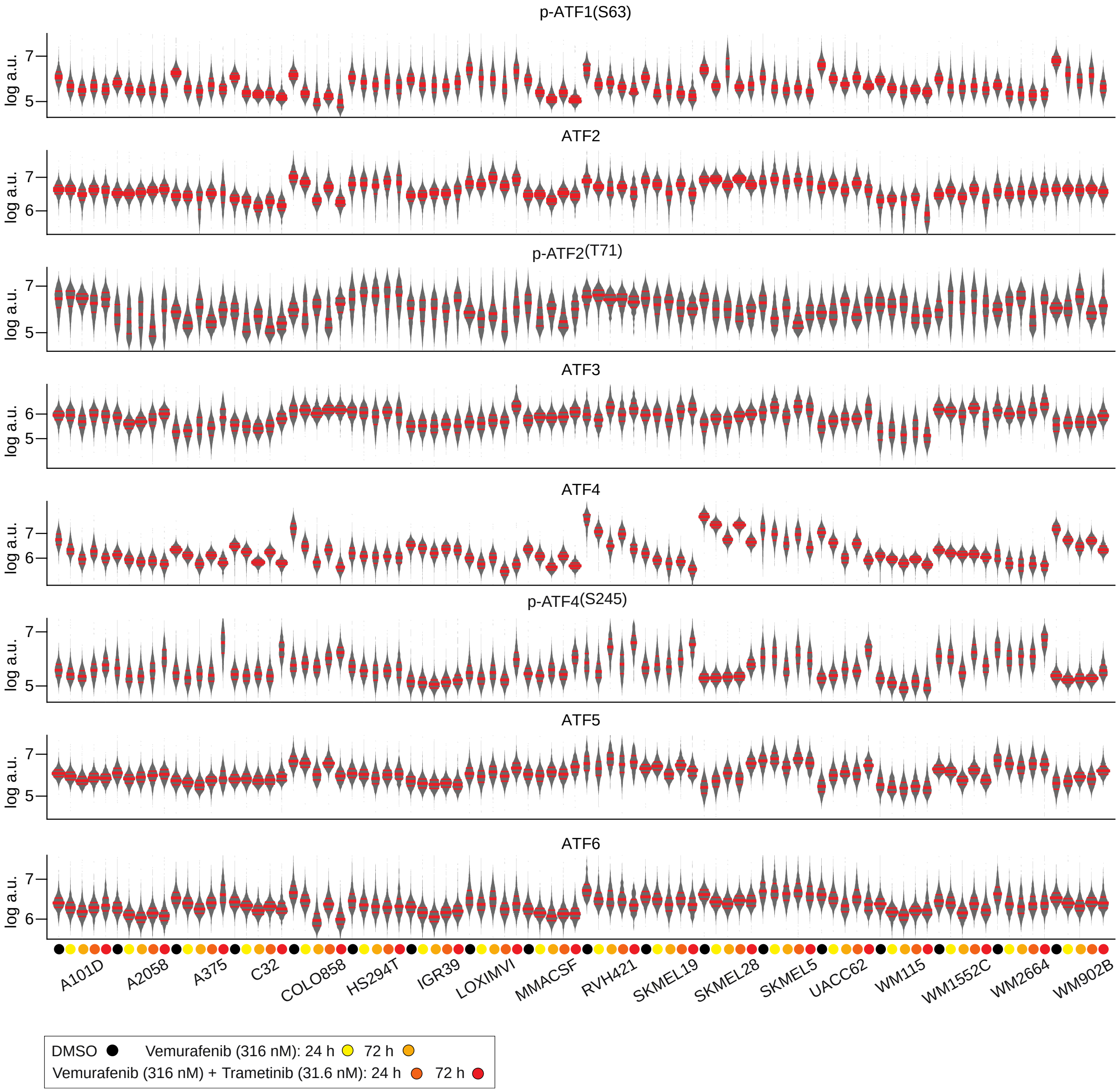

Figure A.3 Single-cell distribution of AP-1 protein measurements, including p-ATF1, ATF2, p-ATF2, ATF3, ATF4, p-ATF4, ATF5 and ATF6, measured in 18 cell lines before and following treatment with MAPK inhibitors for 24 and 72 h. Violin plots highlight the median and interquartile (25% and 75%) ranges. Related to Figure 3.14.

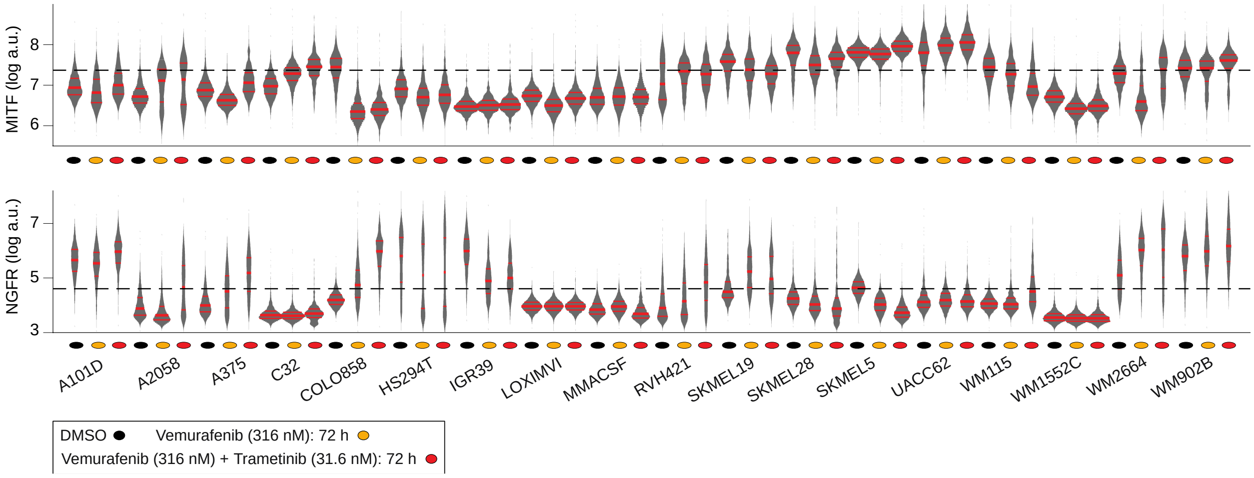

Figure A.4 Single-cell distribution of melanoma differentiation state markers MITF and NGFR, measured in 18 cell lines before and following treatment with MAPK inhibitors for 24 and 72 h. Violin plots highlight the median and interquartile (25% and 75%) ranges. Related to Figure 3.15 and Figure 3.16.